Quantum signal processing with mechanical oscillators

by

Reed W. Andrews

B.A., Macalester College, 2008

M.S., University of Colorado, 2012

A thesis submitted to the

Faculty of the Graduate School of the

University of Colorado in partial fulfillment

of the requirements for the degree of

Doctor of Philosophy

Department of Physics

2015

This thesis entitled:
Quantum signal processing with mechanical oscillators
written by Reed W. Andrews
has been approved for the Department of Physics

Konrad Lehnert

Cindy Regal

Date

The final copy of this thesis has been examined by the signatories, and we find that both the content and the form meet acceptable presentation standards of scholarly work in the above mentioned discipline.

Andrews, Reed W. (Ph.D., Physics)

Quantum signal processing with mechanical oscillators

Thesis directed by Prof. Konrad Lehnert

This thesis experimentally demonstrates how macroscopic mechanical oscillators can be used to process and manipulate electromagnetic signals, i.e. light. Light shined upon an object can cause it to move or, as in the case of a mechanical oscillator, vibrate. This interaction allows light to be converted between vastly different frequencies, and provides an opportunity to manipulate the time and frequency content of electromagnetic signals. The following chapters describe the construction and measurement of systems that use electromagnetic resonators and highly tensioned membranes as mechanical oscillators to manipulate electromagnetic signals with high efficiency and extremely low added noise. These results show that mechanical oscillators can bring needed signal processing capabilities to quantum information networks, where they can be used to connect separate, physically distant, and otherwise mismatched cQED systems.

Dedication

I would like to dedicate this dissertation to the car that I will hopefully be able to purchase when I am no longer limited to the salary of a graduate student.

Also, to my wife Anna. We make a good team, even if she is way cooler than me.

Acknowledgements

I'd like to thank Konrad Lehnert for hiring me into his lab back in 2009. Although I spent my first year in graduate school far more concerned with coursework than with lab work, I like to think I've made up for this in the years since. Konrad has an incredibly keen sense of how currents and voltages propagate through circuits. I've tried to acquire some of this knowledge, but instead I seem to have acquired a penchant for using over-the-top analogies to explain my feelings on a subject.

I'd also like to thank Cindy Regal for a fruitful collaboration that combined microwaves, lasers, and membranes. I may still carry a small grudge from when she banned everyone in her lab from working on (or speaking to me about) the project for a small portion of 2012, but once she has read and signed this thesis all transgressions real and imagined will be forgotten.

I'd also like to thank all members of the JILA shop. I am a skeptical person and sometimes ignored their advice. In most cases, however, if I was smarter I would have followed it.

I'd also like to thank all the labmates I've worked with throughout my time at graduate school. Jen Harlow and Tobias Donner had the patience to let me make mistakes, even when it slowed their progress. Joe Kerckhoff always asked a variety of questions, and in trying to answer them I had to thoroughly consider many different experimental options. These questions helped counter my eternal temptation to solve problems with the most familiar method rather than with the best/cheapest/most reliable method. Adam Reed has displayed a great deal of patience with my sometimes unhelpful direction and advice. Tom Purdy and Robert Peterson gave me a crash course in optics and building optical cavities, and didn't object too strongly when I tried to map

everything onto notions of microwave network analysis. Kat Cicak taught me much of what I know about fabrication techniques.

I'd also like to thank Stephen Pordes and everyone at the PAB for introducing me to experimental physics.

I've had the good fortune to meet and work with people who have been willing to share their knowledge and expertise. Perhaps we'll have future opportunities to collaborate. But, in the meantime, thank you for helping me earn a doctorate.

Contents

Chapter

Tables

Table

Figures

Figure

Chapter 1

Introduction

Light carries momentum. It was—and perhaps still is—a strange concept: light shined upon an object can cause it to move, change course. This peculiar ability of light was perhaps first observed by Johannes Kepler when he noted that the tail of a comet is seemingly "an effluvium from the head, expelled through the rays of the sun..." [1, 2]. As early as 1754, laboratory experiments attempted to confirm that light can move an object [3, 4]. But these initial experiments could not disentangle the effect of light from that of residual air currents, in part because there was no quantitative prediction of how much momentum light should carry.

In 1873, Maxwell's theory of electromagnetism predicted that electromagnetic waves–that is, light—should indeed carry a very specific amount of momentum [5]. A few decades later, the existence and predicted magnitude of the 'radiation pressure' of light were experimentally confirmed [6, 7, 8, 9]. Soon after the invention of the laser, radiation pressure was used to manipulate and control small, micron-scale objects [10], and this spawned proposals that used radiation pressure to cool the motion of atoms [11, 12]. Radiation pressure cooling of trapped atoms was demonstrated in the 1970s [13], and has since become widely used [14].

Far from manipulating single atoms, radiation pressure can control the motion of macroscopic objects. The mathematical understanding of their control and manipulation developed in the context of highly sensitive interferometers designed to detect small strains induced by gravitational waves [15, 16]. An early gravitational wave detector is diagrammed in Fig. 1.1. The position of suspended mirrors used in the interferometer is influenced by radiation pressure: Reflected light

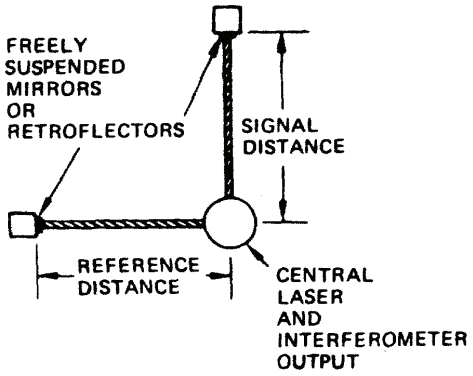

Figure 1.1: Laser interferometer for gravitational wave detection, from [16]. The radiation pressure of the light reflected from the mirrors affects their position. This effect limits the theoretical sensitivity of such interferometers, and can also be used to control the motion of the mirrors.

transfers momentum to the mirrors and alters their position. At the quantum level, fluctuations of the electromagnetic field create a fluctuating force on the mirrors that limits the sensitivity of the interferometer as expected from the Heisenberg uncertainty principle [17, 18]. In addition to disturbing the position of the mirror, radiation pressure changes the dynamical behavior of the mirror's vibrations and can provide damping or anti-damping of vibrations [19]. This phenomenon, termed 'dynamical backaction', was first demonstrated in 1970 [20]. Initial work has given rise to the field of cavity optomechanics, a field that focuses on manipulating macroscopic objects with radiation pressure.

The prototypical cavity optomechanical system contains an optical cavity with one mirror harmonically bound, as diagrammed in Fig. 1.2. The mirror forms a macroscopic mechanical oscillator whose motion couples to the electromagnetic field confined in the cavity. The radiation pressure coupling is characterized by a quantity G that expresses the resonant frequency shift of the cavity per unit motion of the mechanical oscillator. Originally, the goals of cavity optomechanics were to study this interaction in order to make better detectors of force [21, 22], acceleration, mass, and anything that could be somehow coupled to the motion of a macroscopic object [23, 24]. Other more exotic goals include using radiation pressure to generate nonclassical states of motion in a macroscopic mechanical oscillator [25, 26] and using these nonclassical states to probe the

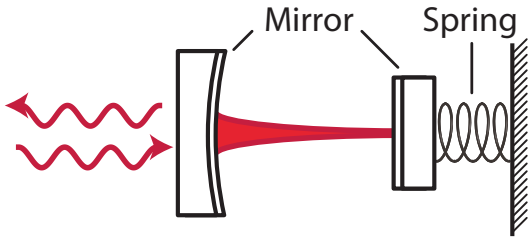

Figure 1.2: A cavity optomechanical system. The prototypical cavity optomechanical system contains a cavity formed from two high-reflectivity mirrors. One mirror is fixed, and the other is harmonically bound.

intersection of gravity and quantum mechanics [27, 28]. A first major goal of cavity optomechanics was to use radiation pressure to cool a macroscopic mechanical oscillator to near its ground state of motion.

To cool a mechanical oscillator to its ground state, the damping provided by the electromagnetic field must exceed the decoherence rate of the mechanical oscillator. This requirement is often written as $\Gamma > n_{\rm m}\kappa_{\rm m}$, where $\kappa_{\rm m}$ is the coupling of the mechanical oscillator to its thermal environment and $n_{\rm m} \equiv 1/(e^{\hbar\omega_{\rm m}/k_{\rm B}T_{\rm env}} - 1)$ is the phonon occupation number of the mechanical oscillator for environment temperature $T_{\rm env}$ and mechanical oscillator frequency $\omega_{\rm m}$. The optomechanical damping Γ depends on the strength of a monochromatic electromagnetic field, often referred to as a pump: $\Gamma \propto n$, where n is the number of photons induced in the cavity by the pump. When $\Gamma > n_{\rm m}\kappa_{\rm m}$, the system is 'quantum-enabled' as electromagnetic signals couple to the mechanical oscillator faster than the mechanical oscillator acquires one phonon from its environment. Reaching this regime took a concerted experimental and theoretical effort. Early work probed the feasibility of quantum-enabled devices and established methods for characterizing optomechanical systems [29, 30, 31, 32] and understanding their limitations [33, 34, 35]. In 2011 two systems achieved ground state cooling of a macroscopic mechanical oscillator. One experiment used a microwave-frequency superconducting circuit coupled to a vibrating aluminum film [36], and the other a photonic and phononic crystal cavity [37]. These achievements have opened up the way for more tantalizing and

exotic proposals to become reality.

However, the leap between using radiation pressure for ground state cooling and using it to create nonclassical states of motion has proved challenging. Fundamentally, cooling exploits a linearized radiation pressure interaction that scales with pump power. The nonlinear interaction necessary to create nonclassical states of motion requires $Gx_{\mathrm{zp}} > \kappa$, where x_{zp} are the zero-point fluctuations of the mechanical oscillator and κ is the energy decay rate of the electromagnetic resonator [38, 39]. Even for state-of-the-art systems, reaching this new regime of optomechanical coupling seems a daunting task. New methods, new ways of thinking, and new creative designs [40] are beginning to emerge, and hopefully some will begin to probe quantum phenomena on a macroscopic scale.

If new methods do not work as hoped, there is still an incredible opportunity to use the linear, pump-enhanced radiation pressure interaction to manipulate (or process) electromagnetic signals. For a quantum-enabled optomechanical system, the manipulation can be clean and extraordinarily low noise as it only involves two degrees of freedom: the electromagnetic field and single mechanical oscillator. A growing portion of the cavity optomechanics community explores electromagnetic signal processing with quantum-enabled optomechanical systems. The signal processing capabilities have many potential near-term applications [24], but in particular they can be used to extend the abilities of quantum networks.

1.1 Cavity optomechanics in quantum networks

Quantum information networks are physically extended networks that use quantum nodes for processing information and quantum channels to link nodes [41], as diagrammed in Fig. 1.3. Quantum networks allow communication between nodes with security guaranteed by physical laws [42, 43], and can increase the capacity of communication channels beyond the classical Shannon bound [44]. Technologies for the nodes of a quantum information network are usually quantum two-level systems (qubits) such as nitrogen vacancy centers, Josephson junctions, or suitable atoms [45]. The communication channels that connect the nodes are almost invariably photonic, as

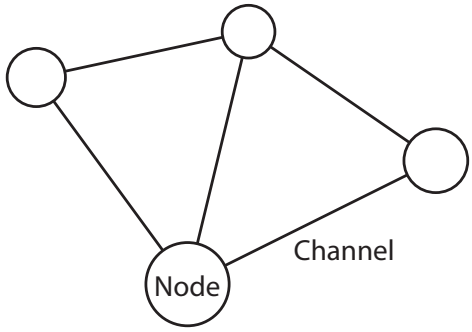

Figure 1.3: Schematic of a quantum information network. The network consists of nodes that process and store quantum information, and quantum channels that are used to transmit information between nodes [49, 41].

electromagnetic fields provide fast, low-loss transmission and they can be easily routed between nodes with cables or optical fibers [46]. A quantum network constructed using these elements requires control over both the temporal and spectral content of the quantum electromagnetic signals exchanged between nodes. Temporal control allows entanglement to be deterministically distributed throughout the network [47], and spectral control allows different types of qubits to be used in the same quantum network. For example, spectral control is needed to connect qubits based on Rubidium atoms with those based on Cesium, or with those based on quantum dots, as each type of qubit interacts with electromagnetic fields at a different frequency [48]. Network components that can arbitrarily shape the temporal and spectral content of quantum electromagnetic fields are a necessary component of complex quantum information networks.

Quantum-enabled cavity optomechanical systems can control both the temporal and spectral content of electromagnetic fields. Initial interest in using mechanical oscillators for this task was motivated by the broad number of systems that couple to motion of macroscopic objects. It was envisioned that mechanical oscillators could mediate qubit-light interactions and thus enable long distance quantum communication [50, 51, 52]. This led to the idea of 'optomechanical transducers' and 'photon-phonon translators' that could be used in a quantum network. Experiments in quantum signal processing with mechanical oscillators have demonstrated that optomechanical systems can be used to delay electromagnetic signals at both optical [53, 54] and microwave frequencies

[55, 56]. Other work has demonstrated time domain protocols that store electromagnetic signals as vibrations of a mechanical oscillator [57], and this capability has recently been extended to quantum-enabled systems [58, 59]. In addition, cavity optomechanical systems have been used to convert electromagnetic signals between different optical frequencies [60, 61, 62]. There has been an experimental push to extend the signal processing capabilities of cavity optomechanical systems and to integrate them into quantum information networks.

This thesis advances two goals in quantum signal processing. First, it extends the frequency conversion capabilities of cavity optomechanics to over four orders of magnitude in frequency, and in particular demonstrates bidirectional frequency conversion with record-breaking efficiency between signals at microwave and optical frequencies. As discussed in more detail in Chapter 3, this capability can provide the backbone of a hybrid quantum network that can exploit the benefits of all types of qubits, whether they be made from artificial atoms or real ones. Second, this thesis extends the time-domain processing of electromagnetic signals to show that beyond storage and delay, cavity optomechanics can be used to arbitrarily manipulate the temporal and spectral content of microwave-frequency electromagnetic signals. This new capability provides a way to create microwave-frequency quantum information networks.

1.2 Contents

Chapter 2 introduces the mechanical oscillators used in this work and how they can be incorporated into electromagnetic resonators. It also establishes a mathematical basis for the radiation pressure interaction in cavity optomechanics. This introductory chapter is not meant to be a rigorous explanation of all the phenomena of cavity optomechanics, but instead lays a framework for understanding the experiments of later chapters. Chapter 3 describes a demonstration of bidirectional and efficient conversion of electromagnetic signals between microwave and optical frequencies, and its relevance for quantum networks. Chapter 4 demonstrates that a mechanical oscillator in a microwave circuit can be used to control both the temporal and spectral content of electromagnetic signals. Finally, Chapter 5 looks to future experiments and how optomechanical systems can be

integrated into quantum information networks.

Chapter 2

Mechanical oscillators and light confined together

A mechanical oscillator is a prototypical physical system: An object of mass m, constrained to move in one dimension, is bound by a Hooke's law restoring force. If the mass interacts with light at all, light shined upon the mass can give it momentum. For a single photon, the maximum momentum transfer is $\Delta p = 2\hbar\omega/c$, where ω is the frequency of the photon, and c is the speed of light. This additional momentum causes the oscillator to vibrate with amplitude $2\hbar\omega/(m\omega_{\rm m}c)$, where $\omega_{\rm m}$ is the oscillation frequency of the mechanical oscillator. The mechanical oscillator 'remembers' the interaction until the vibrations of the oscillator decay away. This basic example highlights the scales that affect the radiation pressure interaction. Mechanical oscillators with a small mass are more easily driven by the momentum of light, and oscillators with low dissipation serve as better memories for photons.

Yet even low mass, high quality mechanical oscillators still only feebly interact with light. A single photon at 282 THz (1064 nm) only gives a vibrational amplitude of $\sim 10^{-22}$ m to a nanogram mechanical oscillator with $\omega_{\rm m} = 2\pi \times 1$ MHz. The photon-induced vibrations are completely masked by zero-point fluctuations of the mechanical oscillator, $x_{\rm zp} = \sqrt{\hbar/2m\omega_{\rm m}} \approx 10^{-16}$ m. The momentum kick imparted by a single photon can be amplified by incorporating the mechanical oscillator into an electromagnetic resonator. The resonator recirculates or recycles photons, giving each photon many interactions with the mechanical oscillator and amplifying the momentum transfer. A suitable mechanical oscillator and a high quality electromagnetic resonator form the basic cavity optomechanical system [23, 24].

Constructing low mass, high quality mechanical oscillators and integrating them with electromagnetic resonators is a key endeavor for creating quantum-enabled cavity optomechanical systems. Advances in microfabrication techniques have produced a variety of optomechanical systems [23]. For this thesis, we work exclusively with mechanical oscillators made from tensioned membranes. Section 2.1 describes some favorable properties of tensioned membranes, and section 2.2 describes how they can be integrated into electromagnetic resonators. Sections 2.3 through 2.5 give a mathematical framework for the radiation pressure interaction between electromagnetic fields and vibrations of a mechanical oscillator.

2.1 Tensioned membranes as mechanical oscillators

A membrane is a thin film with motion that is constrained by boundary conditions. Common examples of membranes include drumheads and trampolines. The motion of a membrane can be modeled as a collection of mechanical oscillators. For a membrane in two dimensions, its transverse vibrations are described by a wave equation [63]:

$$-\frac{D}{h}\left(\nabla^2\right)^2 W + T\nabla^2 W = \rho\frac{\partial^2}{\partial t^2}W \tag{2.1}$$

where W describes the transverse displacement of the film at a particular location and time, h is the thickness of the film and ρ its mass per unit area, and ∇^2 is the two-dimensional Laplacian. The parameters D and T control how much energy is required to deflect the film by a given amount. The flexural rigidity, D, depends on the membrane's mechanical properties and thickness: $D = Eh^3/(12(1-\nu^2))$, where E is the Young's modulus of the membrane and ν its Poisson ratio. The flexural rigidity scales as h^3, indicating that a thin membrane deforms more readily than a thick one. The tension T of the membrane also resists deformations, and for a thin membrane or large tension, the tension dominates the dynamics of the transverse vibrations.

Consider a square membrane in the y-z plane where each side of the membrane has length L, and is oriented as shown in Fig. 2.1. If we look for solutions $W(y,z,t)$ that are harmonic in time

so that $W(y,z,t) = W(y,z) \times \cos(\omega t)$, then the equation for the transverse displacement becomes

$$-\frac{D}{h}\left(\nabla^2\right)^2 W + T\nabla^2 W = -\rho\omega^2 W. \tag{2.2}$$

Eigenmodes of Eqn. 2.2 depend on the boundary conditions. For the membrane in Fig. 2.1 with all four edges clamped, displacement $W(y,z)$ must vanish and $\partial W/\partial y = 0$ or $\partial W/\partial z = 0$ at all four edges. Under these clamped boundary conditions, the approximate eigenmodes can be expressed using hyperbolic functions and sinusoids [64]. However, for a membrane with dynamics dominated by tension with $T \gg D/hL^2$, the eigenmodes are approximately sinusoidal [65, 66]:

$$W_{l,n}(y,z) \propto \sin\left(\frac{l\pi y}{L}\right) \times \sin\left(\frac{n\pi z}{L}\right) \tag{2.3}$$

where l and n are positive integers. In this high-tension approximation, the eigenvalues are given by

$$\omega_{l,n}^2 \approx \frac{T\pi^2}{\rho L^2}\left(l^2 + n^2\right). \tag{2.4}$$

Each eigenmode of the transverse vibrations can be considered a mechanical oscillator with resonant frequency $\omega_{l,n}$.

To completely map the vibrations of the membrane onto a collection of one-dimensional mechanical oscillators, we must assign each eigenmode an effective mass, m_{eff}, and a single displacement coordinate, x. With these assignments, the potential energy U of an eigenmode should be given by $U = m_{\text{eff}}\omega_{n,m}^2 x^2/2$, the potential energy of a one-dimensional mechanical oscillator. Although the coordinate x can be assigned in any way, it should be physically motivated. For example, x can be the average displacement of the membrane: $x(t) = L^{-2}\int_0^L W_{l,n}(y,z,t)dydz$. The convention used here is that $x(t) = \max(W_{l,n}(y,z,t))$. However x is assigned, it is always true that the potential energy of the membrane is well defined and can be expressed as [67, 23]

$$U = \frac{1}{2}\omega_{l,n}^2 \int_0^L \rho W_{l,n}(y,z,t)dydz = \frac{1}{2}m_{\text{eff}}\omega_{l,n}^2 x(t)^2. \tag{2.5}$$

For the chosen convention of $x(t) = \max(W_{l,n}(y,z,t))$, this gives an effective mass of

$$m_{\text{eff}} = \int_0^L \rho\left(\frac{W_{l,n}}{\max(W_{l,n})}\right)^2 dydz. \tag{2.6}$$

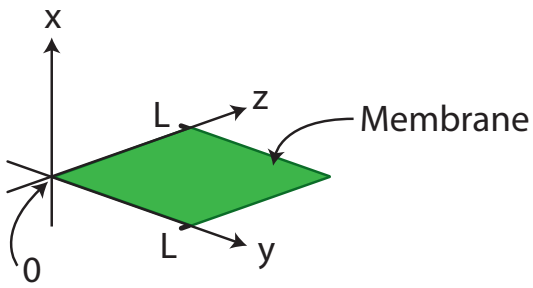

Figure 2.1: A coordinate system for a square membrane. The membrane is oriented in the y-z plane and each side has length L.

For the eigenmodes of Eqn. 2.3, $m_{\text{eff}} = m/4$ where m is the physical mass of the membrane, $m = \int_0^L \rho dy dz$. With this mapping, each eigenfunction $W_{n,m}$ of the membrane can be considered a mechanical oscillator with mass $m/4$ and frequency $\omega_{l,n}$. In a cavity optomechanical system, we usually study the interaction between the electromagnetic field and one particular vibrational eigenmode (or mode, for short) of the membrane.

2.1.1 Tension increases the quality factor of membrane vibrations

The quality factor of a membrane is crucial in determining whether a cavity optomechanical system is quantum enabled. For a quantum-enabled system, $\Gamma > n_{\text{m}}\kappa_{\text{m}}$, as introduced in Chapter 1. For temperatures $k_{\text{B}}T_{\text{env}} > \hbar\omega_{\text{m}}$, $n_{\text{m}} \approx k_{\text{B}}T_{\text{env}}/\hbar\omega_{\text{m}}$. In this case, a quantum-enabled system requires $\Gamma > k_{\text{B}}T_{\text{env}}/\hbar Q$, where $Q \approx \omega_{\text{m}}/\kappa_{\text{m}}$ is the quality factor of a particular vibrational mode of the membrane. Mechanical oscillators with higher quality factors reduce the optomechanical damping Γ necessary to make the system quantum-enabled. As outlined below, tensioned membranes generally have higher quality factors than untensioned structures.

Consider a membrane as in Fig. 2.1 that is simply supported so that at the boundaries $W = 0$. In this case, the eigenfunctions of Eqn. 2.1 are simply sinusoids as in Eqn. 2.3 and have eigenfrequencies [63, 68]

$$\omega_{l,n}^2 \approx \frac{T\pi^2}{\rho L^2}\left(l^2+n^2\right) + \frac{D\pi^4}{h\rho L^4}\left(l^2+n^2\right)^2 \tag{2.7}$$

where l and n are positive integers. Material properties affect the resonant frequency $\omega_{l,n}$. In particular, materials that absorb vibrational energy can be modeled with a complex Young's modulus where the imaginary part represents loss [69, 65]. Any imaginary part of the Young's modulus causes the resonant frequecy of the membrane $\omega_{l,n}$ to also be complex, and this causes vibrations of the membrane to damp over time as $W_{l,n}(y,z,t) = W_{l,n}(y,z) \times \mathrm{Re}\left(e^{\imath\omega_{l,n}t}\right)$. This loss directly affects the quality factor of the vibrations [70, 71]:

$$\frac{1}{Q} \equiv 2\left|\frac{\mathrm{Im}(\omega_{l,n})}{\mathrm{Re}(\omega_{l,n})}\right|. \tag{2.8}$$

Although the material used in the membrane is lossy, tension appears to have little or no imaginary part. Thus, greater tension increases the real part of the resonant frequency and improves the quality factor of the vibrations as can be seen from Eqns 2.7 and 2.8. In particular, in the high tension limit, $Q \propto \sqrt{T}$.

Even though the result that $Q \propto \sqrt{T}$ was found using simple boundary conditions, it is approximately true for a variety of conditions. The same relationship between quality factor and tension has been predicted using clamped boundary conditions [65]. Moreover, tension has been observed to increase the quality factor of vibrations [72, 66]. In real systems, however, the ultimate quality factor can be limited by factors beyond membrane material loss. For example, imperfect boundary conditions allow membrane vibrations to radiate out into the environment [73]. This limits the quality factor achievable through tension alone. Nonetheless, the high-Q vibrational modes achieved with tensioned membranes [65, 74] help create quantum-enabled optomechanical systems.

Two examples of membranes used in this thesis are shown in Fig. 2.2. The vibrational modes of the silicon nitride membrane are approximately described by Eqn. 2.3. Although the aluminum membrane has a much different support structure and boundary conditions, its vibrational modes still form mechanical oscillators. For both these types of membranes, tension develops from differential thermal contraction between the thin film and the substrate that supports it [68, 36], and this tension allows high-Q vibrational modes. A ringdown measurement of a vibrational mode of

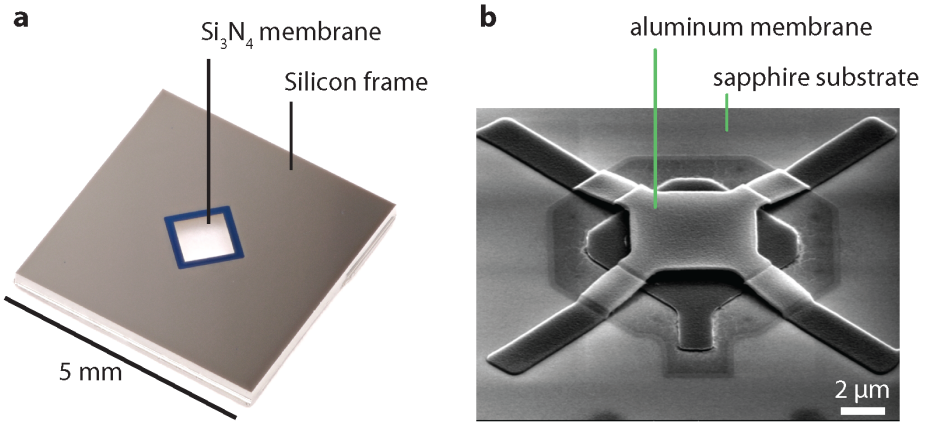

Figure 2.2: Two examples of tensioned membranes. **a**, Photograph of a silicon nitride (Si_3N_4) membrane supported by a silicon frame. The lowest frequency vibrational mode for this membrane is $\omega_m \approx 2\pi \times 400$ kHz. **b**, Scanning electron micrograph of an aluminum membrane on a sapphire substrate. The lowest frequency vibrational mode for this membrane is $\omega_m \approx 20$ MHz. A second aluminum film can be seen under the membrane. This structure forms a parallel-plate capacitor where one plate of the capacitor is free to vibrate. Image courtesy of John Teufel and Aric Sanders.

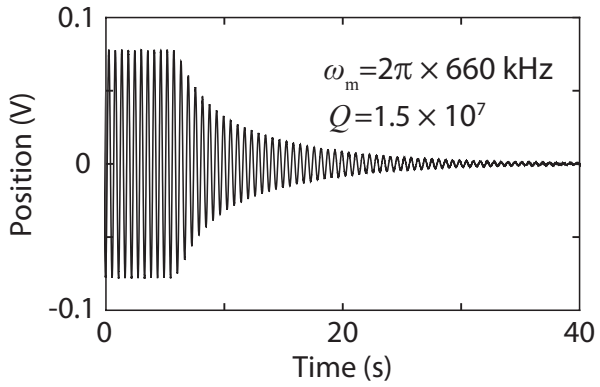

Figure 2.3: Ringdown of a silicon nitride (Si_3N_4) membrane. The membrane is cooled to <25 millikelvin in a dilution fridge and measured. The mechanical oscillator has a resonant frequency of $\omega_m = 2\pi \times 660$ kHz, and an energy decay rate of $\kappa_m = 2\pi \times 0.04$ Hz, yielding a quality factor of approximately 15 million.

a silicon nitride membrane is shown in Fig. 2.3. The fabrication of silicon nitride membranes is discussed in more detail in section 3.3, and the fabrication of aluminum membranes in section 4.2.2.

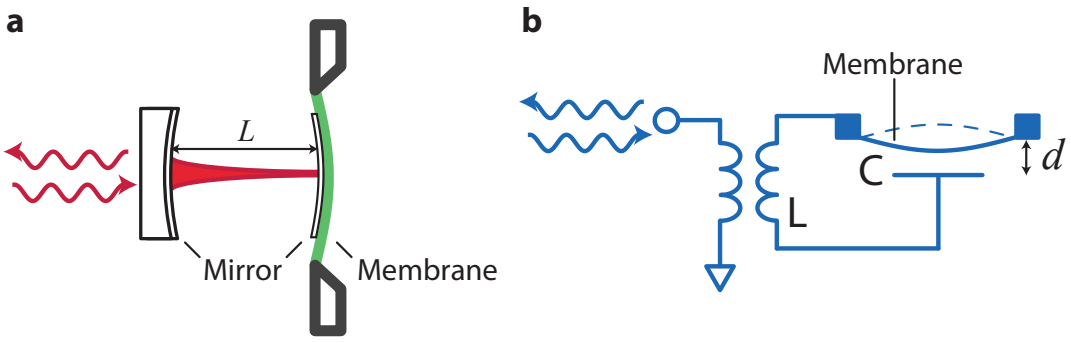

Figure 2.4: Diagrams of electromagnetic resonators. **a**, A Fabry-Perot cavity formed from two mirrors. One of the mirrors is fixed; the other is part of a membrane that is free to vibrate. Electromagnetic waves are coupled into and out of the cavity via a partially transmissive input mirror. The length L of the cavity depends on the position of the membrane. **b**, An inductor-capacitor circuit. The capacitor is a parallel plate capacitor where one of the plates is a membrane that is free to vibrate. The separation d between the capacitor plates depends on the position of the membrane. Electromagnetic waves are coupled into and out of the resonator through a nearby transmission line, which is coupled to the inductor via a mutual inductance.

2.2 Electromagnetic resonators: cavities and circuits

In order to enhance the radiation pressure interaction, we must couple the membrane to an electromagnetic resonator. The membrane can be coupled to a Fabry-Perot cavity as diagrammed in Fig. 2.4a. This resonator geometry is often used to confine optical frequency electromagnetic fields [75], but in principle it can confine electromagnetic fields at any frequency [70]. Fabry-Perot cavities have been used to create high-finesse cavities for frequencies of several tens of gigahertz [76], but at lower frequencies the cavities become large and unwieldy as the wavelength of the electromagnetic fields increases. For these lower frequencies, other types of cavities (such as empty metal cylinders) more effectively confine electromagnetic fields [77]. Taken to the extreme, electrical components such as inductors and capacitors can be used to confine electromagnetic fields at the inductor-capacitor resonant frequency. This last type of resonator, which is commonly used in this thesis, is less of a 'cavity' and more of a 'circuit'. A membrane can be integrated into a circuit by making it one plate of a parallel plate capacitor, as diagrammed in Fig. 2.4b.

Electromagnetic resonators based on circuit components can be extremely compact with

dimensions much less than a wavelength. For example, the length L of the Fabry-Perot cavity diagrammed in Fig. 2.4a is usually many wavelengths but at a very minimum $L = \lambda/2$ where λ is the wavelength of the electromagnetic field at the cavity's resonant frequency of ω_0. However, there is no such restriction on the separation between the capacitor plates used in the microwave circuit and generally $d \ll \lambda$. The length scales of electromagnetic resonators are critical design parameters as they set the scale of the optomechanical interaction. For the Fabry-Perot cavity, when the membrane moves and alters the cavity length by a distance ΔL, the resonant frequency is changed by $\Delta\omega_0/\Delta L = \omega_0/L$. For the microwave circuit, an equivalent amount of motion Δd alters the resonant frequency by $\Delta\omega_0/\Delta d = \omega_0/2d$. For both resonators, smaller length scales yield larger optomechanical coupling.

Electromagnetic resonators based on circuit components are suitable for frequencies $\lesssim 100$ GHz, as low-loss circuit components for these frequencies can be microfabricated using superconducting materials. Such resonators are often formed by patterning metal films on dielectric substrates [78, 79]. Electromagnetic waves are coupled into and out of the resonator via a nearby transmission line, as is discussed in sections 3.3.1 and 4.2.2. The coupling between the resonator and the transmission line serves the same purpose as a partially transmissive mirror in a Fabry-Perot cavity. When cooled to cryogenic temperatures so that the metal film superconducts, these circuits form high quality microwave-frequency electromagnetic resonators.

Although many different forms of electromagnetic resonators exist, they all can be mathematically handled the same way. A confined electromagnetic mode couples to freely propagating electromagnetic fields. In the following description of electromagnetic resonators, based on coupled mode theory [80], I'll refer to a microwave resonator like the one diagrammed in Fig. 2.4b, but the mathematics applies equally well to other electromagnetic resonators.

2.2.1 Coupled-mode description of electromagnetic resonators

Energy in an electromagnetic resonator can be described with a complex field amplitude $a(t)$, where the normalization of $a(t)$ is chosen so that $|a(t)|^2$ gives the number of photons contained in

the resonator at time t. As the field amplitude evolves, energy in the resonator decays away. Some of this energy exits as electromagnetic fields that propagate down the transmission line. This loss can be chosen during resonator design, and I'll refer to it as the external loss rate. However, energy in the resonator can also be absorbed by, for example, two-level systems that form on the microwave circuit's surface [81, 82]. This type of loss is intrinsic to the exact construction of the electromagnetic resonator, and I'll refer to it as internal loss. The total energy loss rate is the sum of internal and external loss rates: $\kappa = \kappa_{\text{int}} + \kappa_{\text{ext}}$. Incorporating this loss rate into an equation of motion for field amplitude $a(t)$,

$$\begin{aligned} \dot{a}(t) &= \left(-\imath\omega_0 - \frac{\kappa}{2}\right) a(t) \\ a_{\text{out}}(t) &= \sqrt{\kappa_{\text{ext}}} a(t) \end{aligned} \tag{2.9}$$

where a_{out} is the amplitude of the field in the transmission line, and ω_0 is the resonant frequency of the resonator. The field amplitude a_{out} is normalized so that $|a_{\text{out}}|^2$ has units of photons/second. If $\kappa_{\text{ext}} = \kappa$, then all the energy initially in the resonator will come out of the transmission line: $|a(0)|^2 = \int_0^\infty |a_{\text{out}}(t)|^2 dt$.

Importantly, all loss channels for the resonator field $a(t)$ also drive it. Including driving terms into Eqns. 2.9 allows for a fully quantum description of a resonator that can be formally derived with input-output theory [83] (see section 2.5). Neglecting these driving fluctuations, we can still coherently drive the resonator via its coupling to a transmisssion line. This driving field can be incorporated as

$$\begin{aligned} \dot{a}(t) &= \left(-\imath\omega_0 - \frac{\kappa}{2}\right) a(t) + \sqrt{\kappa_{\text{ext}}} a_{\text{in}}(t) \\ a_{\text{out}}(t) &= \sqrt{\kappa_{\text{ext}}} a(t) - a_{\text{in}}(t) \end{aligned} \tag{2.10}$$

where a_{in} is the incoming field amplitude, normalized to have units of photon flux like a_{out}. The output field now consists of the reflected input field and fields emitted by the resonator. Eqns. 2.10 provide a description of electromagnetic resonators such as those shown in Fig 2.4. However, Eqns. 2.10 can be modified to incorporate different configurations of resonators and transmission

lines [23].

2.3 Mechanical oscillator displacement readout using electromagnetic fields

When a mechanical oscillator is embedded in an electromagnetic resonator as diagrammed in Fig. 2.4, the position of the oscillator affects the resonator's frequency. For example, an oscillator with a position $x(t) = x_0 \sin(\omega_m t)$ will modulate the resonant frequency and the equation of motion for the resonator field is now

$$\dot{a}(t) = \left(-\imath\left(\omega_0 + G x_0 \sin(\omega_m t)\right) - \frac{\kappa}{2}\right) a(t) + \sqrt{\kappa_{ext}} a_{in}(t) \tag{2.11}$$

where $G = \partial\omega_0/\partial x$ is a coupling constant with units of resonant frequency shift per unit motion. For the circuit diagrammed in Fig. 2.4b, with resonant frequency $\omega_0 \approx 1/\sqrt{LC}$, $G \approx \omega_0/2d$ where d is the separation between the capacitor plates. Similarly, $G \approx \omega_0/L$ for the Fabry-Perot cavity diagrammed in Fig. 2.4a.

Motion of the mechanical oscillator modulates the amplitude and phase of the energy in the electromagnetic resonator, and this motion appears in the electromagnetic field that leaves the resonator via the transmission line. This provides a way to observe motion of the mechanical oscillator via electromagnetic fields.

To observe mechanical motion, we pump the resonator with a non-zero $a_{in}(t)$. Information about the mechanical oscillator will be contained in $a_{out}(t)$, and this can be found by solving Eqn. 2.11. The homogeneous part of equation 2.11 has solutions

$$a_h(t) \propto \exp\left(\left(-\frac{\kappa}{2} - \imath\omega_0\right) t + \frac{\imath G x_0}{\omega_m} \cos(\omega_m t)\right). \tag{2.12}$$

Using the ansatz $a(t) = \tilde{a}(t) a_h(t)$, we have

$$\dot{\tilde{a}}(t) = \sqrt{\kappa_{ext}}\bar{a}_{in} \exp\left(\left(\frac{\kappa}{2} + \imath\omega_0 - \imath\omega_{in}\right) t - \frac{\imath G x_0}{\omega_m} \cos(\omega_m t)\right), \tag{2.13}$$

where I've assumed a monochromatic pump, $a_{in}(t) = \bar{a}_{in} e^{-\imath\omega_{in} t}$. Although Eqn. 2.13 can be directly integrated using a cylindrical wave expansion [84], if the motion of the mechanical oscillator shifts

the electromagnetic resonator's frequency by much less than ω_{m} ($Gx_0 \ll \omega_{\mathrm{m}}$), then

$$\dot{\tilde{a}}(t) \approx \sqrt{\kappa_{\mathrm{ext}}}\bar{a}_{\mathrm{in}} e^{\left(\frac{\kappa}{2}-\imath\Delta\right)t}\left(1-\frac{\imath G x_0}{2\omega_{\mathrm{m}}}\left(e^{\imath\omega_{\mathrm{m}}t}+e^{-\imath\omega_{\mathrm{m}}t}\right)\right) \tag{2.14}$$

where $\Delta = \omega_{\mathrm{in}} - \omega_0$. Eqn. 2.14 can be directly integrated and used to find the output field amplitude. Once transients have decayed away, the output field amplitude is

$$\begin{aligned} a_{\mathrm{out}}(t) = {} & \frac{\imath\Delta + \kappa_{\mathrm{ext}} - \kappa/2}{-\imath\Delta + \kappa/2}\bar{a}_{\mathrm{in}} e^{-\imath\omega_{\mathrm{in}}t} \\ & + \frac{Gx_0}{2}\frac{\kappa_{\mathrm{ext}}}{-\imath\Delta+\kappa/2}\bar{a}_{\mathrm{in}}\left(\frac{e^{-\imath(\omega_{\mathrm{in}}+\omega_{\mathrm{m}})t}}{-\imath(\Delta+\omega_{\mathrm{m}})+\kappa/2} - \frac{e^{-\imath(\omega_{\mathrm{in}}-\omega_{\mathrm{m}})t}}{-\imath(\Delta-\omega_{\mathrm{m}})+\kappa/2}\right). \end{aligned} \tag{2.15}$$

The output field consists of the reflected input field at frequency ω_{in}, and two modulation 'sidebands' at frequencies $\omega_{\mathrm{in}} + \omega_{\mathrm{m}}$ and $\omega_{\mathrm{in}} - \omega_{\mathrm{m}}$, as diagrammed in Fig. 2.5. These sidebands are weighted by the cavity Lorentzian of $(-\imath\omega + \kappa/2)^{-1}$ where ω is the sideband frequency. The power in the upper sideband at frequency $\omega_{\mathrm{in}} + \omega_{\mathrm{m}}$ is, in photons per second,

$$P_{\mathrm{usb}} = \left(\frac{Gx_0}{2}\right)^2 \frac{\kappa_{\mathrm{ext}}^2 \left|\bar{a}_{\mathrm{in}}\right|^2}{\Delta^2 + \kappa^2/4}\left(\frac{1}{(\Delta+\omega_{\mathrm{m}})^2 + \kappa^2/4}\right) \tag{2.16}$$

And similarly, the power in the lower sideband at frequency $\omega_{\mathrm{in}} - \omega_{\mathrm{m}}$ is, in photons per second,

$$P_{\mathrm{lsb}} = \left(\frac{Gx_0}{2}\right)^2 \frac{\kappa_{\mathrm{ext}}^2 \left|\bar{a}_{\mathrm{in}}\right|^2}{\Delta^2 + \kappa^2/4}\left(\frac{1}{(\Delta-\omega_{\mathrm{m}})^2 + \kappa^2/4}\right) \tag{2.17}$$

The power in the sidebands provides information about the amplitude of the oscillator's vibrations, and the phase of the sidebands relative to the pump provides information about the phase of the mechanical oscillator's vibrations. A larger pump field, $\bar{a}_{\mathrm{in}}$ increases the power in the sidebands, giving more and more precise information about the motion of the mechanical oscillator. Eventually, however, any measurement of the mechanical oscillator, if done stongly enough, must provide a momentum kick to the mechanical oscillator so that the position-momentum uncertainty relation is preserved [85, 72, 86]. This necessary dynamic is not included in this simple model of displacement readout. To be accurate, the radiation pressure force must be included in the mathematical description.

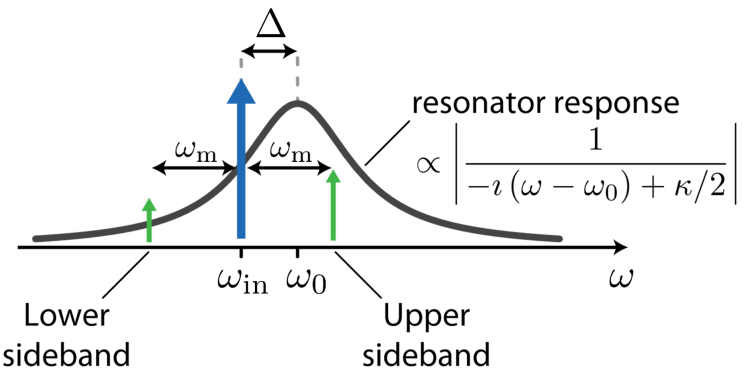

Figure 2.5: Displacement readout with electromagnetic fields. A monochromatic pump at frequency ω_{in} is injected into the electromagnetic resonator. The field emitted from the resonator is modulated by motion of the mechanical oscillator, producing 'sidebands' at frequencies $\omega_{\mathrm{in}}+\omega_{\mathrm{m}}$ and $\omega_{\mathrm{in}}-\omega_{\mathrm{m}}$. The amplitude of the sidebands is filtered by the resonator's frequency response, shown as the black curve.

2.4 Dynamical backaction

The photons in the electromagnetic resonator exert a force on the mechanical oscillator proportional to the average number of photons $|a|^2$ in the electromagnetic resonator. For an electromagnetic resonator, the force takes on the general form $F_{\mathrm{rp}} = -\hbar G|a|^2$ (the negative sign is a convention that a greater radiation pressure force decreases the resonant frequency of the cavity for positive G). Another way to view this force is that as the mechanical oscillator vibrates, it does work on the electromagnetic field [68]. Incorporating the radiation pressure force into an equation of motion for a damped mechanical oscillator, the equations of motion for the cavity opomechanical system are

$$\begin{aligned} \dot{a}(t) &= \left(-\imath\left(\omega_0 + Gx(t)\right) - \frac{\kappa}{2}\right) a(t) + \sqrt{\kappa_{\mathrm{ext}}} a_{\mathrm{in}}(t) \\ \ddot{x}(t) &= -\kappa_{\mathrm{m}}\dot{x}(t) - \omega_{\mathrm{m}}^2 x(t) - \hbar G|a(t)|^2/m_{\mathrm{eff}} \end{aligned} \tag{2.18}$$

where m_{eff} is the effective mass of the mechanical oscillator [23, 67], k_{m} its damping rate, ω_{m} its resonant frequency.

The equations of motion are nonlinear—the postion $x(t)$ depends on the square of the field amplitude $a(t)$. The radiation pressure interaction can be considered a type of Kerr nonlinearity,

as the electromagnetic resonant frequency is a function of the intensity of light in the resonator. In most experiments to date, the radiation pressure force is enhanced by driving the electromagnetic resonator with a strong, monochromatic pump. This pump effectively consumes the nonlinearity, thus rendering the equations of motion for the electromagnetic and mechanical modes linear, but it also enhances the radiation pressure interaction.

We mathematically pump the resonator with $a_{\rm in}(t) = \bar{a}_{\rm in} e^{\imath\omega_{\rm in} t}$, as in section 2.3. This pump populates the electromagnetic resonator with a steady state field amplitude $\bar{a} e^{-\imath\omega_{\rm in} t}$, and creates a net force on the mechanical oscillator. The equilibrium field amplitude $\bar{a}$ and oscillator position $\bar{x}$ can be found by setting the time derivatives Eqns. 2.18 to zero.

$$\bar{a} = \frac{\sqrt{\kappa_{\rm ext}}\bar{a}_{\rm in}}{-\imath\Delta + \kappa/2}, \qquad \bar{x} = \frac{-\hbar G|\bar{a}|^2}{m_{\rm eff}\omega_{\rm m}^2}, \tag{2.19}$$

where $\Delta = \omega_{\rm in} - \omega_0 - G\bar{x}$. We can examine the dynamics of the fluctuations of the field amplitude and oscillator postion about their steady state values, provided the steady-state solution is stable [87, 88]. Assuming a steady state solution exists, let $a \to e^{-\imath\omega_{\rm p} t}(\bar{a} + a(t))$ and $x \to \bar{x} + x(t)$ so that $a(t)$ and $x(t)$ represent fluctuations about equilibrium. Using these replacements in Eqns. 2.18, the dynamics of the fluctuations are described by

$$\begin{aligned} \dot{a}(t) &= (\imath\Delta - \kappa/2)a(t) - \imath G\bar{a}x(t) \\ \ddot{x}(t) &= -\omega_{\rm m}^2 x(t) - \kappa_{\rm m}\dot{x}(t) - \frac{\hbar G}{m_{\rm eff}}\left(\bar{a}a^*(t) + \bar{a}^* a(t)\right) \end{aligned} \tag{2.20}$$

where I've linearized the equations of motion by assuming the fluctuations $|a(t)| \ll |\bar{a}|$. Although the pump simplifies the dynamics of the cavity optomechanical system, it also greatly increases the coupling between the electromagnetic and vibrational modes. Every occurrence of the coupling G in Eqns. 2.20 is now accompanied by $\bar{a}$ or its conjugate, meaning that a stronger pump effectively increases the magnitude of the radiation pressure interaction.

The dynamics of the fluctuations $a(t)$ and $x(t)$ are easily observed in the frequency domain.

Transforming Eqns. 2.20 using $f(\omega) = \int_{-\infty}^{\infty} f(t)e^{\imath\omega t}dt$,

$$a(\omega)(-\imath(\Delta+\omega)+\kappa/2) = -\imath G\bar{a}x(\omega) \tag{2.21}$$

$$a^*(\omega)(\imath(\Delta-\omega)+\kappa/2) = \imath G\bar{a}^*x(\omega) \tag{2.22}$$

$$x(\omega)(-\omega^2+\omega_{\mathrm{m}}^2-\imath\omega\kappa_{\mathrm{m}}) = F_{\mathrm{rp}}(\omega)/m_{\mathrm{eff}} \tag{2.23}$$

where $F_{\mathrm{rp}}(\omega)$ is the force due to radiation pressure.

$$\begin{aligned} F_{\mathrm{rp}}(\omega) &= -\hbar G(\bar{a}a^*(\omega)+\bar{a}^*a(\omega)) \\ &= -\hbar G^2|\bar{a}|^2\left(\frac{\Delta+\omega}{(\Delta+\omega)^2+\kappa^2/4}+\frac{\Delta-\omega}{(\Delta-\omega)^2+\kappa^2/4}\right)x(\omega) \\ &\quad +\imath\hbar G^2|\bar{a}|^2\left(\frac{\kappa/2}{(\Delta+\omega)^2+\kappa^2/4}-\frac{\kappa/2}{(\Delta-\omega)^2+\kappa^2/4}\right)x(\omega) \end{aligned} \tag{2.24}$$

The linearized radiation pressure force, F_{rp} is only non-zero when the mechanical oscillator moves away from its equilibrium position: $F_{\mathrm{rp}}(\omega) \propto x(\omega)$. As such, the radiation pressure force consists of a real part that alters the mechanical resonant frequency and an imaginary part that alters mechanical damping.

Consider the susceptibility of the mechanical oscillator to an external force $F(\omega)$. The position of the oscillator can be described using $x(\omega) = \chi(\omega)F(\omega)$, where $\chi(\omega)$ is the mechanical oscillator's susceptibility. In the presence of $F_{\mathrm{rp}}(\omega)$,

$$\chi(\omega)^{-1} = -\omega^2+(\omega+\Omega(\omega))^2-\imath\omega(\kappa_{\mathrm{m}}+\Gamma(\omega)) \tag{2.25}$$

where $\Omega(\omega) = -\mathrm{Re}[F_{\mathrm{rp}}(\omega)]/(2m_{\mathrm{eff}}\omega_{\mathrm{m}}x(\omega))$ and $\Gamma(\omega) = \mathrm{Im}[F_{\mathrm{rp}}(\omega)]/(m_{\mathrm{eff}}\omega x(\omega))$. This radiation pressure-induced change in mechanical frequency and damping is the essence of dynamical backaction.

2.4.1 Weak-coupling regime

If the electromagnetic resonator has a broader frequency response than the mechanical oscillator, we can approximate $\Omega(\omega)$ and $\Gamma(\omega)$ in Eqn. 2.25 as frequency-independent parameters near the mechanical oscillator's resonant frequency. This approximation requires weak radiation

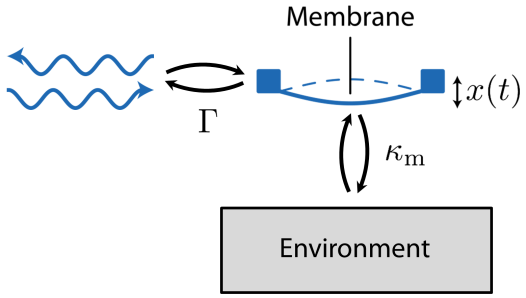

Figure 2.6: Radiation pressure-induced damping of a mechanical oscillator. The oscillator couples to its environment through its intrinsic loss at rate κ_{m}, but also to propagating microwave fields at rate Γ.

pressure coupling: $\kappa_{\mathrm{m}} + \Gamma \ll \kappa$. In this weak-coupling regime, the mechanical oscillator experiences a radiation pressure-induced frequency shift and damping of

$$\begin{aligned} \Omega &= |g|^2 \left[\frac{\Delta + \omega_{\mathrm{m}}}{(\Delta + \omega_{\mathrm{m}})^2 + (\kappa/2)^2} + \frac{\Delta - \omega_{\mathrm{m}}}{(\Delta - \omega_{\mathrm{m}})^2 + (\kappa/2)^2} \right] \\ \Gamma &= |g|^2 \left[\frac{\kappa}{(\Delta + \omega_{\mathrm{m}})^2 + (\kappa/2)^2} - \frac{\kappa}{(\Delta - \omega_{\mathrm{m}})^2 + (\kappa/2)^2} \right] \end{aligned} \tag{2.26}$$

where $g = \sqrt{\hbar/2m_{\mathrm{eff}}\omega_{\mathrm{m}}} G\bar{a}$.

The additional damping Γ can be either positive or negative. For positive damping, which is used throughout this thesis, energy stored as vibrations of the mechanical oscillator leaves through two separate channels as diagrammed in Fig. 2.6. First, energy is lost to the mechanical oscillator's environment at a rate κ_{m}. Second, energy is converted into electromagnetic fields at a rate Γ. The additional damping provided by radiation pressure can be used to cool the mechanical oscillator: Motion induced by the oscillator's thermal environment is rapidly converted into electromagnetic fields, leaving the oscillator with less net motion as if it has been cooled [29, 30, 31].

2.4.2 Resolved-sideband regime

The additional damping Γ has both positive and negative contributions as seen in Eqn. 2.26. $\Gamma = \Gamma_+ - \Gamma_-$ where

$$\Gamma_+ = |g|^2 \frac{\kappa}{(\Delta + \omega_{\mathrm{m}})^2 + (\kappa/2)^2}\ , \qquad \Gamma_- = |g|^2 \frac{\kappa}{(\Delta - \omega_{\mathrm{m}})^2 + (\kappa/2)^2}\ . \tag{2.27}$$

The negative contribution to damping Γ_- amplifies the mechanical oscillator's motion and the positive contribution Γ_+ damps and cools the oscillator. The ratio of the amplification rate to the cooling rate determines how much entropy can be removed from the mechanical oscillator [33, 34]. When $4\omega_{\rm m} \gg \kappa$, the system is in the resolved sideband regime and to a good approximation either Γ_+ or Γ_- can be heavily suppressed. In the resolved-sideband regime with $\Delta = -\omega_{\rm m}$, Γ_- is negligible and $\Gamma = 4|g|^2/\kappa$. Cavity optomechanical systems in this regime have been used to cool a mechanical oscillator to near its ground state of motion [35, 36, 37].

2.5 Heisenberg-Langevin equations of motion

The electromagnetic resonator and the mechanical oscillator have similar dynamics: Both can be modeled as harmonic oscillators. However, sections 2.3 and 2.4 emphasize the position of the mechanical oscillator. To highlight the similarity between the electromagnetic resonator and the mechanical oscillator mode, we can reformulate Eqns. 2.20 using a field amplitude $c(t)$ rather than displacement $x(t)$. The two representations are related through $x(t) = x_{\rm zpf}\left(c(t) + c^*(t)\right)$, where $x_{\rm zpf} = \sqrt{\hbar/(2m_{\rm eff}\omega_{\rm m})}$ are the zero-point fluctuations of the mechanical oscillator. Using this relation,

$$\begin{aligned}
\dot{a}(t) &= (\imath\Delta - \kappa/2)a(t) - \imath g(c(t) + c^*(t)) + \sqrt{\kappa_{\rm ext}}a_{\rm in}(t) + \sqrt{\kappa_{\rm int}}a_0(t) \\
\dot{c}(t) &= (-\imath\omega_{\rm m} - \kappa_{\rm m}/2)c(t) - \imath\left(ga^*(t) + g^*a(t)\right) + \sqrt{\kappa_{\rm m}}c_{\rm in}(t)
\end{aligned} \tag{2.28}$$

Eqn. 2.28 includes all the possible couplings that can drive the electromagnetic resonator or the mechanical oscillator, as diagrammed in Fig. 2.7. The terms $a_{\rm in}(t)$ and $a_0(t)$ drive the electromagnetic resonator through the coupled transmission line and internal resonator loss, respectively. These terms are in the same rotating frame as the fluctuations $a(t)$. Additionally, $c_{\rm in}(t)$ drives the mechanical oscillator through its internal loss mechanism. Eqns. 2.28, along with the relation $a_{\rm out}(t) = \sqrt{\kappa_{\rm ext}}a(t) - a_{\rm in}(t)$, form a complete description of linear optomechanics.

The resonator field amplitude $a(t)$ and $a^*(t)$ and the mechanical oscillator amplitude $c(t)$ and $c^*(t)$ can be directly promoted to creation and annihilation operators. The resulting Heisenberg-

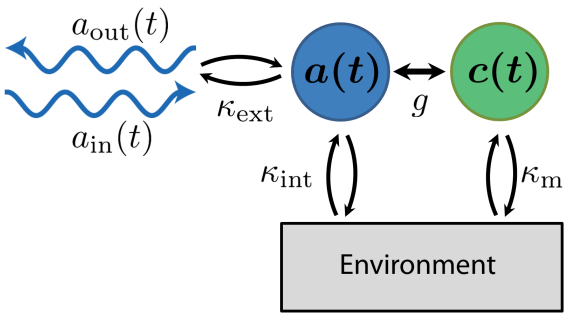

Figure 2.7: An optomechanical system consists of two coupled harmonic oscillators: an electromagnetic resonator, described by field amplitude $a(t)$, and a mechanical oscillator described by field amplitude $c(t)$. Both the electromagnetic resonator and the mechanical oscillator are coupled through some intrinsic loss rate to their environment, and the electromagnetic resonator is additionally coupled to a transmission line.

Langevin equations of motion can be formally derived starting from a Hamiltonian formulation and input-output theory [89, 83, 90].

Eqns. 2.28 are first order, linear differential equations. As such, much of linear control theory [91, 92] can be applied. The framework of control theory provides an extremely general and powerful tool for predicting and modeling the behavior of optomechanical systems. System dynamics are described with a state space model that has the general structure

$$\begin{aligned} \dot{\mathbf{x}}(t) &= A(t)\mathbf{x}(t) + B(t)\mathbf{u}(t) \\ \mathbf{y}(t) &= C(t)\mathbf{x}(t) + D(t)\mathbf{u}(t) \end{aligned} \tag{2.29}$$

Here, $\mathbf{u}(t)$ is a vector of inputs that drive the system, $\mathbf{y}(t)$ is a vector of outputs, and $\mathbf{x}(t)$ is the vector that describes the state of the system. The matrix A describes how the state of the system evolves in time, and B controls how the inputs to the system affect the state of the system. Matrices C and D control how the state of the system and the inputs map onto the outputs of the system.

The dynamics of a cavity optomechanical system can be described using

$$\mathbf{x} = \begin{bmatrix} a(t) \\ c(t) \\ a^\dagger(t) \\ c^\dagger(t) \end{bmatrix}, \ \mathbf{y} = \begin{bmatrix} a_{\text{out}}(t) \\ a^\dagger_{\text{out}}(t) \end{bmatrix}, \ \mathbf{u} = \begin{bmatrix} a_{\text{in}}(t) \\ a_0(t) \\ c_{\text{in}}(t) \\ a^\dagger_{\text{in}}(t) \\ a^\dagger_0(t) \\ c^\dagger_{\text{in}}(t) \end{bmatrix} \tag{2.30}$$

$$A = \begin{bmatrix} \imath\Delta - \kappa/2 & -\imath g(t) & 0 & -\imath g(t) \\ -\imath g^* & -\imath\omega_{\text{m}} - \kappa_{\text{m}}/2 & -\imath g & 0 \\ 0 & \imath g^* & -\imath\Delta - \kappa/2 & \imath g^*(t) \\ \imath g^* & 0 & \imath g & \imath\omega_{\text{m}} - \kappa_{\text{m}}/2 \end{bmatrix}, \ C = \begin{bmatrix} \sqrt{\kappa_{\text{ext}}} & 0 & 0 & 0 \\ 0 & 0 & \sqrt{\kappa_{\text{ext}}} & 0 \end{bmatrix}$$

$$B = \begin{bmatrix} \sqrt{\kappa_{\text{ext}}} & \sqrt{\kappa_{\text{int}}} & 0 & 0 & 0 & 0 \\ 0 & 0 & \sqrt{\kappa_{\text{m}}} & 0 & 0 & 0 \\ 0 & 0 & 0 & \sqrt{\kappa_{\text{ext}}} & \sqrt{\kappa_{\text{int}}} & 0 \\ 0 & 0 & 0 & 0 & 0 & \sqrt{\kappa_{\text{m}}} \end{bmatrix}, \ D = \begin{bmatrix} -1 & 0 & 0 & 0 & 0 & 0 \\ 0 & 0 & 0 & -1 & 0 & 0 \end{bmatrix}. \tag{2.31}$$

These vectors and matrices when used in Eqns. 2.29 reproduce Eqns. 2.28 and the input-output relation $a_{\text{out}}(t) = \sqrt{\kappa_{\text{ext}}}a(t) - a_{\text{in}}(t)$.

2.5.1 Transfer function of optomechanical system

If matrices A, B, C, and D are time invariant, a system transfer function $\Xi(\omega)$ compactly describes how inputs $\mathbf{u}$ are taken to outputs $\mathbf{y}$: $\mathbf{y}(\omega) = \Xi(\omega)\mathbf{u}(\omega)$. [1]

$$\Xi(\omega) = C\left(\imath\omega I - A\right)^{-1} B + D \tag{2.32}$$

[1] The transfer function is computed in Laplace space, where $f(s) = \int_{-\infty}^{\infty} f(t)e^{-st}dt$. This is equivalent to Fourier space so long as we take $s \to -\imath\omega$.

In the context of cavity optomechanics, $\Xi(\omega)$ describes how a signal at frequency ω above the pump will propagate from an input to the outputs. This method is used in chapter 3 to describe the dynamics of microwave to optical conversion.

2.5.1.1 Transfer function and scattering parameters

For time-invariant systems, the transfer function can be measured in the lab by injecting a monochromatic signal and measuring the emitted signal. Comparing the emitted signal to the injected signal yields the amplitude and phase shift of the signal which can be recast as the real and imaginary parts of one component of the transfer function matrix $\Xi(\omega)$. This measurement is commonly performed in microwave-frequency laboratories with a network analyzer [70]. The close tie between mathematical model and experimental characterization make the transfer function an extremely useful tool. In microwave network analysis, the transfer function $\Xi(\omega)$ is sometimes referred to as the scattering matrix, and each element of the matrix as a scattering parameter.

2.5.1.2 Noise analysis using the transfer function

Noise properties of an output electromagnetic field can also be predicted using the transfer function formalism. The spectral density $\mathcal{S}(\omega)$ of the output fields is [93, 94]

$$2\pi\mathcal{S}(\omega)\delta(\omega-\omega') = \left\langle [\mathbf{y}(\omega')]^\dagger \mathbf{y}^T(\omega)\right\rangle = \Xi^*(\omega')\left\langle [\mathbf{u}(\omega')]^\dagger \mathbf{u}^T(\omega)\right\rangle \Xi^T(\omega) \tag{2.33}$$

More compactly, $\mathcal{S}(\omega) = \Xi^*(\omega)\Sigma\Xi^T(\omega)$ where $\Sigma = (2\pi\delta(\omega-\omega'))^{-1}\left\langle [\mathbf{u}(\omega')]^\dagger \mathbf{u}^T(\omega)\right\rangle$.

The correlation matrix Σ describes the noise properties of the inputs. If the system is driven by noise from its thermal environment—that is, blackbody radiation or Johnson noise [95]—the elements of Σ have a simple form [93]. For example, $\left\langle [\hat{a}_{\rm in}(\omega')]^\dagger \hat{a}_{\rm in}(\omega)\right\rangle = 2\pi\delta(\omega-\omega')n_{\rm in}$, where $n_{\rm in}$ is the Bose-Einstein occupation factor for the transmission line modes. Thus, the $(1,1)$ component of Σ will have the value $n_{\rm in} = 1/(e^{\hbar\omega/k_{\rm B}T}-1)$ where T is the temperature of the modes in the transmission line. If the electromagnetic resonator has a narrow freqeuency response ($\kappa \ll \omega_0$), we can approximate $\omega \approx \omega_0$ in the expression for $n_{\rm in}$. For $k_{\rm B}T \gg \hbar\omega_0$, $n_{\rm in} \approx k_{\rm B}T/\hbar\omega_0$, which is the

same as Johnson noise expressed in units of photons/sec·Hz. If all the ports of the optomechanical system are driven by thermal noise, then

$$\Sigma = \begin{bmatrix} n_{\mathrm{in}} & 0 & 0 & 0 & 0 & 0 \\ 0 & n_0 & 0 & 0 & 0 & 0 \\ 0 & 0 & n_{\mathrm{m}} & 0 & 0 & 0 \\ 0 & 0 & 0 & n_{\mathrm{in}}+1 & 0 & 0 \\ 0 & 0 & 0 & 0 & n_0+1 & 0 \\ 0 & 0 & 0 & 0 & 0 & n_{\mathrm{m}}+1 \end{bmatrix}. \tag{2.34}$$

In order to perform low-noise measurement and manipulation of a mechanical oscillator using an electromagnetic resonator, it is crucial to minimize n_{in} and n_0. For a microwave circuit with $\omega_0 = 2\pi \times 7$ GHz, $n_0 < 1$ requires a temperature of $T < 300$ mK. For this reason, manipulation of mechanical oscillators using a microwave frequency electromagnetic resonator is often performed at low temperatures of <50 mK attained with a dilution refrigerator [96]. Furthermore, the transmission line connecting to the electromagnetic resonator must be driven by Johnson noise from a cold (ideally <50 mK) source resistance so that $n_{\mathrm{in}} \ll 1$. Achieving this in practice means utilizing components like cryogenic attenuators, directional couplers, and circulators as shown in Appendix D.

Even though the electromagnetic resonator can be driven by vacuum fluctuations ($n_{\mathrm{in}} = n_0 = 0$), the mechanical oscillator can have a significant driving term $n_{\mathrm{m}} \gg 1$. Even at a temperature $T = 50$ mK, a mechanical oscillator with frequency $\omega_{\mathrm{m}} = 2\pi \times 10$ MHz will have an average thermal occupancy of $n_{\mathrm{m}} \approx 100$. This additional noise can be avoided by using mechanical oscillators with resonant frequencies of several GHz [97, 98, 99]. For mechanical oscillators with resonant frequencies from kHz to many MHz, the thermal fluctuations driving the mechanical oscillator are almost always the largest noise source for the optomechanical system.

Finally, I want to point out that the 'quantum' aspect of this input-output formalism is the asymmetry between the operators for the input fields. For example, $\left\langle [\hat{a}_{\mathrm{in}}(\omega')]^\dagger \hat{a}_{\mathrm{in}}(\omega) \right\rangle = 2\pi\delta(\omega - \omega')n_{\mathrm{in}}$ and $\left\langle \hat{a}_{\mathrm{in}}(\omega')[\hat{a}_{\mathrm{in}}(\omega)]^\dagger \right\rangle = 2\pi\delta(\omega - \omega')(n_{\mathrm{in}}+1)$. This asymmetry exists, of course, because the

creation and annihilation operators do not commute [94]: $\left[a_{\text{in}}(\omega'), [a_{\text{in}}(\omega)]^\dagger\right] = 2\pi\delta(\omega - \omega')$. Without this asymmetry in the correlation matrix Σ, all the dynamics and noise properties of the cavity optomechanical system are entirely classical.

2.5.2 Time-dependent system dynamics

Although in our experiments the matrices B, C, and D in Eqn. 2.29 are approximately time independent, A can be time dependent. The mean field amplitude in the electromagnetic resonator, $\bar{a}$, is determined by the strength of the pump, as seen in Eqns. 2.19. By varying the amplitude of the pump, $g = G\bar{a}x_{\text{zpf}}$ can be made time dependent so that $g \rightarrow g(t)$ and $A \rightarrow A(t)$. Additionally, the pump has a phase and this determines the phase of $\bar{a}$. Altering the phase of the pump by π changes the sign of $\bar{a}$ and this changes the sign of the pump-enhanced radiation pressure coupling. These dynamics provide an extremely convenient way to control and tune the radiation pressure interaction.

For time domain signal processing demonstrated in chapter 4, it is necessary to modulate the coupling $g(t)$ between the electromagnetic resonator and the mechanical oscillator. Although the transfer function approach of section 2.5.1 does not fail with a time-dependent A matrix, it is no longer as useful in understanding the system dynamics. Instead, equations 2.29 can be directly integrated or numerically solved to predict the system dynamics. For example, equations 2.29 are discretized and numerically solved to predict the effect of the time-dependent optomechanical interaction used in chapter 4.

Chapter 3

Microwave to optical frequency conversion with a mechanical oscillator

The radiation pressure interaction between light and a mechanical oscillator is inherently broadband: electromagnetic signals at most frequencies can interact with a mechanical oscillator, as initially indicated in chapter 2. In this chapter, we utilize the broadband nature of the radiation pressure interaction to convert electromagnetic signals between microwave and optical frequencies. We couple two electromagnetic resonators—one at a microwave frequency, one at an optical frequency—to the same mechanical oscillator. The dynamical backaction of the resonator fields on the mechanical oscillator, as introduced in section 2.4, allows a microwave signal sent into the electro-opto-mechanical frequency converter to stream through the mechanical oscillator and emerge as an optical signal, and vice-versa. This process can be remarkably efficient, and we demonstrate photon number conversion efficiencies of $\sim$10%. Although the demonstrated conversion adds significant noise due to thermally driven vibrations of the mechanical oscillator, conversion can in principle be noiseless and we anticipate nearly noiseless frequency conversion is achievable with modest modifications.

3.1 The need for a microwave-to-optical quantum link

Modern communication networks manipulate information at several gigahertz with microprocessors and distribute information at hundreds of terahertz via optical fibers. The division of labor between these different frequencies did not occur by chance, but was in part directed by nature. Silica has a natural minimum of absorption and scattering of light at wavelength $\lambda = 1550$ nm. This

has led to low-loss optical fibers suitable for distributing signals at this wavelength [100]. Similarly, the rise of silicon-based integrated circuits has enabled low-cost manipulation of electrical signals [101]. Combining the processing power available to electrical signals with the efficient distribution available to optical signals has ushered in an era of high-speed internet connectivity.

A similar frequency dichotomy is developing in quantum information processing. Superconducting qubits operating at several gigahertz have recently emerged as promising high-fidelity and intrinsically scalable quantum processors [102, 103, 104]. Conversely, optical frequencies provide access to low-loss transmission [46, 100] and long-lived quantum-compatible storage [45, 105, 106]. Converting information between gigahertz-frequency 'microwave light' that can be deftly manipulated and terahertz-frequency 'optical light' that can be efficiently distributed will potentially enable small-scale quantum systems [107, 108, 109] to be combined into larger, fully-functional quantum networks [41, 110]. But no current technology can transform information between these vastly different frequencies while preserving the fragile quantum state of the information. For this demanding application, a frequency converter must provide a near-unitary transformation between microwave light and optical light; that is, the ideal transformation is coherent, lossless and noiseless.

Traditionally, nonlinear materials such as lithium niobate are used to create electro-optic modulators (EOMs) that connect microwave and optical light. Although EOMs are in principle capable of quantum frequency conversion [111, 112], such conversion has not yet been demonstrated, and current EOMs [113, 114, 115] have predicted photon number efficiencies of only a few 10^{-4} [114, 111, 112]. Although these technical challenges might be overcome in the future, there is a technological vacuum that has been filled with proposed routes to a quantum link between microwave and optical light. Proposed methods of frequency conversion utilize clouds of ultracold atoms [116, 117, 118], nitrogen-vacancy centers in diamond [119], rare-earth doped crystals [120, 121], and mechanical oscillators [52, 122, 99]. All these proposed frequency converters face the challenge of integrating optical light with the cryogenic temperatures needed for low-noise microwave signals and superconducting circuitry.

Experimental interest in using mechanical oscillators for microwave-to-optical frequency con-

version began around 2011 when both microwave light and optical light were used to cool mechanical oscillators to near the ground state of motion [55, 37]. Since this time, experiments have demonstrated coupling between MHz-frequency signals and optical light using mechanical oscillators [123, 124, 125], and show promise for microwave-to-optical frequency conversion. Another approach uses a combination of piezoelectricity and radiation pressure to couple microwave signals to optical frequencies [99]. This chapter describes the construction and measurement of a microwave-to-optical converter based on a mechanical oscillator [122]. The converter operates at cryogenic temperatures and the frequency conversion is shown to be both bidirectional and highly efficient.

3.2 A frequency converter forms a two-port network

From an experimental point of view, a frequency converter can be viewed as a 'black box' that has a microwave frequency port and an optical frequency port, as diagrammed in Fig. 3.1a. The converter must be characterized using these ports alone. We can characterize the coherent response of the converter by, for example, injecting a microwave field at frequency ω into the converter and comparing it to the outgoing optical field at frequency $\omega_c + \omega$, where ω_c is the frequency change added by the converter. This measurement yields one element of the transfer function matrix $\Xi(\omega)$ as defined in section 2.5.1. In the language of microwave engineering, each element of the transfer function corresponds to a single scattering parameter of the network. For a two port network such as the frequency converter, four S-parameters describe the network [70] as detailed in Fig. 3.1b.

Without knowledge of the internal dynamics of the converter, we can still generate criteria for an ideal frequency converter. First, we would like the converter to preserve the number of photons in a signal. The fields $b_{\text{in}}(\omega)$ and $a_{\text{out}}(\omega)$ in Fig. 3.1b have units of $(\text{number}\times\text{sec})^{1/2}$ as in section 2.2.1, and so the apparent photon number efficiency for upconversion can be expressed as $|S_{21}(\omega)|^2 = |a_{\text{out}}(\omega_c + \omega)/b_{\text{in}}(\omega)|^2$. Ideally, $|S_{21}(\omega)|^2 = 1$ and the converter has no loss and no photon number gain. Although gain might be beneficial for some applications [126], gain necessarily adds noise [127] that will corrupt quantum signals. If conversion has no gain and has unit efficiency,

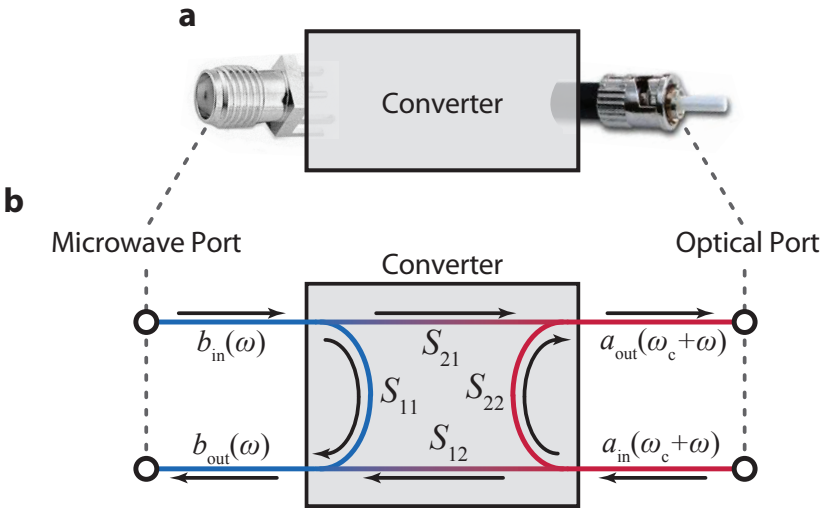

Figure 3.1: Scattering parameters of a frequency converter. **a**, All frequency converters have a microwave port and an optical port, here represented by an SMA connector and a fiber connector, respectively. **b**, Transmission and reflection of a frequency converter can be characterized by scattering parameters. For example, the transmission for upconversion, $S_{21}(\omega)$, can be found by measuring the quantity $a_{\text{out}}(\omega_c+\omega)/b_{\text{in}}(\omega)$ with $a_{\text{in}}(\omega) = 0$, where ω_c is the frequency change added by the converter.

there can be no reflected microwave signal: The ideal converter is impedance matched and $S_{11}(\omega) = b_{\text{out}}(\omega)/b_{\text{in}}(\omega) = 0$. Finally, if frequency conversion is lossless and adds no noise to the converted signal, it can be reversed and undone. As an initial indication of reversibility, the conversion process should be reciprocal or bidirectional: $S_{21}(\omega) = S_{12}(\omega)$. A perfectly efficient, impedance-matched, and bidirectional converter is a significant step toward quantum frequency conversion.

These three criteria can be satisfied with a frequency converter based on a mechanical oscillator. Section 3.3 describes the construction of an electro-opto-mechanical frequency converter. Section 3.4 predicts the performance of this frequency converter with respect to the three criteria, and section 3.6 demonstrates that our converter begins to meet all criteria. However, frequency conversion with a mechanical oscillator can add noise to the converted signal, as discussed in section 3.4.3. Reducing added noise is a crucial challenge, and in section 3.6.3 we demonstrate a reduction of added noise that can in principle be extended to create a quantum frequency converter.

Although low added noise and high conversion efficiency imply the converter is suitable for

conversion of quantum states, an unambiguous demonstration of quantum frequency conversion is necessary. The experiments presented here are progress toward this goal, but quantum frequency conversion is a task for future graduate students.

3.3 Construction of electro-opto-mechanical frequency converter

Coupling electromagnetic fields and mechanical oscillators was pioneered in the 1970s and 1980s [20, 128, 88], but not until recently has the strength of the radiation pressure coupling been enhanced to the point that technological goals, such as quantum frequency conversion [129, 130, 131, 132, 90], seem within reach. A key development was the discovery that silicon nitride membranes have outstanding mechanical and optical properties [133]. When placed between two mirrors that form a high-finesse Fabry-Perot cavity, the vibrations of the silicon nitride membrane couple to the electromagnetic field confined in the cavity [134, 135]. At microwave frequencies, state-of-the-art experiments use metallic membranes to create low-loss capacitors that naturally couple membrane vibrations to electrical signals [136, 55]. These experiments require cryogenic temperatures both to eliminate Johnson noise at microwave frequencies and to create low-loss superconducting circuits. Our frequency converter leverages advances in both types of optomechanical systems. It includes a Fabry-Perot cavity that forms an optical-frequency electromagnetic resonator and an inductor-capacitor circuit that forms a microwave-frequency electromagnetic resonator at cryogenic temperatures. A silicon nitride membrane spans these two electromagnetic resonators, as shown in Fig. 3.2.

The challenge of constructing an electro-opto-mechanical system is integration of the two electromagnetic resonators. The optical cavity must operate at cryogenic temperatures needed by the microwave circuit, and the microwave circuit must operate in close proximity to the Fabry-Perot cavity, where light in the cavity can potentially interact with the microwave circuit. In particular, high-frequency photons absorbed by a superconducting microwave circuit adversely affect its performance [137]. Photons with energy greater than the superconducting gap (which for niobium corresponds to a photon frequency of ≈ 1 THz) can break cooper pairs apart into their

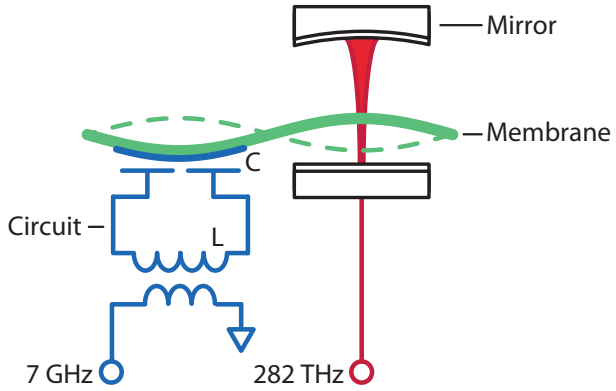

Figure 3.2: Schematic of a microwave-to-optical frequency converter. The converter consists of a silicon nitride membrane coupled to a microwave-frequency electromagnetic resonator formed from an inductor-capacitor circuit and an optical-frequency electromagnetic resonator formed from two high-reflectivity mirrors. Propagating electromagnetic fields are coupled to the microwave resonator with an inductive coupler, and to the optical resonator with a slightly transmissive input mirror.

individual electrons. Unpaired electrons cause additional loss in the circuit in a manner similar to an increased temperature of the entire superconductor [138]. Although changes in the number of unpaired electrons can be used to detect photons [78, 79], for a frequency converter we need the microwave circuit to be unaffected by the amount of light in the Fabry-Perot cavity.

We begin constuction of the frequency converter with a physically large silicon nitride membrane (dimensions of 1 mm by 1 mm by 90 nm thick) so that the superconducting microwave circuit and the Fabry-Perot cavity can couple to physically distant portions of the silicon nitride membrane. The membrane is fabricated using standard photolithographic techniques [139, 140] that create a silicon nitride membrane held in place by a silicon frame. Additionally, we cover a portion of the membrane with niobium for use in the superconducting circuit. A picture of the metallized silicon nitride membrane is shown in figure 3.3a.

3.3.1 Construction of microwave circuit

To couple the silicon nitride membrane to a microwave circuit, we pattern a thin film of niobium on a separate silicon substrate as shown in Fig. 3.3b. This substrate contains the majority

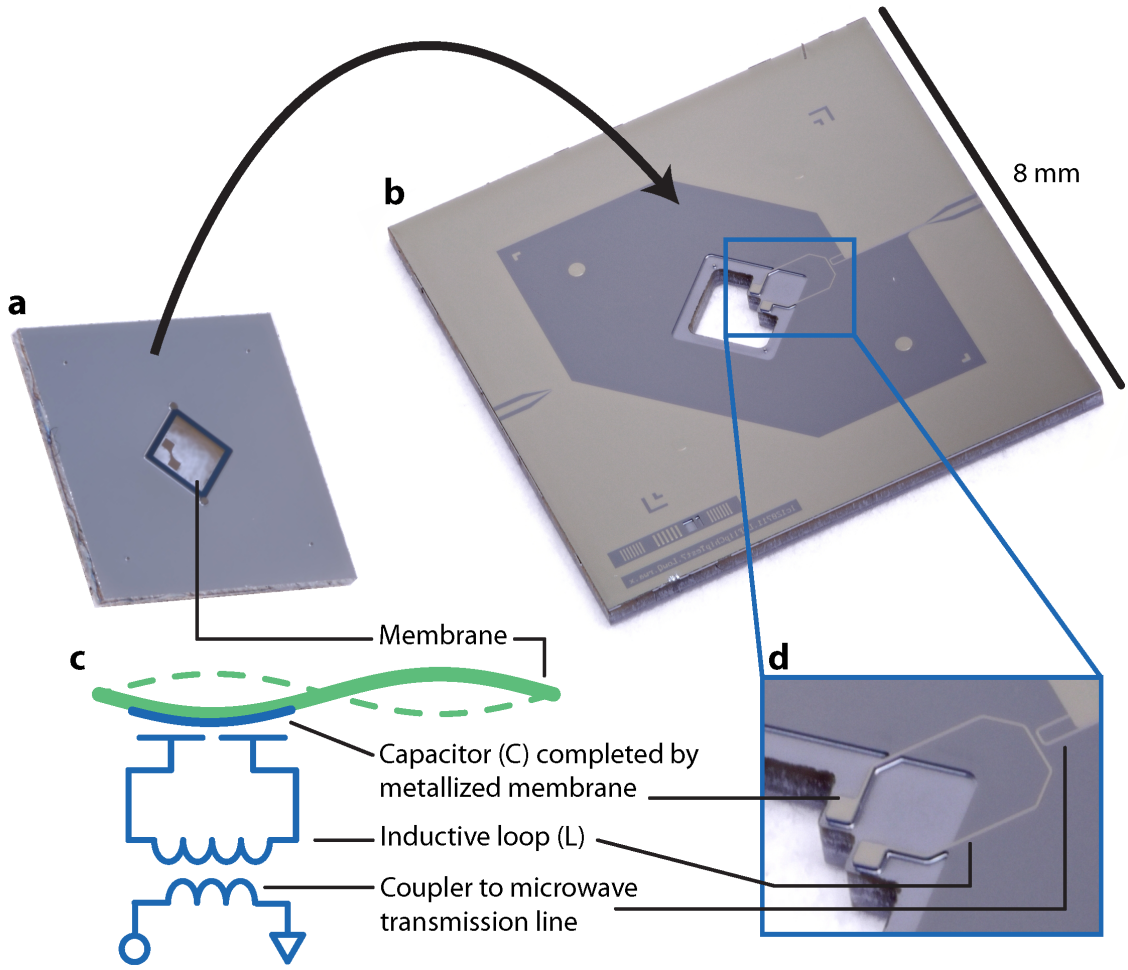

Figure 3.3: Construction of a 'flip-chip' microwave circuit. **a**, A silicon frame supports the silicon nitride membrane. The silicon nitride appears clear, but the niobium metallization appears as a gray-colored bowtie shape on the silicon nitride. **b**, Partially complete microwave circuit created by patterning a niobium film on a silicon substrate. The microwave circuit is completed when the membrane is flipped over onto this circuit and attached. **c**, Schematic depiction of the completed microwave circuit. **d**, Expanded view of microwave circuitry.

of the microwave circuitry, including a transmission line that allows microwave signals to be coupled into and out of the circuit, and is designed to mate with the metallized silicon nitride membrane to form a complete inductor-capacitor circuit. The circuitry and the membrane are brought into close proximity to form what we call a 'flip-chip' microwave circuit. An electrical diagram of the flip-chip is shown in Fig. 3.3c.

We require a large electromechanical coupling $G_e = \partial\omega_e/\partial x$ where ω_e is the resonant frequency of the microwave circuit and x describes the position of the silicon nitride membrane. For the inductor and parallel-plate capacitor circuit shown in Fig. 3.3c, the electromechanical coupling is $G_e \approx \omega_e/(2d)$ where d is the separation between the two plates of the parallel plate capacitor, indicating that small plate separations are necessary for large G_e. A key engineering aspect of creating small separations is removal of any unnecessary material. Less material at the interface between the circuitry and membrane reduces the chance that particulate will prevent the capacitor plates from reaching the desired separation distance. Using material removal as a design rule, the flip-chip microwave circuits consistently have parallel-plate capacitors with plate separations of $d \approx 400$ nm. This separation yields an electromechanical coupling of $G_e \approx 2\pi \times 4$ MHz/nm. An assembled flip-chip and its profile are shown in figure 3.4, and fabrication details are given in Appendix A.

Vibrational excitations of the membrane can radiate out into an acoustically lossy environment, which can limit the the quality factor of vibrational modes of the membrane [65, 73]. In an attempt to decouple vibrational modes of the membrane and its supporting silicon frame from other lossy vibrational modes, we assemble the flip chip with a small amount of Stycast 2850FT epoxy. We have found this assembly process to be compatible with high quality factor vibrational modes of the membrane, as shown in Fig. 2.3.

To integrate the flip-chip with an optical cavity, we must mount and connectorize it in an appropriate way. We attach the flip-chip with epoxy to a copper-plated Invar bracket designed for direct integration with a Fabry-Perot cavity. Invar is our material of choice for use in the Fabry-Perot cavity (see section 3.3.2), but copper is necessary to create a controlled electromagnetic

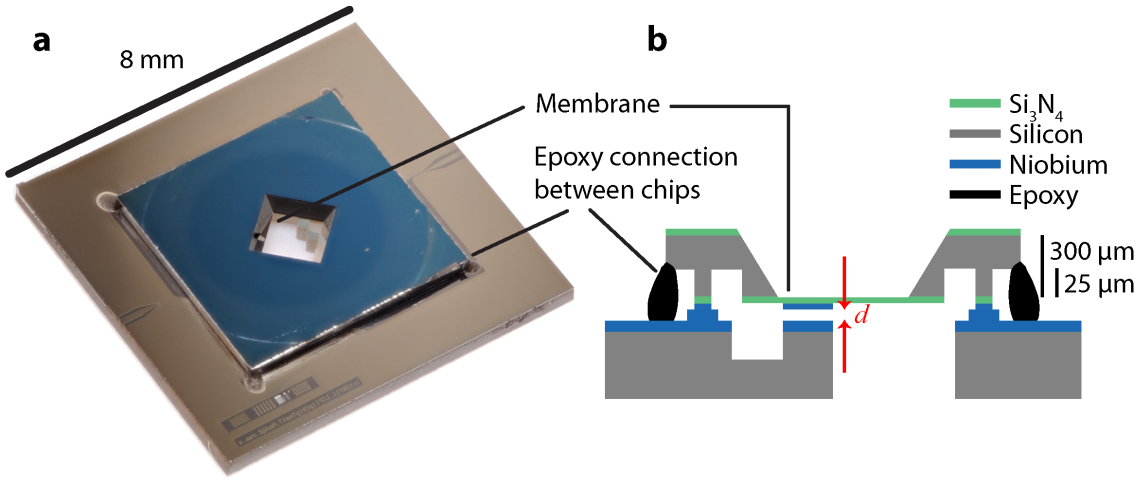

Figure 3.4: **a**, Picture of an assembled flip-chip. Note the large, approximately 1mm by 1mm central area that will allow optical frequency light to interact with the silicon nitride membrane. **b**, Schematic profile of the assembled flip-chip. Importantly, only the posts that hold the chips apart and the capacitor plates of the microwave circuit are within 400 nm of each other ($d \approx 400$ nm). All other surfaces are > 25 μm apart.

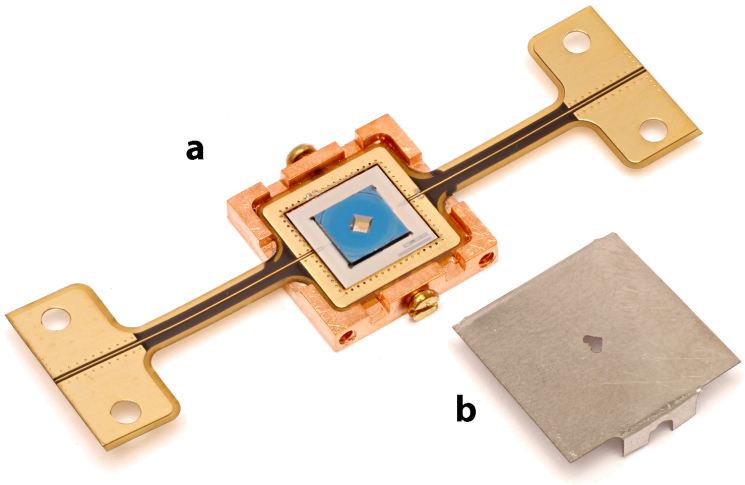

Figure 3.5: Packaged flip-chip microwave circuit. **a**, Flip-chip is mounted on a copper-plated Invar substrate, which simultaneously provides a low-loss electromagnetic environment for the microwave circuit and low thermal contraction required for the cryogenically compatible Fabry-Perot cavity. A flexible microstrip transmission line connects to the microwave circuit, and also connects to a coaxial cable via a commercially available connector (not shown). **b**, A niobium shim, once attached to the top of the copper-plated Invar, blocks most stray light from reaching the microwave circuit. The niobium shim is necessary to protect the superconductivity of the microwave circuit when it is placed in a Fabry-Perot cavity (see section 3.3.3).

environment for the microwave circuit. Without a high-conductivity ground plane, magnetic fields in the microwave circuit will induce eddy currents in the Invar that will dissipate energy in the microwave circuit. We couple microwave signals into and out of the circuit via a flexible circuit board made from copper rolled onto a polyimide substrate [141]. The copper is patterned to form a microstrip transmission line. Although the microstrip transmisison line forms a robust electrical connection to the microwave circuit, it creates only a weak mechanical connection. This ensures that forces applied to the circuit board will not influence the exact position of the silicon nitride membrane, whose placement is critical for successful operation of the optical cavity. A packaged flip-chip is shown in figure 3.5. Importantly, the entire structure can be placed in a high-finesse Fabry-Perot cavity: The flip-chip and package contain a large central area that is completely free of metal and silicon as can be seen in Fig. 3.4a and Fig. 3.5a. This open area will allow optical light to interact with the silicon nitride membrane without additionally interacting with silicon, niobium, or other materials.

3.3.2 Construction of optical cavity

To create a robust, cryogenically compatible Fabry-Perot cavity, we construct a cavity using materials with low thermal expansion, especially Invar [142, 96]. An Invar cavity spacer rigidly holds two high-reflectivity mirrors, one of which is attached to a linear translation piezoelectric element that adjusts the cavity length. The packaged flip-chip slides between the cavity mirrors and is attached to the Invar spacer via Invar plates and a second linear translation piezoelectric element that moves the silicon nitride membrane along the cavity length. Including only two adjustable degrees of freedom allows for construction of a rigid Fabry-Perot cavity that is resistant to environmental vibrations. However, once the components of the cavity are aligned and fixed in place with Stycast 2850FT epoxy, any subsequent misalignment of the silicon nitride membrane relative to the cavity mirrors cannot be corrected [74]. Such misalignment is a common result of cooling to cryogenic temperatures, when differential thermal expansion of cavity components alters their relative positions. Constructing the cavity using materials with low thermal expansion

minimizes the potential for misalignment. With careful construction, a cavity can be cycled from cryogenic temperatures to room temperature multiple times without degredation in performance. A diagram of the cavity is shown in Fig. 3.6a.

The optomechanical coupling $G_o = \partial\omega_o/\partial x$, where ω_o is the resonant frequency of the Fabry-Perot cavity, is predominantly determined by the length of the cavity and the thickness of the silicon nitride membrane [143, 68]. We use a Fabry-Perot cavity ≈ 5 mm long and a membrane ≈ 90 nm thick, which together yield a coupling of $G_o \approx 2\pi \times 40$ MHz/nm.

3.3.3 Initial characterization of frequency converter

As noted in section 3.3, the superconducting microwave circuit can fail when exposed to too much optical frequency light. To test compatibility of the microwave circuit with light confined in the Fabry-Perot cavity, we cool the frequency converter to 4 kelvin using a liquid helium bath cryostat so that the microwave circuit superconducts (niobium superconducts at temperatures below about 9 kelvin). We monitor the response of the microwave circuit with a network analyzer as an increasing amount of 1064 nm light passes through the unmetallized portion of the silicon nitride membrane. From the circuit's response, we determine the energy decay rate of the microwave circuit due to internal loss. Results of this measurement are shown in figure 3.7.

During initial tests we found that the superconducting circuit was inadequately isolated from the light in the optical cavity. Specifically, only a few milliwatts of circulating power in the cavity drastically increased the internal loss rate of the microwave circuit. Internal loss of the microwave circuit only became sufficiently decoupled from the amount of light in the Fabry-Perot cavity when we incorporated an additional niobium shim designed to prevent stray optical light from reaching the microwave circuit. The niobium shim (shown in Fig. 3.5b) did not affect light confined in the Fabry-Perot cavity. These data support previous observations that stoichiometric silicon nitride has low absorption at optical frequencies and the membrane does not experience significant bulk heating when irradiated [135, 74].

Additionally, we characterize the vibrational modes of the silicon nitride membrane. We

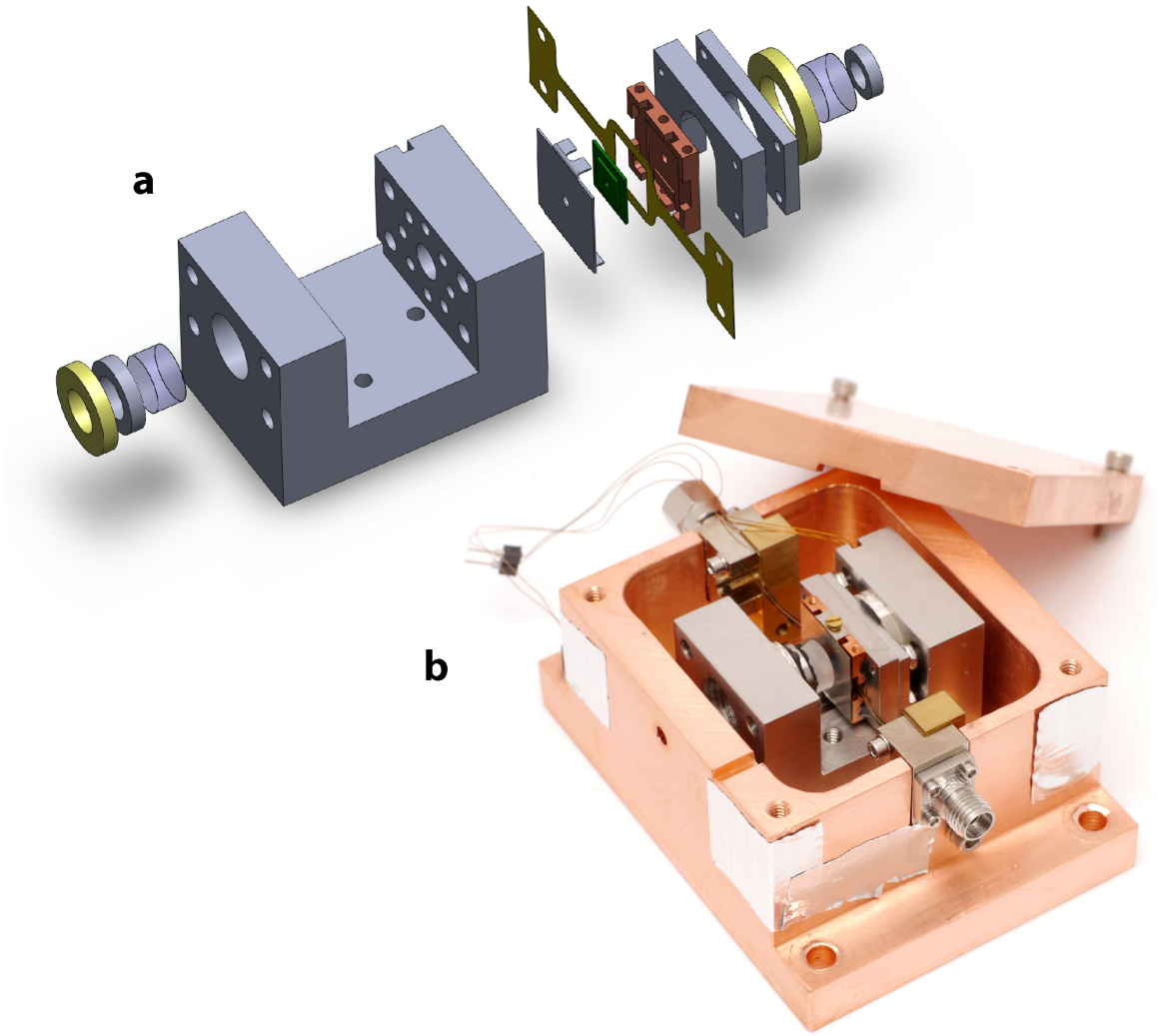

Figure 3.6: Electro-opto-mechanical frequency converter. **a**, Exploded view of a CAD rendering of the converter. Silver corresponds to Invar, yellow to piezoelectric material, and light gray to fused silica (the substrate for the high-reflectivity mirrors). The flip-chip microwave circuit and mounting are also shown. **b**, Picture of completed converter, which during operation is enclosed in a copper box. A coaxial cable carries microwave signals to and from the converter, and a hole in the copper box allows optical signals to enter and exit converter.

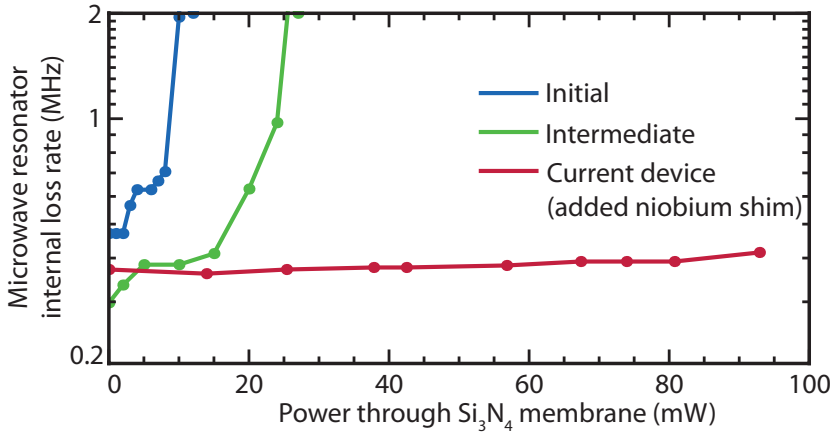

Figure 3.7: Compatibility of microwave circuitry with optical frequency light. Optical power confined in the cavity had dramatically less effect on the microwave circuit when we incorporated a niobium shim that prevented any stray light from reaching the microwave circuit (see Fig. 3.5).

drive the linear translation piezoelectric element connected to the silicon nitride membrane at a frequency ω and simultaneously drive the optical cavity with a monochromatic pump. Motion of the silicon nitride membrane appears as 'sidebands' on the pump as discussed in section 2.3. A peak in sideband power occurs when the signal driving the piezoelectric element has a frequency near $\omega = \omega_{\mathrm{m}}$. With this method, we measure the resonant frequency of several vibrational modes of the silicon nitride membrane. By comparing the measured resonant frequencies with a finite element simulation of the membrane, we identify several vibrational modes suitable for frequency conversion. These modes are shown in Fig. 3.8.

3.3.4 Future improvements

We have constructed a microwave-to-optical frequency converter by simultaneously coupling a silicon nitride membrane to both a superconducting microwave circuit and a high-finesse optical cavity. Our frequency converter provides a potential route to quantum-compatible frequency conversion; however, a few aspects need improvement. The flip-chip microwave circuit does not provide a reproducible acoustic environment for the silicon nitride membrane. The silicon frame that

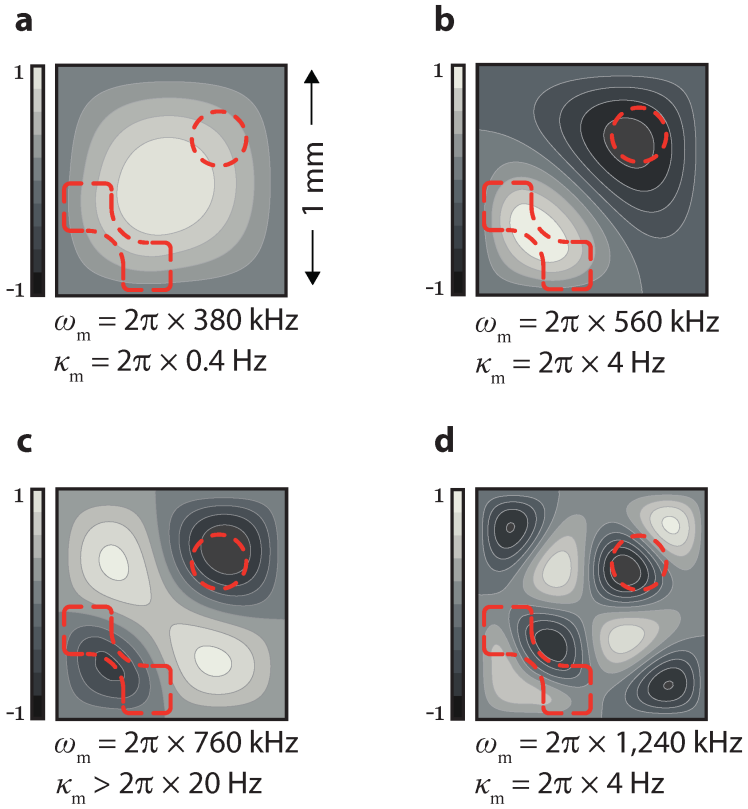

Figure 3.8: Simulated vibrational modes of membrane used in electro-opto-mechanical frequency converter. **a**—**d**, Contour plots of simulated membrane displacement, normalized to unity, for four different vibrational modes of the partially metallized silicon nitride membrane used in the frequency converter. Outline of the niobium metallization is indicated with red bowtie shapes, and the outline of the optical beam waist is indicated with red circles.

supports the membrane can potentially be modified to include a phononic crystal [144] that will acoustically isolate the membrane from the epoxy connections [145, 146]. This modification is likely compatible with a flip-chip microwave circuit, and could result in reproducibly high quality factors for vibrational modes of the silicon nitride membrane. Second, although the open design of the Fabry-Perot cavity makes incorporating the microwave circuit simple, it sacrifices some mechanical rigidity and makes the converter susceptible to failure during cooling to cryogenic temperatures. We think that building a more integrated device, rather than attaching a packaged microwave circuit as shown in Fig. 3.5, will improve converter performance and simultaneously simplify its

assembly.

3.4 Radiation pressure enables frequency conversion

The electro-opto-mechanical converter described in section 3.3 consists of a mechanical oscillator coupled to two electromagnetic resonators. We can model the converter using the mathematical formalism of cavity optomechanics, introduced in section 2.2. In particular, equations 2.28 can be modified to include a second electromagnetic resonator. This results in

$$\begin{aligned}
\dot{a}(t) &= (\imath\Delta_{\mathrm{o}} - \kappa_{\mathrm{o}}/2)a(t) - \imath g_{\mathrm{o}}(c(t) + c^*(t)) + \sqrt{\kappa_{\mathrm{o,ext}}}a_{\mathrm{in}}(t) + \sqrt{\kappa_{\mathrm{o,int}}}a_0(t) \\
\dot{b}(t) &= (\imath\Delta_{\mathrm{e}} - \kappa_{\mathrm{e}}/2)b(t) - \imath g_{\mathrm{e}}(c(t) + c^*(t)) + \sqrt{\kappa_{\mathrm{e,ext}}}b_{\mathrm{in}}(t) + \sqrt{\kappa_{\mathrm{e,int}}}b_0(t) \\
\dot{c}(t) &= (-\imath\omega_{\mathrm{m}} - \kappa_{\mathrm{m}}/2)c(t) - \imath(g_{\mathrm{o}}a^*(t) + g_{\mathrm{o}}^*a(t)) - \imath(g_{\mathrm{e}}b^*(t) + g_{\mathrm{e}}^*b(t)) + \sqrt{\kappa_{\mathrm{m}}}c_{\mathrm{in}}(t),
\end{aligned} \tag{3.1}$$

where the subscript 'e' indicates parameters associated with the electrical circuit and the subscript 'o' to indicate parameters associated with the optical cavity. The field amplitudes $b(t)$ and $a(t)$ are the fluctuations about the microwave and optical pumps, respectively. The pumps populate the microwave circuit and optical cavity with mean field amplitudes $\bar{b}$ and $\bar{a}$, as described in section 2.4. The mean field amplitude controls the strength of the optomechanical coupling: $g_{\mathrm{e}} = G_{\mathrm{e}}x_{\mathrm{zpf}}\bar{b}$ and $g_{\mathrm{o}} = G_{\mathrm{o}}x_{\mathrm{zpf}}\bar{a}$. Fig. 3.9 visually depicts Eqns. 3.1, and table 3.1 contains parameters of the electro-opto-mechanical frequency converter described in section 3.3.

3.4.1 Frequency conversion in the resolved-sideband and weak-coupling regime

The dynamics of frequency conversion can be more easily understood with a few experimentally justified approximations to Eqn. 3.1. First, I'll set the frequency of the microwave and optical pumps so that $\Delta_{\mathrm{e}} = \Delta_{\mathrm{o}} = -\omega_{\mathrm{m}}$ as diagrammed in Fig. 3.10. In the resolved-sideband regime ($4\omega_{\mathrm{m}} \gg \kappa_{\mathrm{e}}, \kappa_{\mathrm{o}}$), these detunings maximally damp the mechanical oscillator via dynamical backaction as discussed in section 2.4. To simplify the dynamics, I'll remove the free evolution of the field amplitudes by moving to a new rotating frame: $a(t) \to a(t)e^{-\imath\omega_{\mathrm{m}}t}$, $b(t) \to b(t)e^{-\imath\omega_{\mathrm{m}}t}$, $c(t) \to c(t)e^{-\imath\omega_{\mathrm{m}}t}$, and so forth for the other field amplitudes. With these adjustments Eqns. 3.1

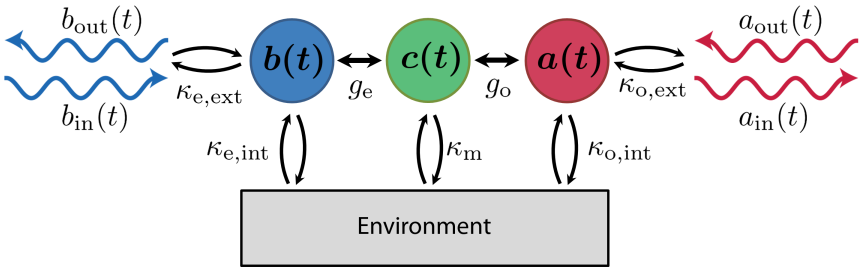

Figure 3.9: Three coupled harmonic oscillators form the frequency converter. The electromagnetic field in the microwave circuit is described by field amplitude $b(t)$, the position of the mechanical oscillator is described by field amplitude $c(t)$, and the electromagnetic field in the optical cavity is described by field amplitude $a(t)$. The microwave circuit can be driven via its coupling to a transmission line and the optical cavity can be driven via a partially transmissive input mirror, as diagrammed in Fig. 3.2. The electromagnetic resonators and the mechanical oscillator are also coupled to the their environment.

Table 3.1: Parameters of electro-opto-mechanical frequency converter. Sets of values apply to three different vibrational modes of the mechanical oscillator we used for frequency conversion.

Parameter	Value	Units
g_{e}	$2\pi\times 80^{*}$	kHz
ω_{e}	$2\pi\times 7.06$	GHz
$\kappa_{\mathrm{e,ext}}$	$2\pi\times 1220$	kHz
$\kappa_{\mathrm{e,int}}$	$2\pi\times 370$	kHz
κ_{e}	$\kappa_{\mathrm{e,ext}}+\kappa_{\mathrm{e,int}}$	
g_{o}	$2\pi\times 80^{\dagger}$	kHz
ω_{o}	$2\pi\times 282$	THz
$\kappa_{\mathrm{o,ext}}$	$2\pi\times 380$	kHz
$\kappa_{\mathrm{o,int}}$	$2\pi\times 1270$	kHz
κ_{o}	$\kappa_{\mathrm{o,ext}}+\kappa_{\mathrm{o,int}}$	
ω_{m}	$2\pi\times\{380,\ 560,\ 1240\}$	kHz
κ_{m}	$2\pi\times\{0.42,\ 4.0,\ 4.2\}$	Hz

*Adjustable up to this value via the microwave pump.

†Adjustable up to this value via the optical pump.

become

$$\begin{aligned}
\dot{a}(t) &= -(\kappa_{\mathrm{o}}/2)a(t) - \imath g_{\mathrm{o}}(c(t) + c^*(t)e^{2\imath\omega_{\mathrm{m}}t}) + \sqrt{\kappa_{\mathrm{o,ext}}}a_{\mathrm{in}}(t) \\
\dot{b}(t) &= -(\kappa_{\mathrm{e}}/2)b(t) - \imath g_{\mathrm{e}}(c(t) + c^*(t)e^{2\imath\omega_{\mathrm{m}}t}) + \sqrt{\kappa_{\mathrm{e,ext}}}b_{\mathrm{in}}(t) \\
\dot{c}(t) &= -(\kappa_{\mathrm{m}}/2)c(t) - \imath(g_{\mathrm{o}}a^*(t)e^{2\imath\omega_{\mathrm{m}}t} + g_{\mathrm{o}}^*a(t)) - \imath(g_{\mathrm{e}}b^*(t)e^{2\imath\omega_{\mathrm{m}}t} + g_{\mathrm{e}}^*b(t)) + \sqrt{\kappa_{\mathrm{m}}}c_{\mathrm{in}}(t).
\end{aligned} \tag{3.2}$$

Eqns. 3.2 can be simplified with a rotating wave approximation that neglects the terms oscillating at frequency $2\omega_{\mathrm{m}}$. For this approximation to be valid, these terms must oscillate faster than other rates in the problem, leading to $4\omega_{\mathrm{m}} \gg \kappa_{\mathrm{o}}, \kappa_{\mathrm{e}}$. This approximation places the model in the resolved-sideband regime. Although the frequency converter we have constructed does not operate deep in the resolved-sideband regime (see Table 3.1), many aspects of frequency conversion in the resolved-sideband regime appear in the unresolved-sideband regime. If the optomechanical coupling rates are much slower than the energy decay rates of the electromagnetic resonators, $\kappa_{\mathrm{o}} \gg g_{\mathrm{o}}$ and $\kappa_{\mathrm{e}} \gg g_{\mathrm{e}}$, then the dynamics of the electromagnetic resonators can be adiabatically eliminated by setting $\dot{a}(t) = \dot{b}(t) = 0$ [147]. In this weak-coupling regime, we have

$$\begin{aligned}
a(t) &= \frac{-2\imath g_{\mathrm{o}}}{\kappa_{\mathrm{o}}}c(t) + \frac{2}{\kappa_{\mathrm{o}}}\sqrt{\kappa_{\mathrm{o,ext}}}a_{\mathrm{in}}(t) \\
b(t) &= \frac{-2\imath g_{\mathrm{e}}}{\kappa_{\mathrm{e}}}c(t) + \frac{2}{\kappa_{\mathrm{e}}}\sqrt{\kappa_{\mathrm{e,ext}}}b_{\mathrm{in}}(t) \\
\dot{c}(t) &= -\frac{1}{2}\left(\kappa_{\mathrm{m}} + \frac{4|g_{\mathrm{o}}|^2}{\kappa_{\mathrm{o}}} + \frac{4|g_{\mathrm{e}}|^2}{\kappa_{\mathrm{e}}}\right)c(t) - \frac{2\imath g_{\mathrm{o}}^*}{\sqrt{\kappa_{\mathrm{o}}}}\frac{\sqrt{\kappa_{\mathrm{o,ext}}}}{\sqrt{\kappa_{\mathrm{o}}}}a_{\mathrm{in}}(t) - \frac{2\imath g_{\mathrm{e}}^*}{\sqrt{\kappa_{\mathrm{e}}}}\frac{\sqrt{\kappa_{\mathrm{e,ext}}}}{\sqrt{\kappa_{\mathrm{e}}}}b_{\mathrm{in}}(t)
\end{aligned} \tag{3.3}$$

Eqns. 3.3 are simply solved in the frequency domain. Using the input-output relation $a_{\mathrm{out}}(\omega) = \sqrt{\kappa_{\mathrm{o,ext}}}a(\omega) - a_{\mathrm{in}}(\omega)$ with $a_{\mathrm{in}}(\omega) = 0$, we can find an expression for upconversion.

$$S_{21}(\omega) = \frac{a_{\mathrm{out}}(\omega)}{b_{\mathrm{in}}(\omega)} = e^{\imath\phi} \times \frac{\sqrt{\Gamma_{\mathrm{o}}\Gamma_{\mathrm{e}}}}{-\imath(\omega - \omega_{\mathrm{m}}) + (\Gamma_{\mathrm{o}} + \Gamma_{\mathrm{e}} + \kappa_{\mathrm{m}})/2} \times \sqrt{\eta_{\mathrm{o}}\eta_{\mathrm{e}}} \tag{3.4}$$

where $\phi = \mathrm{Arg}(-g_{\mathrm{o}}g_{\mathrm{e}}^*)$, $\Gamma_{\mathrm{o}} = 4|g_{\mathrm{o}}|^2/\kappa_{\mathrm{o}}$ and $\Gamma_{\mathrm{e}} = 4|g_{\mathrm{e}}|^2/\kappa_{\mathrm{e}}$, and $\eta_{\mathrm{e}} = \kappa_{\mathrm{e,ext}}/\kappa_{\mathrm{e}}$ and $\eta_{\mathrm{o}} = \kappa_{\mathrm{o,ext}}/\kappa_{\mathrm{o}}$.[1]

Γ_{e} and Γ_{o} are exactly the additional mechanical damping rates predicted in section 2.26 with $\Delta = -\omega_{\mathrm{m}}$ and $4\omega_{\mathrm{m}} \gg \kappa$. Eqn. 3.4 is in the frame of the pumps so that $b_{\mathrm{in}}(\omega)$ and $a_{\mathrm{out}}(\omega)$ are a

[1] The optical cavity additionally emits light into a particular spatial mode. If this mode does not perfectly match the spatial mode of the incident light field, $\eta_{\mathrm{o}} = \epsilon\kappa_{\mathrm{o,ext}}/\kappa_{\mathrm{o}}$ where ϵ is the optical mode matching.

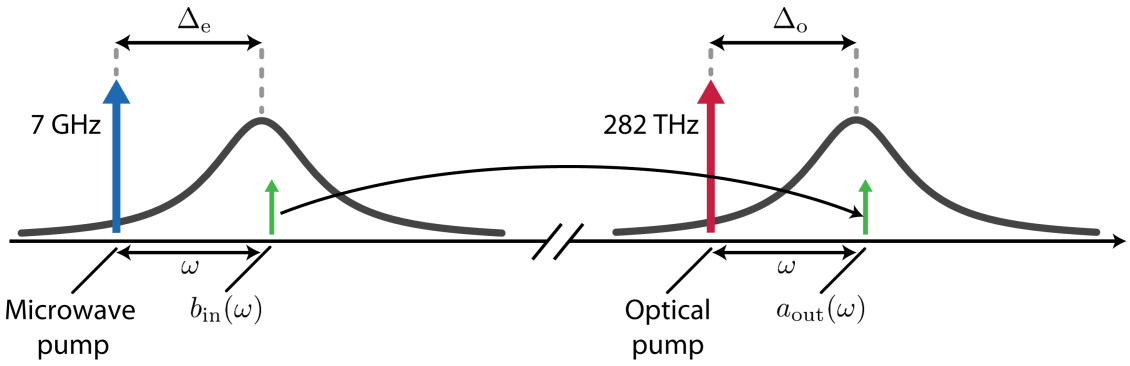

Figure 3.10: Frequency domain schematic of frequency conversion. A strong microwave pump (blue arrow) is applied below the microwave resonance (response shown as black curve) with detuning Δ_e. Similarly, a strong optical pump (red arrow) is applied below the optical resonance (response shown as a black curve) with detuning Δ_o. This enables an incoming microwave frequency signal $b_{in}(\omega)$ to be upconverted to an outgoing optical frequency signal $a_{out}(\omega)$. The expression for frequency upconversion (or downconversion) in the weak-coupling ($\kappa_o \gg g_o$ and $\kappa_e \gg g_e$) and resolved-sideband ($4\omega_m \gg \kappa_e, \kappa_o$) regimes with $\Delta_e = \Delta_o = -\omega_m$ is given in equation 3.4

frequency ω above the microwave and optical pumps, respectively. In this analysis, upconversion is mathematically identical to downconversion, $S_{21}(\omega) = S_{12}(\omega)$, meaning that frequency conversion is bidirectional. A frequency domain schematic of frequency conversion is shown in Fig. 3.10.

Using Eqns. 3.3 with $b_{out}(\omega) = \sqrt{\kappa_{e,ext}}b(\omega) - b_{in}(\omega)$, we can find an expression for the reflected microwave signal.

$$S_{11}(\omega) = \frac{b_{out}(\omega)}{b_{in}(\omega)} = \frac{-\Gamma_e \eta_e}{-\imath(\omega - \omega_m) + (\Gamma_e + \Gamma_o + \kappa_m)/2} + 2\eta_e - 1. \tag{3.5}$$

The scattering parameters $S_{11}(\omega)$ and $S_{21}(\omega)$ $(= S_{12}(\omega))$ are shown in Fig. 3.11 for matched $(\Gamma_e = \Gamma_o)$ optomechanical coupling rates.

Photon number conversion efficiency $|S_{21}(\omega)|^2$ is greatest when the signal is a mechanical resonant frequency above the microwave and optical pumps ($\omega = \omega_m$). Additionally, the rates Γ_e and Γ_o must be matched to each other to maximize conversion efficiency. This 'cooperativity matching' [60, 130] can be accomplished by adjusting the strength of the microwave or optical pump. Unit conversion efficiency is only reached when the microwave circuit, optical cavity, and mechanical resonator have negligible loss: $\eta_e = \eta_o \approx 1$ and $\Gamma_o, \Gamma_e \gg \kappa_m$. When unit transfer

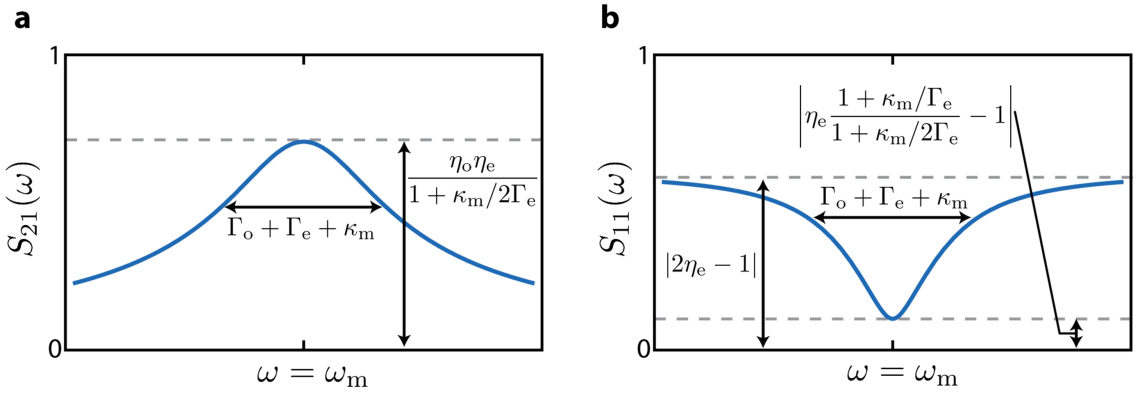

Figure 3.11: **a**, Expected scatterering parameters for electro-opto-mechanical frequency conversion with matched damping rates ($\Gamma_e = \Gamma_o$). **a**, Frequency conversion occurs over a bandwidth $\Gamma_o + \Gamma_e + \kappa_m$ and with unit photon number efficiency when $\eta_o = \eta_e = 1$ and $\Gamma_0, \Gamma_e \gg \kappa_m$. **b**, Reflected microwave power diminishes as transfer efficiency increases.

efficiency is reached, there is no reflected microwave power, as can be seen in Fig. 3.11. This indicates nearly ideal conversion, as the entire microwave signal is transformed into an optical signal. However, the converter is only active over a limited bandwidth set by the total damping of the mechanical oscillator, $\Gamma_o + \Gamma_e + \kappa_m$. This bandwidth can be increased by using stronger microwave and optical pumps; however, eventually it is limited by the bandwidths of the microwave circuit and optical cavity.

3.4.2 Frequency conversion in the weak-coupling regime

A full calculation of the transfer function using equations 3.1 without any additional simplifying assumptions can be performed using the methods presented in section 2.5.1 [148]. If we assume the weak coupling regime, a valid approximation given parameters of our frequency converter (see table 3.1), we can write down a relatively succinct expression for $S_{21}(\omega)$.

$$S_{21}(\omega) = \frac{a_{\text{out}}(\omega)}{b_{\text{in}}(\omega)} = e^{\imath\phi} \times \frac{\sqrt{\Gamma_o\Gamma_e}}{-\imath(\omega - \omega'_m) + (\Gamma_o + \Gamma_e + \kappa_m)/2} \times \sqrt{\mathcal{A}\eta_o\eta_e}, \tag{3.6}$$

where $\omega'_m = \omega_m + \Omega_e + \Omega_o$ is the radiation pressure-modified mechanical resonant frequency and $\mathcal{A} = \mathcal{A}_e\mathcal{A}_o$ is conversion gain. Frequency shifts Ω_e and Ω_o, and coupling rates Γ_o and Γ_e, are

determined by the dynamical backaction of the electromagnetic fields as given in equation 2.26.

$$\begin{aligned}\Omega_{\mathrm{e}} &= g_{\mathrm{e}}^2\left[\frac{\Delta_{\mathrm{e}}+\omega_{\mathrm{m}}}{(\Delta_{\mathrm{e}}+\omega_{\mathrm{m}})^2+(\kappa_{\mathrm{e}}/2)^2}+\frac{\Delta_{\mathrm{e}}-\omega_{\mathrm{m}}}{(\Delta_{\mathrm{e}}-\omega_{\mathrm{m}})^2+(\kappa_{\mathrm{e}}/2)^2}\right]\\ \Omega_{\mathrm{o}} &= g_{\mathrm{o}}^2\left[\frac{\Delta_{\mathrm{o}}+\omega_{\mathrm{m}}}{(\Delta_{\mathrm{o}}+\omega_{\mathrm{m}})^2+(\kappa_{\mathrm{o}}/2)^2}+\frac{\Delta_{\mathrm{o}}-\omega_{\mathrm{m}}}{(\Delta_{\mathrm{o}}-\omega_{\mathrm{m}})^2+(\kappa_{\mathrm{o}}/2)^2}\right]\end{aligned} \tag{3.7}$$

$$\begin{aligned}\Gamma_{\mathrm{e}} &= g_{\mathrm{e}}^2\left[\frac{\kappa_{\mathrm{e}}}{(\Delta_{\mathrm{e}}+\omega_{\mathrm{m}})^2+(\kappa_{\mathrm{e}}/2)^2}-\frac{\kappa_{\mathrm{e}}}{(\Delta_{\mathrm{e}}-\omega_{\mathrm{m}})^2+(\kappa_{\mathrm{e}}/2)^2}\right]\\ \Gamma_{\mathrm{o}} &= g_{\mathrm{o}}^2\left[\frac{\kappa_{\mathrm{o}}}{(\Delta_{\mathrm{o}}+\omega_{\mathrm{m}})^2+(\kappa_{\mathrm{o}}/2)^2}-\frac{\kappa_{\mathrm{o}}}{(\Delta_{\mathrm{o}}-\omega_{\mathrm{m}})^2+(\kappa_{\mathrm{o}}/2)^2}\right].\end{aligned} \tag{3.8}$$

Additionally, the gains are given by

$$\begin{aligned}\mathcal{A}_{\mathrm{e}} &= \frac{(\Delta_{\mathrm{e}}-\omega_{\mathrm{m}})^2+(\kappa_{\mathrm{e}}/2)^2}{-4\Delta_{\mathrm{e}}\omega_{\mathrm{m}}}\\ \mathcal{A}_{\mathrm{o}} &= \frac{(\Delta_{\mathrm{o}}-\omega_{\mathrm{m}})^2+(\kappa_{\mathrm{o}}/2)^2}{-4\Delta_{\mathrm{o}}\omega_{\mathrm{m}}}.\end{aligned} \tag{3.9}$$

Although there is a small shift in the center frequency of the conversion window of Eqn. 3.6 relative to Eqn. 3.4, the most important difference is that frequency conversion in the unresolved-sideband regime has photon number gain as indicated by the factor $\mathcal{A}$. Gain becomes appreciable when $4\omega_{\mathrm{m}} < \kappa_{\mathrm{o}}, \kappa_{\mathrm{e}}$ or when pump detunings are small and $\omega_{\mathrm{m}} > 4\Delta_{\mathrm{o}}, 4\Delta_{\mathrm{e}}$. From an experimental point of view, gain occurs when a converted signal appears at a frequency ω both above and below the microwave or optical pump, as diagrammed in Fig. 3.12. The gains $\mathcal{A}_{\mathrm{e}}$ and $\mathcal{A}_{\mathrm{o}}$ in Eqns. 3.9 can be formulated as a ratio of power in the upper sideband at frequency ω above the pump, and power in the lower sideband at frequency ω below the pump.

As introduced in section 2.3, if a mechanical oscillator in a cavity optomechanical system vibrates with a fixed amplitude at frequency ω_{m}, it scatters energy from the pump into frequencies ω_{m} above and below the pump. The amount of power scattered is given in Eqns. 2.16 and 2.17 for a generic electromagnetic resonator with linewidth κ and pump detuning Δ. If we identify the resonator as the optical cavity of the electro-opto-mechanical frequency converter, then

$$\mathcal{A}_{\mathrm{o}} = \frac{P_{\mathrm{usb}}}{P_{\mathrm{usb}} - P_{\mathrm{lsb}}} \tag{3.10}$$

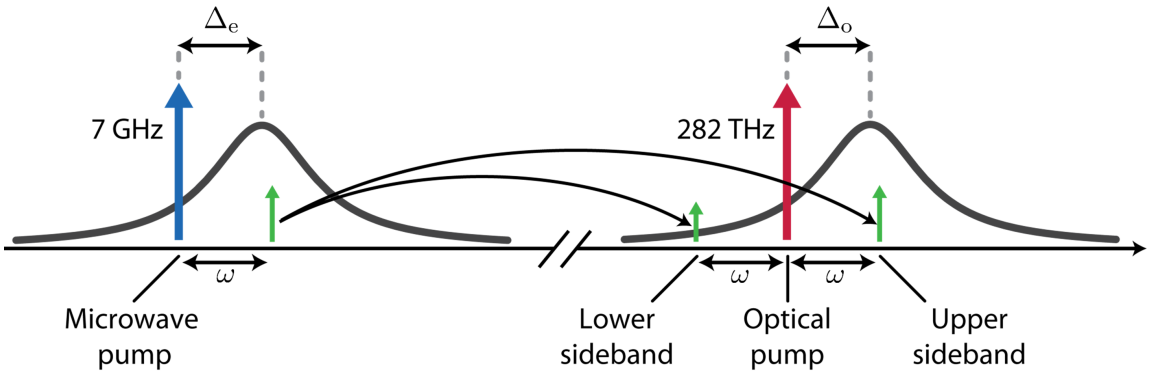

Figure 3.12: Frequency domain schematic of frequency conversion with gain. A strong microwave pump (blue arrow) is applied below the microwave resonance (response shown as black curve) with detuning Δ_e. Similarly, a strong optical pump (red arrow) is applied below the optical resonance (responce shown as a black curve) with detuning Δ_o. This enables an incoming microwave frequency signal $b_{in}(\omega)$ to be upconverted to an outgoing optical frequency signal at $\omega_o + \omega$. Conversion also produces a lower frequency signal at $\omega_o - \omega$ when the optical resonator response does not completely suppress it, i.e., when $\omega_m \lesssim \kappa_o$. This additional sideband indicates the conversion has gain, as seen in Eqn. 3.6.

and similarly for the microwave circuit. Gain $\mathcal{A}$ is only unity when there is no power present in the lower sideband, and suppressing the lower sideband requires the resolved sideband regime $4\omega_m \gg \kappa_e, \kappa_o$. The minimum expected conversion gain $\mathcal{A}$ as a function of the resolved-sideband parameter ω_m/κ_e is shown in Fig. 3.13 for $\kappa_e = \kappa_o$.

In section 3.6.1, we demonstrate frequency conversion using three different vibrational modes of the silicon nitride membrane. One vibrational mode with $\omega_m = 1240$ kHz approaches the resolved-sideband regime with $\mathcal{A} < 2$. We use the other two vibrational modes to explore the minimum bound on conversion gain.

3.4.3 Noise added during frequency conversion

Phase-insensitive gain during frequency conversion means that noise must be added to the signal during conversion [127]. This noise manifests as extraneous vibrations of the mechanical oscillator. We quantify the vibrational noise added to a signal during upconversion by calculating the spectral density of the output optical field with no input fields, $\langle [a_{out}(\omega)]^\dagger a_{out}(\omega) \rangle$ with $a_{in}(\omega) =$

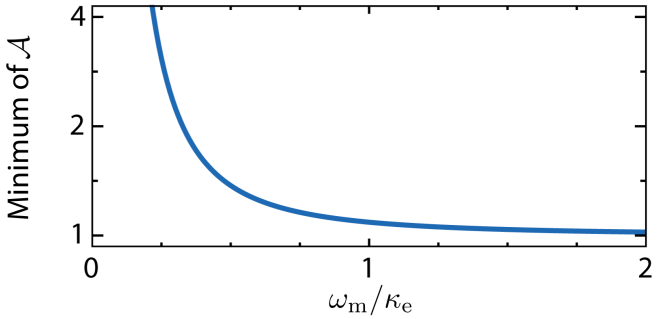

Figure 3.13: Minimum gain during frequency conversion, assuming $\kappa_e = \kappa_o$. In the resolved sideband limit of $4\omega_m \gg \kappa_e, \kappa_o$, the minimum gain approaches unity.

$b_{in}(\omega) = 0$, and referring it to the input of the converter [60]. In units of quanta of added noise (a quantum corresponding to one photon per second in a 1 Hz bandwidth [93]), upconversion adds

$$n_{vib} = \frac{\left\langle [a_{out}(\omega)]^\dagger a_{out}(\omega) \right\rangle}{|S_{21}(\omega)|^2} = \frac{1}{\mathcal{A}_e \eta_e} \left(\frac{\kappa_m n_{env}}{\Gamma_e} + (\mathcal{A}_e - 1) + (\mathcal{A}_o - 1) \right) \tag{3.11}$$

for matched coupling rates, where $n_{env} \equiv 1/(e^{\hbar\omega_m/k_B T_{env}} - 1)$ and T_{env} is the temperature of the mechanical oscillator's environment. Any conversion gain adds noise given by the last two terms in Eqn. 3.11. Environment-driven vibrations of the mechanical oscillator, indicated by the mechanical decoherence rate $\kappa_m n_{env}$, also add noise. Only with unit gain ($\eta_e \gg \mathcal{A}_e - 1$ and $\eta_e \gg \mathcal{A}_o - 1$) and negligible mechanical decoherence ($\eta_e \Gamma_e \gg \kappa_m n_{env}$) do vibrations of the mechanical oscillator 'freeze out'.

Frequency conversion with low gain and low vibrational noise is closely related to resolved-sideband cooling of a mechanical oscillator. A gain of $\mathcal{A} < 2$ implies that the oscillator can, in principle, be cooled to its ground state of motion using radiation pressure [23, 33, 34]. Low noise frequency conversion can only occur when the mechanical oscillator is simultaneously cooled to near its ground state of motion by both the microwave circuit and the optical cavity. In addition to low vibrational noise, noiseless frequency conversion requires unit conversion efficiency ($\eta_e = \eta_o = 1$).

3.5 Measurement network

In order to measure the scattering parameters of the electro-opto-mechanical frequency converter, we must integrate it into a larger measurement network. To properly predict converter performance, we must specify which components are part of the converter, and which are part of the measurement network. For the calculations in sections 3.4, the converter includes the microwave circuit, the mechanical oscillator, and the optical cavity. Converter performance thus includes internal losses in the microwave, optical, and mechanical resonators and imperfect optical mode matching, but excludes losses and gains in other components that are used in our measurement. This is a natural definition for the converter, and one that makes it a stand-alone component that can be readily integrated into other networks.

A microwave signal generator and a Nd:YAG laser are used to pump the microwave circuit and Fabry-Perot cavity, respectively. To generate a coherent signal at a frequency $\omega \approx \omega_{\mathrm{m}}$ above the pumps, we generate a signal at $\omega \approx \omega_{\mathrm{m}}$ and use it to modulate the microwave or optical pump via single-sideband modulation (accomplished with standard microwave and optical components [148]). After interacting with the converter, the outgoing signals are detected using homodyne detection (for microwave frequencies) and direct detection with a photodiode (for optical frequencies). The detected signal is referenced to the initial signal to obtain a magnitude and phase shift. A diagram of the measurement network is shown in Fig. 3.14, and a detailed diagram is included in appendix C.

Components in the measurement network add additional gains and losses to a measured S-parameter, as diagrammed in Fig. 3.14b, and this makes it difficult to independently and accurately calibrate the quantities $S_{21}(\omega)$ and $S_{12}(\omega)$. However, we can exploit the symmetry of the network to calibrate the product $S_{12}(\omega)S_{21}(\omega)$: To isolate the converter performance from the gains and losses of other components used in our measurement, we measure the forward and reverse transmission, $\alpha S_{21}\delta$ and $\gamma S_{12}\beta$, and the off-resonant reflections, $\alpha\beta$ and $\gamma\delta$. This gives $S_{21}S_{12} = (\alpha S_{21}\delta)(\gamma S_{12}\beta)/(\alpha\beta)(\gamma\delta)$, a quantity insensitive to imperfect measurement of the separate gains and losses α, β, γ, δ. The off-resonant reflections are measured by tuning the injected

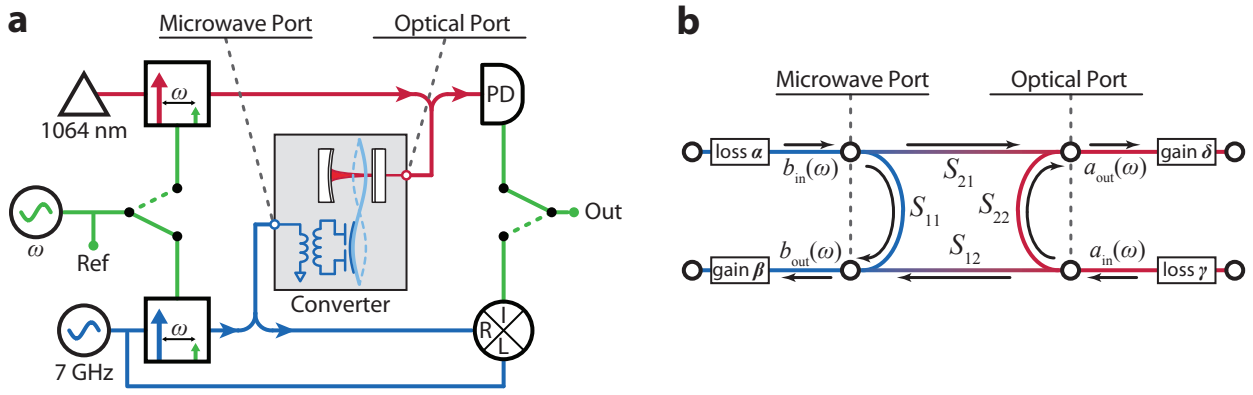

Figure 3.14: Measurement network. **a**, A signal at frequency $\omega \approx \omega_m$ modulates a microwave or optical pump. After interacting with the converter, the output signal is referenced to the initial signal (Ref) to obtain a magnitude and phase shift. **b**, Schematic of the measurement network. To make a calibrated measurement of the S-parameters of the converter, we must remove the additional gains and losses added by the measurement network. This can be done by exploiting the symmetry of the network.

signal away from the resonator's central frequency, where the converter acts as a near-perfect mirror. With this method, we can determine $S_{21}(\omega)S_{12}(\omega)$ to about 6% [148]. We find this calibration procedure appealing because it makes equivalent use of both the forward and reverse transmission of the converter, demonstrating and emphasizing its bidirectional nature.

3.6 Microwave to optical frequency conversion of electromagnetic signals

3.6.1 Bidirectional frequency conversion

By injecting a microwave or optical field and monitoring the outgoing fields, we measure the scattering parameters that give the number efficiency of the converter. Initially, we use the $\omega_m = 2\pi \times 560$ kHz vibrational mode, shown in Fig. 3.15d, for frequency conversion. By sweeping the frequency of the injected microwave signal near $\omega \approx \omega_m$, we confirm that forward transmission $S_{21}(\omega)$ has the expected Lorentzian lineshape of Eqn. 3.6, with a peak at $\omega = \omega_m'$. Reverse transmission $S_{12}(\omega)$ is the same to within our measurement error, giving initial indication that the conversion process is bidirectional. We also monitor microwave reflection $S_{11}(\omega)$ during up-

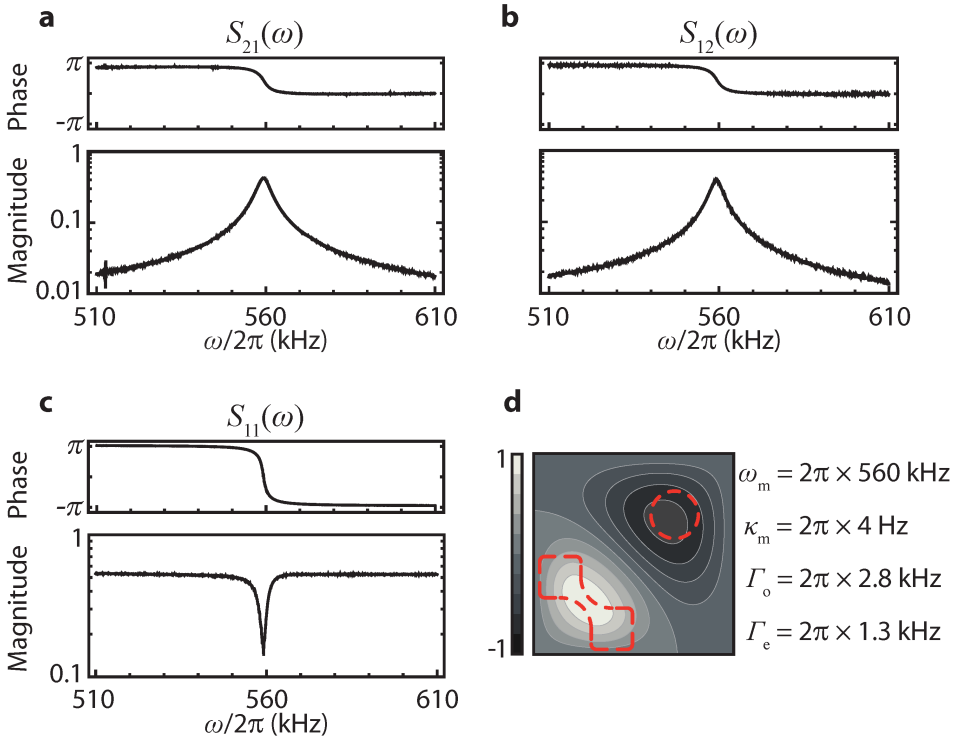

Figure 3.15: Measured scattering parameters. **a** – **c**, Upconversion $S_{21}(\omega)$, downconversion $S_{12}(\omega)$, and microwave reflection $S_{11}(\omega)$ for the $\omega_m = 2\pi \times 560$ kHz vibrational mode with $\Gamma_e = 2\pi \times 1.2$ kHz and $\Gamma_o = 2\pi \times 2.8$ kHz. **d**, Contour plot of membrane displacement, normalized to unity, for the $\omega_m = 2\pi \times 560$ kHz vibrational mode. The outlines of the niobium metallization (red bowtie shape) and optical beam waist (red circle) are included.

conversion. When conversion efficiency peaks at $\omega = \omega_m'$, there is a corresponding dip in reflected microwave power, as seen in Fig. 3.15c, further demonstrating that some of the injected microwave signal is indeed being converted. In addition to the magnitudes of the converted and reflected signal, the measurements also yield phase information. We find that, up to a frequency-dependent phase shift, the phase is preserved during conversion, indicating the conversion between the two frequency regimes is coherent.

Frequency conversion in Fig. 3.15 is performed with specific microwave and optical pump powers that yield optomechanical damping rates of $\Gamma_e = 2\pi \times 1.2$ kHz and $\Gamma_o = 2\pi \times 2.8$ kHz. However, as indicated by Eqn. 3.6, the maximum conversion efficiency is expected to occur near $\Gamma_e = \Gamma_o$. By changing the microwave pump power while holding the optical pump power fixed, we

vary the ratio Γ_e/Γ_o and observe that maximum conversion efficiency occurs near $\Gamma_e = \Gamma_o$, as seen in Fig. 3.16b, confirming the cooperativity matching condition predicted by Eqn. 3.6.

To observe the presence of conversion gain, we perform frequency conversion using different vibrational modes of the silicon nitride membrane. For the $\omega_m = 2\pi \times 380$ kHz vibrational mode, $\omega_m/\kappa_e \approx \omega_m/\kappa_o \approx 0.25$ and a photon number gain of $\mathcal{A} = 3$ is expected as indicated in Fig. 3.13. This results in an apparent efficiency of 0.25, as seen in the peak value of $|S_{21}S_{12}|$ for this vibrational mode (Fig. 3.16c). For conversion with the higher frequency $\omega_m = 2\pi \times 1.24$ MHz vibrational mode, $\omega_m/\kappa_e \approx \omega_m/\kappa_o \approx 0.8$ and the converter approaches the resolved-sideband limit. This reduces the photon number gain to $\mathcal{A} = 1.4$. With this lower gain comes a lower apparent efficiency, but the absorption of microwave power occurs nearer the peak in conversion efficiency, as shown in Fig. 3.16a, indicating more ideal conversion.

The converter reaches nearly unit internal efficiency as $\Gamma_e, \Gamma_o \gg \kappa_m$. For the $\omega_m = 2\pi \times 560$ kHz vibrational mode, the converter reaches a matched ($\Gamma_e = \Gamma_o$) bandwidth of approximately 30 kHz, overwhelming the intrinsic mechanical decay rate of $\kappa_m = 2\pi \times 4$ Hz by nearly four orders of magnitude. For this vibrational mode, we expect the maximum *apparent* conversion efficiency to be $|S_{21}S_{12}| = \mathcal{A}\eta_e\eta_o = 0.169 \pm 0.012$, which corresponds well with the measured maximum of 0.178 ± 0.011. The true efficiency $\eta_e\eta_o$, which does not include conversion gain $\mathcal{A}$, is limited by absorption and scattering of light in the electromagnetic resonators ($\kappa_{e,ext}/\kappa_e = 0.76$ and $\kappa_{o,ext}/\kappa_o = 0.23$), and imperfect optical mode-matching ($\epsilon = 0.47$). These factors combine to give an expected efficiency $\eta_e\eta_o = 0.082 \pm 0.006$. This corresponds well with the measured maximum apparent efficiency divided by the expected gain of 0.086 ± 0.007.

3.6.2 Bandwidth of frequency conversion

The converter achieves a maximum conversion bandwidth of $\Gamma_e + \Gamma_o = 2\pi \times 32$ kHz, as shown in Fig. 3.17. Beyond these damping rates, microwave pump power begins to break superconductivity in the microwave circuit. Although this places a limit on the bandwidth of frequency conversion with a single vibrational mode of the mechanical oscillator, other vibrational modes of the mechanical

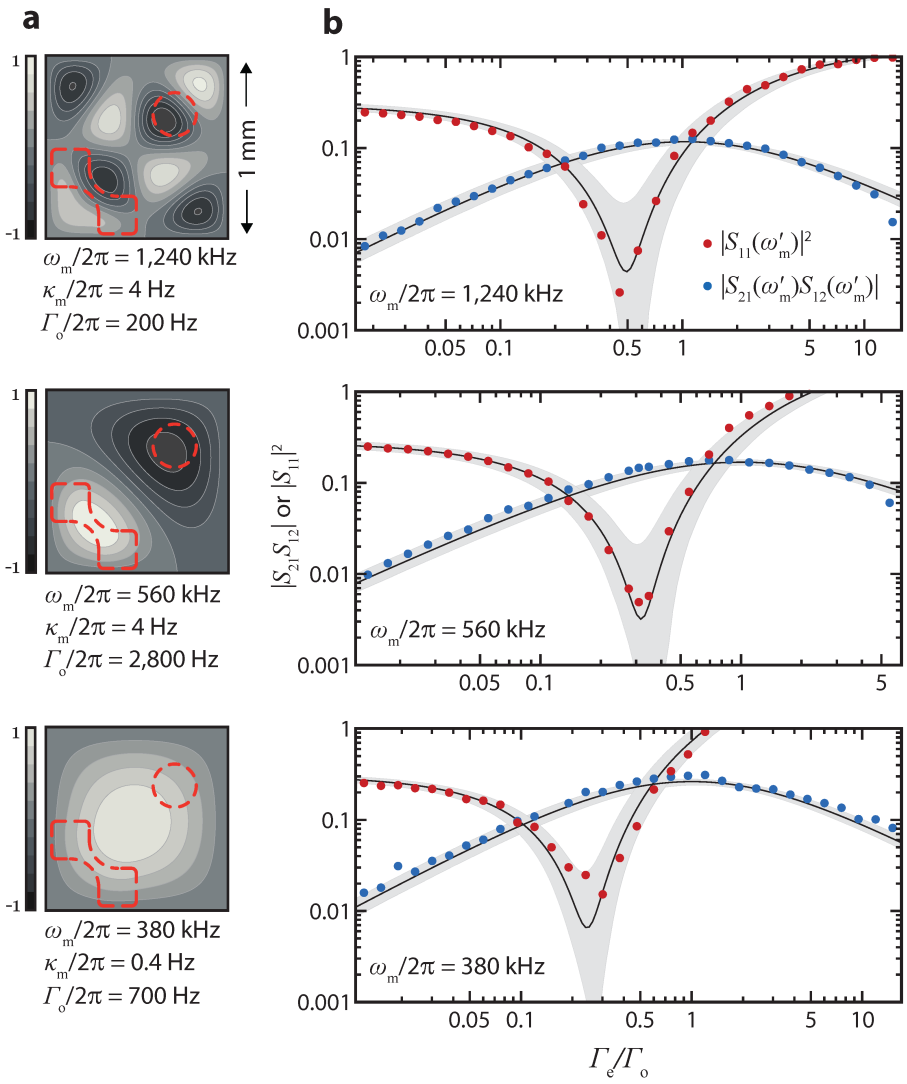

Figure 3.16: Bidirectional and efficient conversion. (**a**) Contour plot of simulated membrane displacement, normalized to unity, for the three vibrational modes used for frequency conversion. Outlines of the optical mode (dashed circle) and niobium metallization (dashed bowtie) are shown. (**b**) Maximum apparent transfer efficiency, $|S_{21}(\omega_m')S_{21}(\omega_m')|$, and microwave reflection coefficient, $|S_{11}(\omega_m')|^2$, as a function of damping ratio for the three vibrational modes. Measurement error is smaller than the plotted points. The black lines are expected values given independently measured system parameters. Gray regions express the uncertainties of our system parameters, which are approximately 10% [148]. Pumps are red-detuned with $\Delta_e \approx -\omega_m$ and $\Delta_o/2\pi = -730$ kHz.

oscillator also contribute to frequency conversion, as can be seen in Fig. 3.17b. This suggests the possibility of improving conversion bandwidth by using multiple vibrational modes of the silicon nitride membrane for frequency conversion.

3.6.3 Noise added during frequency conversion

Noise added during frequency conversion will appear in the spectral density of the output optical or microwave fields. We can specify the noise added to a signal during conversion with a signal to noise ratio (SNR) defined as SNR=$\mathcal{S}_{\mathrm{in}}/n_{\mathrm{vib}}$ where $\mathcal{S}_{\mathrm{in}}$ is the spectral density of the input signal and n_{vib} is the vibrational noise added during conversion as given by Eqn. 3.11. To characterize noise added by vibrations of the mechanical oscillator, we inject a monochromatic microwave field into the microwave port of the converter and measure the spectral density of the output optical field. We measure vibrational noise added during upconversion (as opposed to downconversion) because near quantum-limited photodetection allows us to quickly characterize noise at optical frequencies. The microwave field is injected at a frequency ω_{m}' above the microwave pump with matched coupling rates ($\Gamma_{\mathrm{e}} \approx \Gamma_{\mathrm{o}}$). As shown in the inset of Fig. 3.18, the converted signal power appears on a noise background that is dominated by thermal fluctuations filtered by the mechanical oscillator's susceptibility. As we increase the coupling rates Γ_{e} and Γ_{o} (while keeping the injected microwave signal power constant), we observe an increased SNR (Fig. 3.18). Fitting the observed SNR with n_{vib} as given by Eqn. 3.11 allows us to estimate the added vibrational noise.

Vibrational noise is non-zero during 4 K operation because the mechanical resonator is still 'hot' and driven by thermal fluctuations. While this effect can be substantially reduced by increasing Γ_{e} and Γ_{o}, colder temperatures are needed to reduce added vibrational noise to the single quantum level. Thermalizing the vibrational modes of the mechanical resonator to a dilution refrigerator temperature of 40 mK with the achieved $\Gamma_{\mathrm{e}} = \Gamma_{\mathrm{o}} = 2\pi \times 15$ kHz would ideally result in $n_{\mathrm{vib}} \approx 1$. We view colder temperatures as a necessity for quantum frequency conversion since temperatures of $T_{\mathrm{env}} < (2\pi \times 7\ \mathrm{GHz})\hbar/k_{\mathrm{B}} \approx 300$ mK are required to eliminate Johnson noise at microwave frequencies that corrupts weak (quantum) signals.

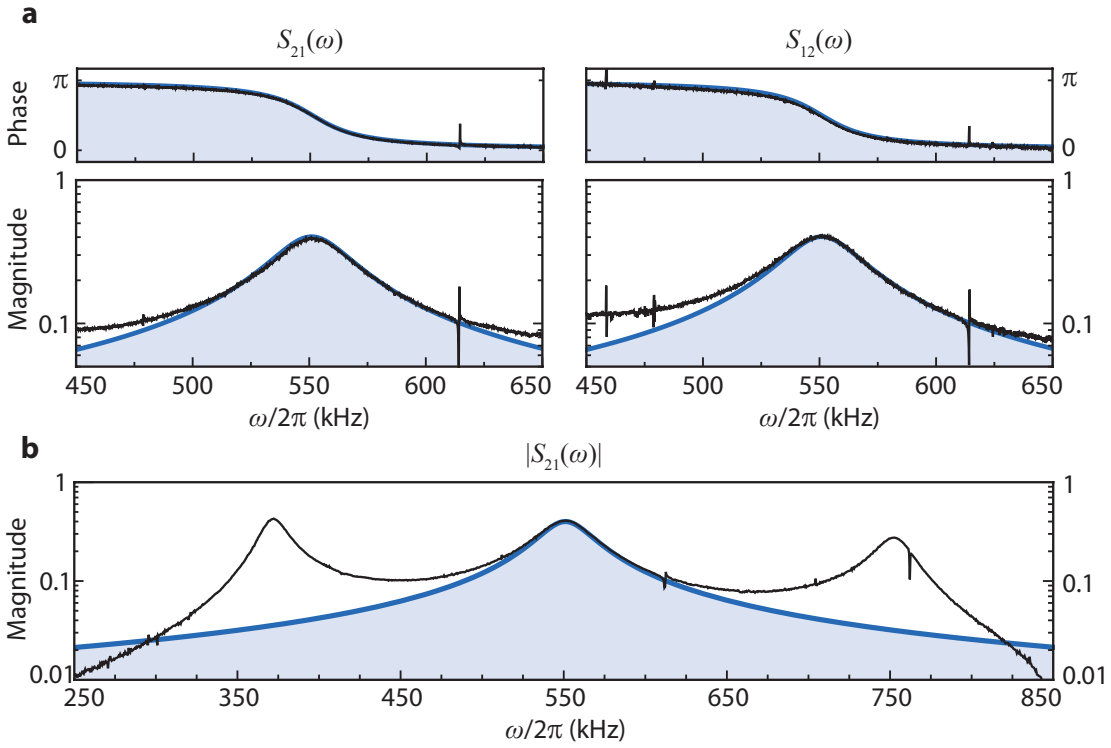

Figure 3.17: (**a**) Forward transmission $S_{21}(\omega)$ and reverse transmission $S_{12}(\omega)$ for the $\omega_{\mathrm{m}} = 2\pi \times 560$ kHz vibrational mode with 32 kHz of transfer bandwidth. A Lorentzian fit (blue) is included. (**b**) Upconversion over a wide range of frequencies; conversion is visible for three vibrational modes of the mechanical oscillator at $\omega_{\mathrm{m}}/2\pi = 380$ kHz, 560 kHz, and 760 kHz.

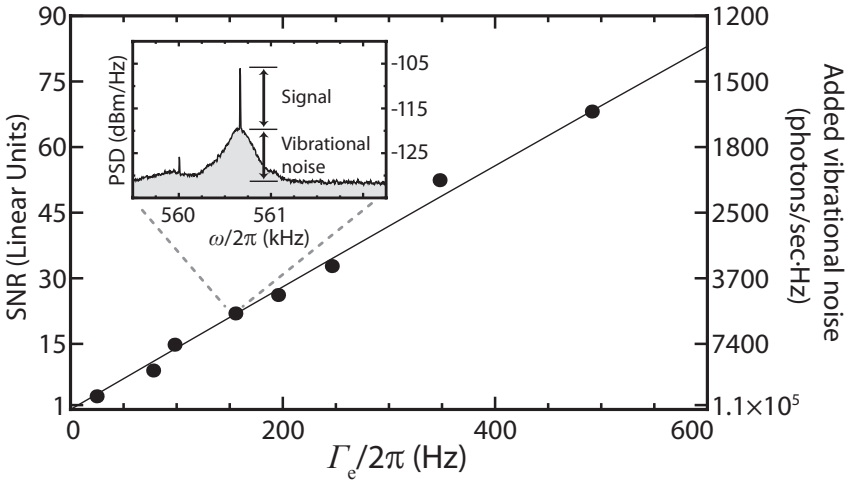

Figure 3.18: Signal to noise ratio (SNR). SNR for an upconverted microwave signal as a function of coupling rate Γ_e; injected signal power is kept constant and $\Gamma_o \approx \Gamma_e$. A fit with n_{vib} as given by Eqn. 3.11 is shown (line), and the extracted added vibrational noise (n_{vib}) is shown on the right vertical axis. Inset: power spectral density (PSD) of an upconverted microwave signal.

3.7 Future work

We have demonstrated a converter that provides a bidirectional, efficient, and impedance-matched link between microwave and optical frequencies. Additionally, the bidirectionality of the conversion, its phase-preserving nature, and the absorption of injected signal power during conversion provide firm evidence that state transfer is occurring, and that we have accessed the beam-splitter Hamiltonian [147] that is fundamentally capable of quantum frequency conversion. The ability to efficiently and coherently exchange information between microwave and optical light opens new possibilities for quantum information, in particular entanglement between microwave and optical photons [132, 149, 150, 151].

Although the converter functions well, some modest changes can significantly improve performance. Removing internal loss in the electromagnetic resonators will improve η_e and η_o, which currently limit conversion efficiency. Lower temperatures will improve the microwave resonator, which at 4 K suffers from thermally excited quasiparticles that limit η_e. More careful placement of the flip-chip circuit inside the optical cavity can decrease scattered light and improve optical mode matching [86]. Added vibrational noise can be reduced by using mechanical oscillators with

higher quality factors. In particular, the type of silicon nitride membrane we use is capable of extremely high quality factors of $Q > 10^7$ [133, 74, 65], about two orders of magnitude greater than the quality factors used in this work. With our modular converter design, improvements to any single converter component can be carried out independently. This inherent flexibility will hopefully allow future work to explore new materials and methods and to demonstrate quantum frequency conversion between microwave and optical light.

Chapter 4

Temporal and spectral mode conversion of microwave signals

The radiation pressure interaction between light and a mechanical oscillator can be varied in time, as initially pointed out in section 2.5. Additionally, a mechanical oscillator can be used to create a tunable capacitor. In this chapter, we combine these two capabilities and create a 'temporal and spectral mode converter' that can manipulate the temporal and spectral content of microwave-frequency electromagnetic signals. As a demonstration of our mode converter, we use it to implement a particular protocol that converts the temporal envelope of a 7 GHz microwave signal from a decaying exponential to a Gaussian, and also shifts the signal frequency by up to 250 MHz. We characterize the noise acquired by low-amplitude classical signals during mode conversion, and we find the total added noise is less than one quantum for frequency conversions up to ∼100 MHz, suggesting that our mode converter is suitable for use with fragile quantum signals.

4.1 Analog quantum signal processing is needed in quantum networks

Cavity quantum electrodynamics (cQED) and its low-frequency on-chip counterpart circuit quantum electrodynamics (also cQED) form prototypical quantum systems that have enabled many tests of quantum theory and advanced goals of quantum computation [152, 103]. A single cQED system links a quantum two-level system (a qubit) to the fields in an electromagnetic resonator. Because they naturally interface with electromagnetic fields, multiple cQED systems can be used to form the nodes of a quantum information network linked by photonic channels [41, 107].

To deterministically distribute information over a network made from cQED systems, elec-

tromagnetic signals emitted by one node must be completely absorbed by another [47]. For electromagnetic resonators used in cQED, absorption is the time reverse of emission. For example, the electromagnetic signal in a resonator naturally exits with a temporal envelope of $e^{-\kappa t}$ for resonator energy decay rate κ, but the same electromagnetic resonator only completely absorbs a signal with the time reverse envelope, $e^{\kappa t}$, as can be seen in Eqns. 2.10. Unless somehow time-reversed, a signal emitted by one resonator will not be completely absorbed by another, even if they share the same resonant frequency and energy decay rate. Moreover, because different types of qubits interact with electromagnetic fields at different frequencies [48], both temporal and spectral manipulation of electromagnetic signals are necessary to construct a quantum information network.

Tools that tailor quantum electromagnetic signals have been developed since the late 1990s. At optical frequencies, the most general tools typically use nonlinear materials such as lithium niobate [153, 154], although three-level atomic systems can be used to control the temporal envelope of single photon signals [155, 156]. However, there is a lack of technology that controls the temporal and spectral content of quantum microwave signals. Recent experiments control the temporal content of signals using tunable inductors made from Josephson junctions [157, 158, 159]; other methods exploit the flexibility of superconducting qubits to control the release of single photon signals [160, 161]. In separate experiments, Josephson junctions have been used to convert microwave signals between different frequencies [162, 163, 164]. However, frequency conversion has only been demonstrated between two fixed frequencies, and such conversion is not necessarily compatible with state-of-the-art circuit QED systems which currently use electromagnetic resonators with frequencies that are imprecisely fixed during fabrication [165, 166].

This chapter describes the construction and measurement of a mode converter that can arbitrarily manipulate the temporal and spectral content of electromagnetic signals. The mode converter utilizes the radiation pressure interaction and an electrostatically tunable capacitor to manipulate electromagnetic signals both efficiently and with low added noise, qualities that suggest it can be used with quantum electromagnetic signals. Section 4.2 describes how a membrane made from a tensioned metallic film can couple to a microwave-frequency electromagnetic resonator

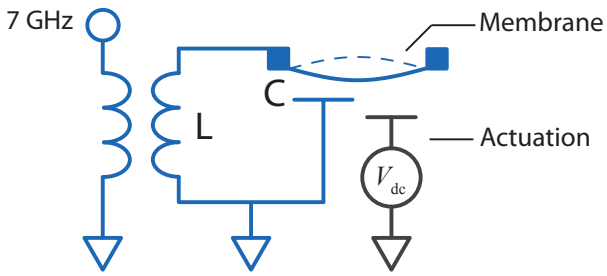

Figure 4.1: Schematic of temporal and spectral mode converter. An aluminum membrane is used to form the capacitor of an inductor (L) and capacitor (C) electromagnetic resonator (shown in blue). Additionally, an actuation circuit (shown in black) can alter the position of the aluminum membrane and thus change the resonant frequency of the microwave circuit.

and simultaneously form a tunable capacitor. Section 4.3 describes how the radiation pressure interaction can be used to manipulate the temporal content of electromagnetic signals. Sections 4.5 and 4.6 demonstrate efficient and low noise manipulation of electromagnetic signals.

4.2 A tunable microwave-frequency optomechanical system

Thin aluminum membranes have been successfully integrated into microwave frequency electromagnetic resonators [136, 167], and our mode converter builds on these advances. We use an aluminum membrane to form two separate parallel-plate capacitors, as diagrammed in Fig. 4.1. One capacitor is used in the microwave-frequency electromagnetic resonator, and as the membrane vibrates it alters this capacitance and thus the resonant frequency, yielding the usual cavity optomechanical coupling. The second capacitor consists of the membrane and an actuation electrode. When a voltage is applied to the actuation electrode, it creates a force on the membrane that pulls the membrane toward the actuation electrode. The net displacement of the membrane increases the capacitance of the microwave circuit and lowers its resonant frequency. Tuning the resonant frequency in this way will allow us to manipulate the spectral content of electromagnetic signals.

4.2.1 Limitations of electrostatically actuated capacitors

Electrostatic actuation of the membrane using a voltage is convenient and relatively easy to implement, but it suffers from practical limitiations. In particular, electrostatic actuation can cause the membrane to collapse and stick to the actuation electrode [168, 169]. Additionally, if the voltage across the collapsed capacitor exceeds the breakdown voltage of any dielectric separating the capacitor [170, 171], the resulting electric discharge typically destroys the entire circuit. Finally, voltage fluctuations on the actuation electrode can incoherently drive vibrations of the aluminum membrane. If not controlled, these fluctuations corrupt electromagnetic signals processed with the membrane.

To understand and design around these problems, consider the simplified system diagrammed in Fig. 4.2a, which shows a parallel plate capacitor formed by an actuation electrode and a membrane. In the absence of any voltage on the actuation electrode, the membrane experiences an approximately harmonic restoring force described by a potential energy $U(x) = k(d-x)^2/2$, where k is the spring constant of the mechanical oscillator formed by the membrane and d is the separation between the membrane's equilibrium position and the actuation electrode. For the membranes we use, the harmonic potential is predominantly provided by tension in the aluminum. When a voltage is applied, $U(x) = k(d-x)^2/2 - C_{\mathrm{dc}}(x)V_{\mathrm{dc}}^2/2$, where C_{dc} is the capacitance between the membrane and the actuation electrode[1] . For a parallel plate capacitor, $C_{\mathrm{dc}} \propto 1/x$. For any $V_{\mathrm{dc}} \neq 0$, the absolute minimum energy configuration of the system is at $x = 0$. However, a meta-stable equilibrium position of the mechanical oscillator near $x \approx d$ can still exist, as shown in Fig. 4.2b, but the dynamics of the membrane are modified. The membrane has a new equilibrium position at $x < d$, and the resonant frequency of the membrane is lowered. Both these effects can be visually seen in Fig. 4.2b, where the harmonic potential is effectively widened with a shifted local minimum.

Beyond a certain voltage, known as the 'pull-in' voltage, V_{pi}, the attractive force between the membrane and the actuation electrode overwhelms the restoring force provided by tension in

[1] The energy stored in the capacitor is of course $C(x)V_{\mathrm{dc}}^2/2$, but a voltage source is also connected to the system. This results in an effective potential of $-C(x)V_{\mathrm{dc}}^2/2$ [172].

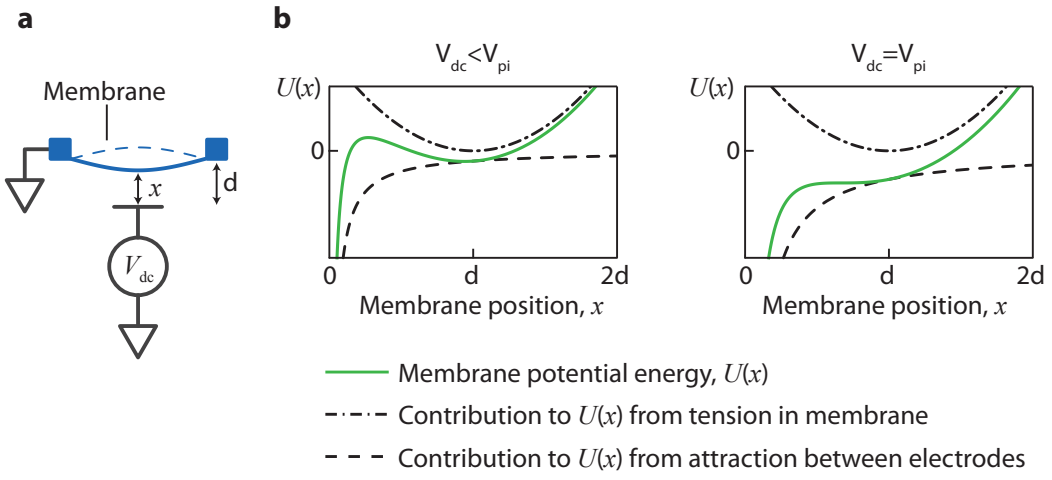

Figure 4.2: Instability of electrostatically actuated capacitor. **a**, A schematic of a tunable capacitor. The aluminum membrane is harmonically bound with frequency ω_{m}, and a nearby actuation electrode forms a capacitance with the membrane. **b**, Potential energy of membrane, with specific contributions indicated as dashed lines, for two different values of the actuation voltage V_{dc}. For $V_{\mathrm{dc}} < V_{\mathrm{pi}}$, there is a stable equilibrium for the membrane at $x \neq 0$. For $V_{\mathrm{dc}} > V_{\mathrm{pi}}$, there is no stable equilibrium other than $x = 0$.

the membrane. The membrane is 'pulled in' to the actuation electrode because there is no stable equilibrium position other than $x = 0$, as indicated in Fig. 4.2c. For the simple schematic in Fig. 4.2a, when $V_{\mathrm{dc}} = V_{\mathrm{pi}}$, the equilibrium position of the membrane is $x = 2d/3$ [173].

The pull-in effect limits the dynamic range of an electrostatically actuated capacitor. If such a capacitor is used in a microwave circuit, under ideal circumstances the resonant frequency of the circuit can only be continuously tuned between ω_0 and approximately $0.8\omega_0$, where ω_0 is the resonator's frequency with $V_{\mathrm{dc}} = 0$. We would like a capacitor that can ideally tune the resonant frequency between ω_0 and 0. Such tunability can potentially be achieved with the circuit shown in Fig. 4.1, provided the separation between the membrane and the actuation electrode is at least three times greater than the separation between the membrane and the microwave electrode. In this case, before the electrostatic instability 'pulls in' the membrane, the capacitance in the microwave circuit has been tuned over its entire working range.

Additionally, the pull-in voltage V_{pi} determines the sensitivity of the membrane to fluctuations

in $V_{\rm dc}$. The force on the membrane is given by $F = -\partial U(x)/\partial x = \partial C_{\rm dc}/\partial x \times V_{\rm dc}^2/2$. For a noisy actuation voltage, $V_{\rm dc} \to V_{\rm dc} + V_{\rm n}$ where $V_{\rm n}$ is a noise voltage that is assumed small relative to the actuation voltage $V_{\rm dc}$. The noise $V_{\rm n}$ creates a force, $F_{\rm n}$, that drives the membrane. For the schematic shown in Fig. 4.2,

$$F_{\rm n} \approx \frac{\partial C_{\rm dc}}{\partial x} V_{\rm dc} V_{\rm n} \propto kd \frac{V_{\rm dc} V_{\rm n}}{V_{\rm pi}^2}. \tag{4.1}$$

For a given separation d and noise voltage $V_{\rm n}$, a larger pull-in voltage results in a lower $F_{\rm n}$. Ideally, $F_{\rm n}$ should be less than the force fluctuations provided by the membrane's coupling to its thermal environment. With a sufficiently large $V_{\rm pi}$ and careful filtering of noise on $V_{\rm dc}$, this can be achieved (see Appendix D for filtering details).

4.2.2 Construction of temporal and spectral mode converter

We create our mode converter by patterning thin films of aluminum on a sapphire substrate following a technique originally developed at NIST Boulder [136]. Multiple layers of aluminum are initially separated by a layer of silicon nitride. Once the silicon nitride is removed, a suspended aluminum membrane remains [174], as shown in Fig. 4.3. (A suspended aluminum membrane without microwave circuitry is shown in Fig. 2.2b.) Two electrodes reside under the aluminum membrane. One completes the capacitor of the microwave-frequency electromagnetic resonator, and a separate annular electrode actuates the membrane. Additional circuitry couples microwave signals to the resonator, and an inductor-capacitor low-pass filter prevents signals in the resonator from coupling to the actuation line (further discussed in Appendix D).

The exact placement of the actuation electrode relative to the aluminum membrane is critical for circuit tunability. As shown in Fig. 4.4a, the actuation electrode is formed by a thin layer of aluminum below the edge of the aluminum membrane. At room temperature both the actuation electrode and the electrode of the microwave resonator are separated from the membrane by approximately 200 nm, as diagrammed in the lower panel of Fig. 4.4a. However, upon cooling to cryogenic temperatures needed to both operate the circuit and remove microwave frequency John-

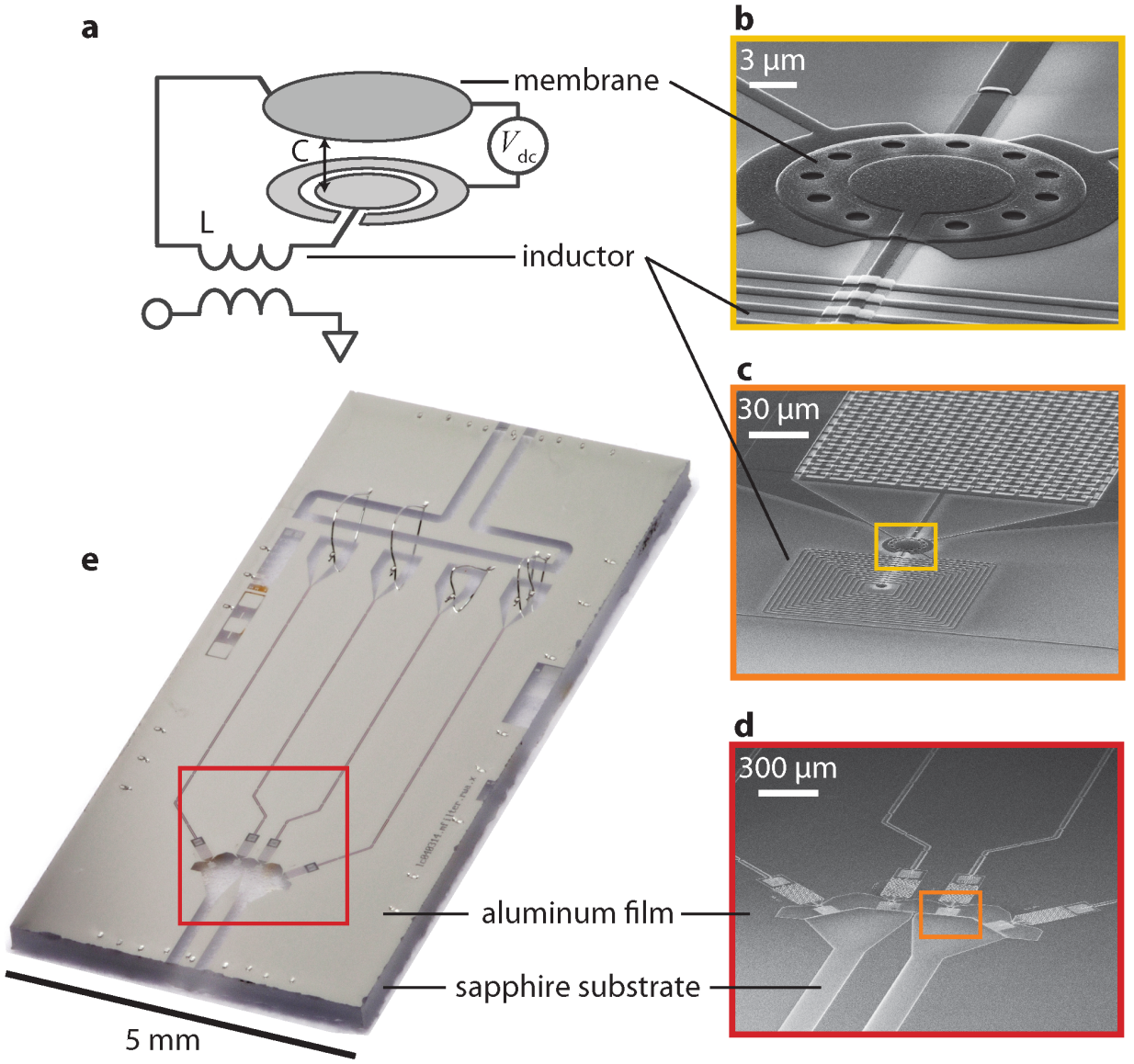

Figure 4.3: Completed temporal and spectral mode converter. **a**, A schematic of the circuit, showing a separate annular actuation electrode and a central microwave capacitor. **b**, Scanning electron micrograph of aluminum membrane, oriented similarly to panel **a**. Actuation electrode and microwave capacitor plate are below the membrane and not directly visible. Only their outline appears in the membrane in the micrograph. **c**, **d**, Progressively zoomed-out view of the aluminum membrane. Signals are coupled to the inductor-capacitor electromagnetic resonator via a transmission line that passes near the inductor (visible as a thin line in **c**), and an inductor-capacitor low-pass filter prevents signals in the resonator from coupling to the actuation line (the capacitor of the filter is visible in the upper portion of **c**). Multiple circuits couple to the same microwave feedline, as visible in **d**. **e**, Photograph of completed sapphire chip that contains the temporal and spectral mode converter.

son noise, the differential thermal contraction between sapphire and aluminum greatly alters the geometry. A finite element simulation of this thermal contraction is shown in Fig. 4.4b. Due to the altered geometry, the separation between the membrane and the actuation electrode is greater than the separation between the membrane and the capacitor plate. Ideally, this geometry circumvents the limitation of electrostatically tunable capacitors discussed in section 4.2.1.

Although this design avoids the instability introduced by electrostatic tuning of the capacitor, any attractive force that increases as two metal films are brought into proximity can affect the circuit's properties. For example, the Casimir force also provides an instablity [175, 176, 177], as do patch potentials [178, 179] that can develop between the aluminum membrane and the electrodes beneath it.

The finite element simulations of the mode converter geometry guide other aspects of construction. In particular, alumium films with different thickness have different bending moments and react differently to the strain created during cooling to cryogenic temperatures. For certain film thicknesses, the capacitor is extremely likely to collapse during cooling to cryogenic temperatures (that is, the displacement of the membrane in Fig. 4.3b is greater than the separation between the two aluminum films). For example, aluminum films with thickness 200 nm separated by 200 nm are predicted to collapse during cooling. The film thicknesses used in this device represent a design choice that creates an aluminum membrane that is free to vibrate at crogenic temperatures, but this choice may not be optimal in some respects.

4.2.3 Initial characterization of mode converter

To verify tunability of the mode converter, we cool it to <25 mK in a dilution refrigerator and measure properties of the mode converter as a voltage is applied to the actuation electrode. As expected, the mode converter responds similarly to both positive and negative voltages (the electrostatic force is $\propto V_{\mathrm{dc}}^2$; see section 4.2.1), and greater magnitude voltages tune the frequency of the electromagnetic resonator, ω_{e}, lower as shown in Fig. 4.5. Unfortunately, the resonator only tunes to about 75% of its maximum resonant frequency before an instability 'pulls in' the membrane

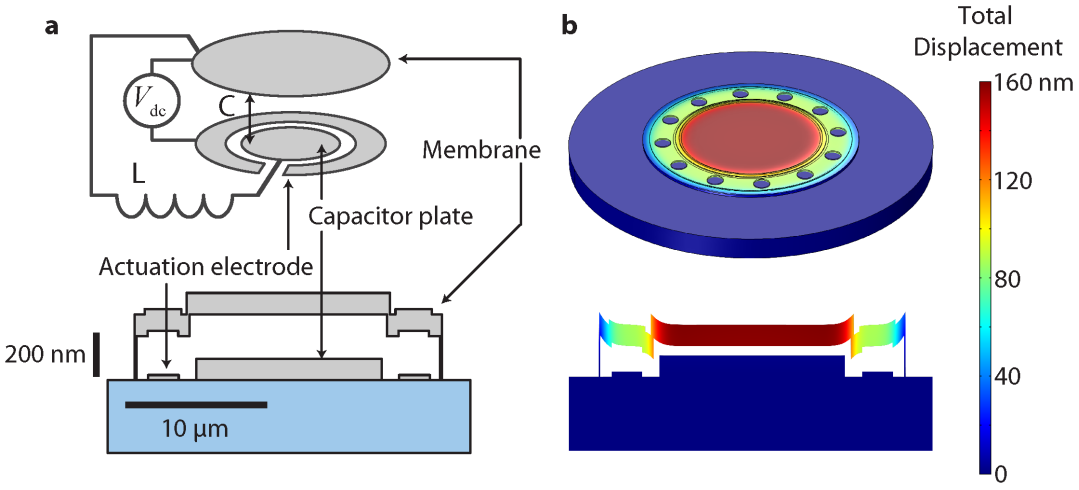

Figure 4.4: Mode converter geometry. **a**, Diagram of the mode converter, and cross section of the parallel plate capacitor that is formed by depositing aluminum films (gray) on a sapphire substrate (light blue). At room temperature, there is approximately 200 nm of separation between the aluminum films. **b**, Finite element simulation of device geometry after cooling from room temperature to cryogenic temperatures. The parallel plate capacitor in the microwave circuit has a separation of approimately 40 nm, while the separation between the actuation electrode and the aluminum membrane is approximately 120 nm.

and collapses the capacitor. The instability also affects the membrane's vibrational modes. At $V_{\mathrm{dc}} = 0$, the lowest frequency vibrational mode of the aluminum membrane has a frequency of $\omega_{\mathrm{m}} \approx 2\pi \times 9.6$ MHz, a frequency set by the 200 MPa of tension created by differential thermal contraction between the sapphire substrate and the aluminum films. As attractive forces between the capacitor plates overwhelm the tension in the membrane, the membrane's vibrational frequency decreases. Just before the capacitor 'pulls in', the membrane's vibrational frequency approaches zero as can be seen in Fig. 4.2b and the data in Fig. 4.5. The pull-in voltage of approximately 17 V represents a rough compromise between low sensitivity to noise and safe, easily generated voltages.

Given the geometry of the aluminum membrane and the underlying electrodes shown in Fig. 4.4, we can predict the frequency tuning of the electromagnetic resonator and the vibrational modes of the membrane. A diagram of the geometry used for finite element simulation is included in Appendix B. If we include only the electrostatic force between the metal films, the performance predicted with a finite element simulation (shown as dashed lines in Fig. 4.5) deviates from the

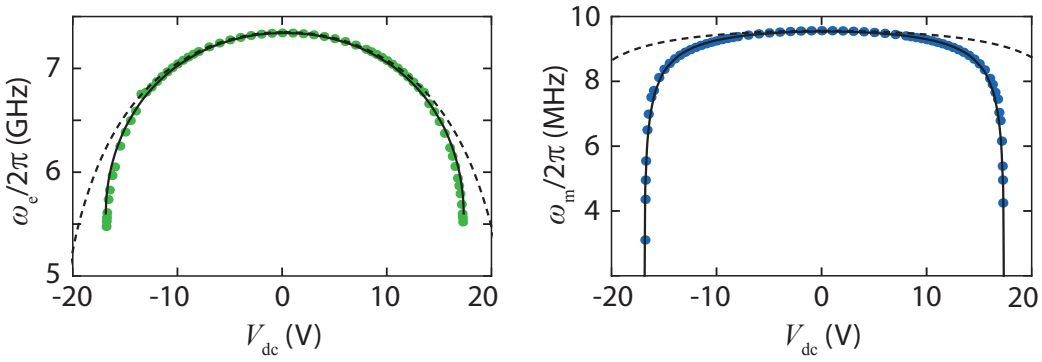

Figure 4.5: Frequency tuning of mode converter. Measured microwave resonant frequency (ω_e) and mechanical resonant frequency (ω_m) of the mode converter as a function of V_{dc}. Solid lines show the expected peformance as calculated with a finite element simulation that includes an attractive force that scales like the Casimir force and is within a factor of two of an estimated Casimir force magnitude. Neglecting this additional attractive force results in the much different behavior shown with the dashed lines.

observed frequency tuning: The predicted pull-in voltage and tuning of the microwave resonator are significantly greater than observed. Only when we include an additional attractive force that scales like the Casimir force and is within a factor of two of an estimated Casimir force magnitude [180] does the performance predicted with a finite element simulation (shown as solid lines in Fig. 4.5) agree with the observed frequency tuning.

Although incorporation of the Casimir force accounts for our data reasonably well, we can not rule out some contribution from patch potentials [178]. For this reason we view the data in Fig. 4.5 not as a measurement of the Casimir force, but as strong evidence that the Casimir force plays a crucial role in determining performance of the mode converter. Given its significance, the Casimir force can potentially be used to counter the 'pull-in' effect from electrostatic forces: it is perhaps possible to engineer repulsive Casimir forces that prevent the capacitor from collapsing [181, 182]. Such a repulsive force could be used to increase the frequency tunability of the electromagnetic resonator. Nevertheless, the current device can be tuned over approximately 2 GHz, an amount sufficient to demonstrate spectral control of electromagnetic fields.

Table 4.1: Parameters of temporal and spectral mode converter.

Parameter	Value	Units
g	$2\pi\times1^*$	MHz
ω_e	$2\pi\times7.34^\dagger$	GHz
κ_{ext}	$2\pi\times2.3$	MHz
κ_{int}	$2\pi\times200$	kHz
κ	$\kappa_{ext}+\kappa_{int}$	
ω_m	$2\pi\times9.6^\dagger$	MHz
κ_m	$2\pi\times25$	Hz
n_m	36	

*Adjustable up to this value via the microwave pump.
†Quoted values are with $V_{dc}=0$ V

4.3 Radiation pressure interaction is naturally tunable

The mode converter described in section 4.2 consists of a mechanical oscillator coupled to a tunable electromagnetic resonator. Although the tunable resonant frequency will allow for spectral control of electromagnetic signals, the radiation pressure coupling provides temporal control. As noted in section 2.4, a time dependent radiation pressure coupling arises when the nonlinear interaction between light and a mechanical oscillator is linearized in the presence of a large pump. To see how this tunability can be used to manipulate electromagnetic signals, consider the equations of motion for a mechanical oscillator and an electromagnetic resonator in the presence of a strong pump. Using Eqns. 3.3 with only one electromagnetic resonator, we have

$$\begin{aligned} a(t) &= \frac{-2\imath g}{\kappa}c(t)+\frac{2}{\kappa}\sqrt{\kappa_{ext}}a_{in}(t) \\ \dot{c}(t) &= -\frac{1}{2}\left(\kappa_m+\frac{4|g|^2}{\kappa}\right)c(t)-\frac{2\imath g^*}{\sqrt{\kappa}}\frac{\sqrt{\kappa_{ext}}}{\sqrt{\kappa}}a_{in}(t) \end{aligned} \tag{4.2}$$

Using the relation $a_{out}=\sqrt{\kappa_{ext}}a(t)-a_{in}(t)$, the dynamics of the system are described by

$$\begin{aligned} \dot{c}(t) &= -\frac{1}{2}\left(\kappa_m+\Gamma(t)\right)c(t)-e^{-\imath\psi}\sqrt{\eta\Gamma(t)}a_{in}(t) \\ a_{out}(t) &= e^{\imath\psi}\sqrt{\eta\Gamma(t)}c(t)+(2\eta-1)a_{in}(t) \end{aligned} \tag{4.3}$$

where $\Gamma(t)=4|g|^2/\kappa$, $\eta=\kappa_{ext}/\kappa$, and $\psi=\mathrm{Arg}(-\imath g)$. A schematic of Eqns. 4.3 is shown in Fig. 4.6.

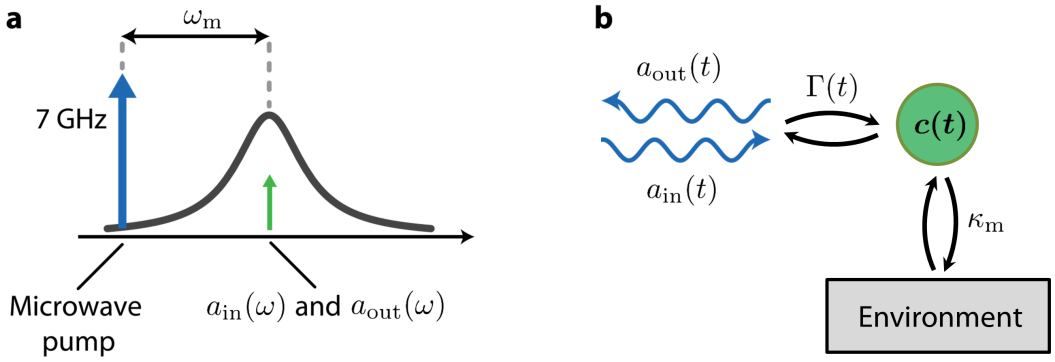

Figure 4.6: Time-dependent coupling between propagating electromagnetic fields and a mechanical oscillator. **a** A microwave pump (blue arrow) is applied at a frequency ω_m below the microwave resonator (response shown as a black curve). **b** The microwave pump determines $\Gamma(t)$, which couples incoming and outgoing microwave fields to vibrations of the mechanical oscillator.

Eqns. 4.3 describe how a freely propagating electromagnetic field, $a_{in}(t)$, couples to vibrations of a mechanical oscillator, $c(t)$. There is a strong formal similarity between Eqns. 4.3 and those of an electromagnetic resonator coupled to a transmission line, Eqns. 2.10: Both describe a freely propagating electromagnetic field coupled to a resonator. For the formal mapping to be near-exact, we require $\Gamma(t) \gg \kappa_m$ and $\eta \approx 1$. Parameters of our mode converter (see table 4.1) approximately satisfy these requirements. This formal simlarity implies that both a simple electromagnetic resonator and our mode converter have similar signal processing capabilities. However, for the mode converter, both the strength of the coupling $\Gamma(t)$ and its phase ψ can be modulated by changing the amplitude and phase of a microwave pump. This tunability is generally not available with electromagnetic resonators, where the coupling to propagating fields is often fixed during construction.

A tunable coupling is key to manipulating the temporal content of electromagnetic signals [183, 184]. Consider an incoming signal $a_{in}(t)$ with a temporal envelope as shown in Fig. 4.7. We can use the mode converter to change the temporal content of this signal by implementing the following protocol, which is diagrammed in Fig. 4.7. First, $\Gamma(t)$ is modulated so that the incoming signal, $a_{in}(t)$, is optimally captured as a vibration of the mechanical oscillator. If $\eta \approx 1$, optimally

capturing the signal is equivalent to minimizing the reflected signal, $a_{\mathrm{out}}(t)$, for times $0 < t < t_1$. Minimizing the energy in the reflected signal, $\int_0^{t_1} |a_{\mathrm{out}}(t)|^2 dt$, with $\eta = 1$ requires a coupling $\Gamma(t)$ of [185][2]

$$\Gamma(t) = \frac{e^{\kappa_{\mathrm{m}} t}|a_{\mathrm{in}}(t)|^2}{\frac{a_{\mathrm{in}}(0)^2}{\Gamma(0)} + \int_0^t e^{\kappa_{\mathrm{m}} t'}|a_{\mathrm{in}}(t')|^2 dt'} \tag{4.4}$$

where $\Gamma(0)$ is the coupling at $t = 0$. Once the incoming signal is captured, $\Gamma(t) = 0$ for $t_1 < t < t_2$. During this time, the captured signal is stored as a vibration of the mechanical oscillator. Beginning at time $t = t_2$, $\Gamma(t)$ is modulated to recover the signal with the desired waveform. An experimental implementation of this temporal mode conversion protocol is given in section 4.5.

For the temporal mode conversion protocol to be successful, it must manipulate electromagnetic signals before they are corrupted or lost. For an optomechanical mode converter, the entire protocol should be completed before the mechanical oscillator acquires one phonon from its environment, which occurs at the mechanical decoherence rate $n_{\mathrm{m}}\kappa_{\mathrm{m}}$. However, signals can only be manipulated with bandwidth Γ. Arbitrary control over the temporal content of signals thus requires $\Gamma \gg n_{\mathrm{m}}\kappa_{\mathrm{m}}$. A similar figure of merit is used in optical signal processing, where a large bandwidth-delay product (BDP) indicates large signal processing power [186]. For an optomechanical system, BDP $\approx \Gamma/n_{\mathrm{m}}\kappa_{\mathrm{m}}$. Our mode converter approaches BDP $\gg 1$ with a maximum $\Gamma \approx 2\pi \times 1$ MHz and a decoherence rate $n_{\mathrm{m}}\kappa_{\mathrm{m}} \approx 2\pi \times 1$ kHz, or a BDP of 10^3.

4.3.1 Relation between optomechanical coupling and mechanical resonant frequency

Eqns. 4.3 allow temporal control of electromagnetic fields; however, these equations of motion are an approximation of the radiation pressure interaction assuming the resolved-sideband regime, $4\omega_{\mathrm{m}} \gg \kappa$. In this regime, with the specified pump detuning $\Delta = -\omega_{\mathrm{m}}$, the mechanical oscillator experiences an additional damping $\Gamma(t) = 4|g(t)|^2/\kappa$ and a frequency shift $\Omega = 0$, as given by Eqns. 2.26. Even though our mode converter is in the resolved-sideband regime (see table 4.1), the

[2] This coupling can be found by using the Euler-Lagrange equation to find a stationary point of the the reflected energy, $\int_0^{t_1} |a_{\mathrm{out}}(t)|^2 dt$, with $a_{\mathrm{out}}(t)$ as given by Eqns. 4.3.

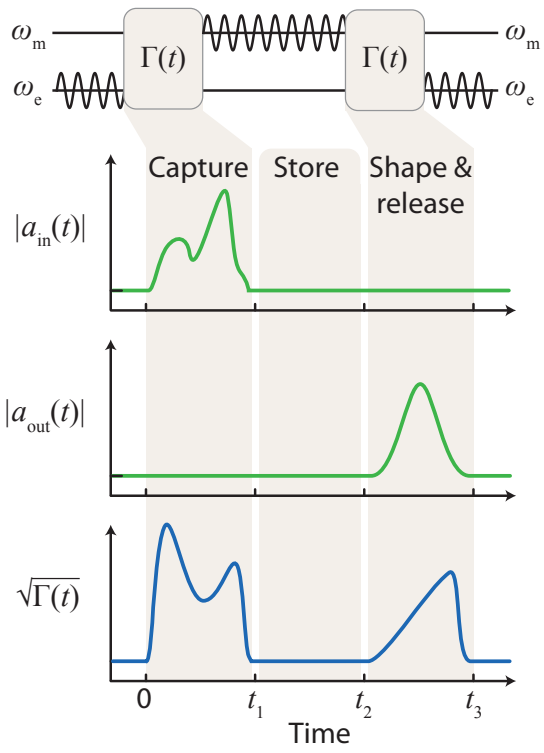

Figure 4.7: Protocol for temporal mode conversion. An incoming microwave signal, $a_{\mathrm{in}}(t)$, at frequency ω_{e} is first captured as a vibration of the mechanical oscillator by modulating $\Gamma(t)$ (blue waveform). After an adjustable storage time, the signal is released from the mechanical oscillator into outgoing microwave signal, $a_{\mathrm{out}}(t)$, by modulating $\Gamma(t)$.

microwave pump still slightly alters the frequency of the mechanical oscillator. For a pump with detuning $\Delta = -\omega_{\mathrm{m}}$, $\Omega(t)/\Gamma(t) \approx -\kappa/8\omega_{\mathrm{m}}$, a ratio that is independent of pump amplitude. As $\Gamma(t)$ is modulated to shape an outgoing microwave signal, the corresponding change in $\Omega(t)$ 'chirps' the frequency of the signal. This effect can be corrected by altering the frequency of the pump by $-\Omega(t) = \kappa\Gamma(t)/8\omega_{\mathrm{m}}$. We use this correction when operating our mode converter.

4.4 Measurement network

We create a measurement network that allows us to inject microwave signals into the mode converter and carefully measure signals reflected or emitted from the mode converter. The main components of the network are diagrammed in Fig. 4.8. A combination of arbitrary waveform

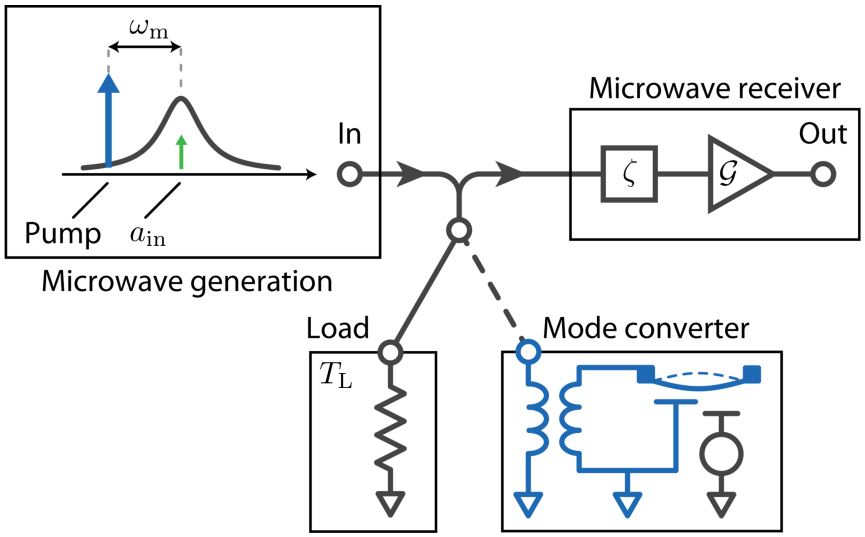

Figure 4.8: Measurement network. A signal and a pump are created using standard microwave techniques and injected into the mode converter. A microwave receiver measures signals reflected or emitted from the mode converter. To calibrate the efficiency ζ and gain $\mathcal{G}$, a resistive load with a variable temperature injects Johnson noise into the microwave receiver. A detailed schematic that includes components used in microwave generation is included in Appendix D

generators and microwave mixers generates a microwave pump and signal with programmable amplitude, frequency, and phase. A microwave receiver measures signals after they have interacted with the converter. The performance of the receiver is characterized by an efficiency ζ, and a gain, $\mathcal{G}$. The efficiency can in principle range between 0 (no measurement) and 1 (perfect measurement), and the gain expresses how a spectral density at the input of the receiver is converted to a spectral density at the output. To calibrate the microwave receiver, the measurement network includes a resistive load whose temperature T_L can be varied. Once a signal is amplified, it is downconverted with a frequency mixer and digitized. Data collected thus consist of time-stamped voltage values. A detailed schematic of the measurement network is included in Appendix D.

4.4.1 Calibration of microwave receiver

The microwave receiver employs a Josephson parametric amplifier (JPA) [187]. The JPA amplifies one quadrature of a microwave signal and deamplifies the other, where a quadrature is composed of linear combinations of signals at frequencies above and below the JPA's pump fre-

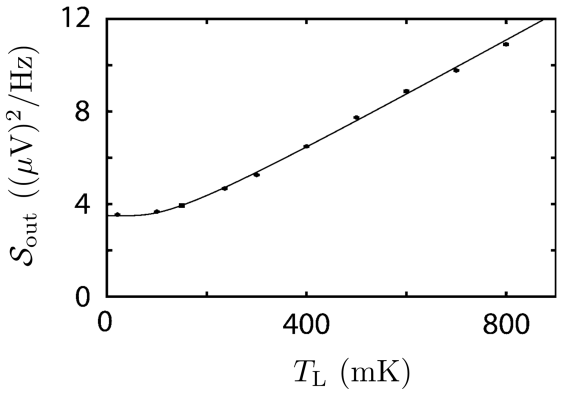

Figure 4.9: Calibration of microwave receiver. The output spectral density of the microwave receiver varies with the temperature of the load. A fit to Eqn. 4.6 (solid line) shows the receiver has an efficiency of $\zeta' = 0.6$ and a gain $\mathcal{G} = 7(\mu\text{V})^2/(\text{Hz} \cdot \text{quanta})$.

quency [188, 189]. Before amplification or deamplification, the spectral density of each quadrature emitted by the resistive load is given by, in units of quanta (a quanta corresponding to a photon per second per unit bandwidth),

$$\mathcal{S}_{\rm L} = \frac{1}{2}\coth\left(\frac{\hbar\omega}{2k_{\rm B}T_{\rm L}}\right) \tag{4.5}$$

where $T_{\rm L}$ is the temperature of the resistive load [189]. At temperatures $T_{\rm L} \ll \hbar\omega/k_{\rm B}$, $S_{\rm L}$ approaches 1/2 quantum. At these low temperatures, the total spectral density of both quadratures is thus 1 quantum, consistent with the convention that each unit of bandwidth has a minimum spectral density of 1/2 quantum [93]. Similarly, at temperatures $T_{\rm L} \gg \hbar\omega/k_{\rm B}$, the total power emitted in both quadratures by the resistive load is $2k_{\rm B}T_{\rm L}/\hbar\omega$, the classical Johnson noise formula for two units of bandwidth.

Once measured by the microwave receiver, we expect to observe a spectral density given by [190]

$$\mathcal{S}_{\rm out} = \mathcal{G}\left(\frac{1-\zeta'}{2} + \zeta'\mathcal{S}_{\rm L}\right). \tag{4.6}$$

Fitting this model to the measured receiver output at $\omega = 2\pi \times 7.34$ GHz yields $\zeta' = 0.6$ and $\mathcal{G} = 7.0$ $(\mu\text{V})^2/(\text{Hz} \cdot \text{quanta})$, as shown in Fig. 4.9.

We use the microwave receiver to measure signals reflected or emitted from the mode converter. These signals are entirely contained in frequencies above the JPA pump frequency. As such, the measured signal is contained neither in the amplified or deamplified quadratures, but in both. The signal in the deamplified quadrature is not measured and this loss of information reduces the efficiency of our microwave receiver by a factor of two, so $\zeta = \zeta'/2 = 0.30$. The maximum possible efficiency for this mode of operation is $\zeta = 0.5$ [127].

4.5 Temporal mode conversion of microwave signals

As an initial test of our measurement network, we generate a microwave signal and measure it with the microwave receiver. The signal is centered at the mode converter's resonant frequency of $\omega_e = 2\pi \times 7.34$ GHz (with $V_{dc} = 0$) and has an exponentially rising temporal envelope: $|a_{in}(t)| \propto (1 - \Theta(t - t_1))e^{(t-t_1)\gamma/2}$, where $\Theta(t)$ is the Heaviside step function and $\gamma = 2\pi \times 24$ kHz. This waveform is shown in Fig. 4.10a. Initially, we inject no microwave pump. With no pump, $\Gamma(t) = 0$ and $a_{out}(t) \approx a_{in}(t)$ as indicated by Eqns. 4.3. The measured signal, shown in Fig. 4.10b, is consistent with this prediction and confirms the signal generation and microwave receiver function as expected.

In order to manipulate the temporal content of the incoming microwave signal, we must modulate $\Gamma(t)$. To capture an incoming signal with a rising exponential envelope as a vibration of the mechanical oscillator, we inject a constant microwave pump so that $\Gamma(t) = \gamma$ during signal capture. By pulsing $\Gamma(t)$ between $\Gamma(t) = \gamma$ and $\Gamma(t) = 0$, we capture, store, and retrieve the incoming microwave signal, as shown in Fig. 4.11. This protocol stores the incoming microwave signal and reverses its temporal envelope [58].

In order to arbitrarily manipulate the temporal content of an incoming signal, $\Gamma(t)$ must be carefully chosen. Consider, for example, an incoming microwave signal with a decaying exponential temporal envelope: $|a_{in}(t)| \propto \Theta(t)e^{-\gamma t/2}$. This temporal envelope is ubiquitous, and in particular highly coherent circuit QED systems produce quantum electromagnetic signals with similar envelopes [166, 165]. A microwave pump pulsed so that $\Gamma(t) = \gamma$ or $\Gamma(t) = 0$ does not efficiently

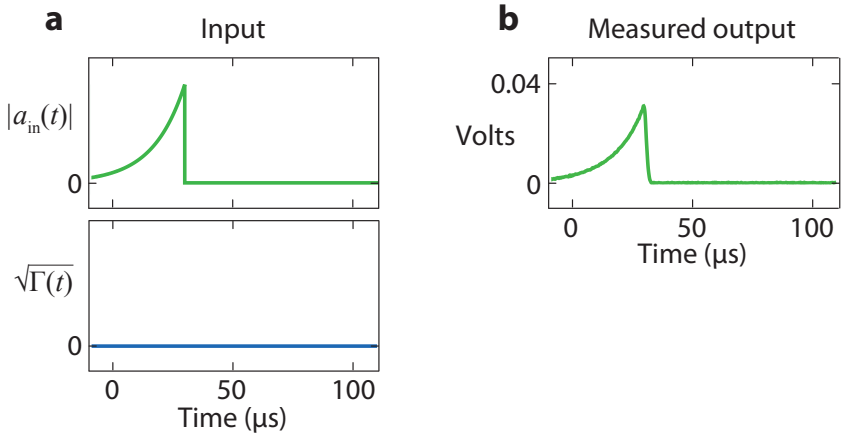

Figure 4.10: Test of microwave receiver. **a**, A signal with a rising exponential temporal envelope (green waveform) is injected into the mode converter. Because no pump is injected, $\Gamma(t) = 0$ and the incoming signal should reflect off the mode converter. **a**, Outgoing microwave signal as measured with our microwave receiver. As expected, the outgoing signal has the same temporal envelope as the injected signal.

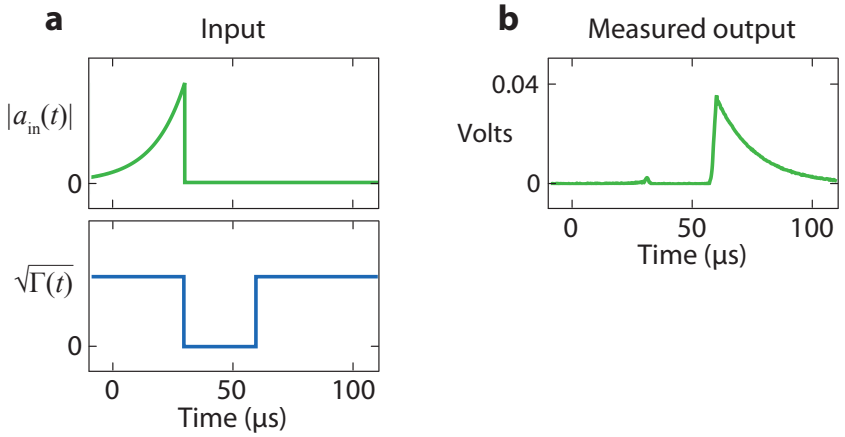

Figure 4.11: Storage of microwave signals. **a**, A microwave signal (green waveform) and a pump are injected into the mode converter. **b**, By pulsing $\Gamma(t)$, the signal is temporarily stored as a vibration of the mechanical oscillator and later recovered with a decaying exponential temporal envelope.

capture an incoming signal with a decaying exponential temporal envelope. As demonstrated in Fig. 4.12, much of the incoming signal is reflected and only a fraction is stored as a vibration of the mechanical oscillator and later retrieved. To efficiently capture this signal, $\Gamma(t)$ must be modulated as prescribed by Eqn. 4.4:

$$\Gamma(t) = \Theta(t)\frac{\gamma e^{-\gamma t}}{1 - e^{-\gamma t} + \gamma/\Gamma(0)} \tag{4.7}$$

where I've assumed $\gamma \gg \kappa_{\mathrm{m}}$ and $\Gamma(0)$ is an input; $\Gamma(0) \gg \gamma$ yields a high capture efficiency. We use $\gamma = 2\pi \times 24$ kHz and $\Gamma(0) \approx 2\pi \times 500$ kHz. As demonstrated in Fig. 4.13a, this choice of $\Gamma(t)$ efficiently captures the incoming signal as a vibration of the mechanical oscillator. We choose to release the signal with a Gaussian temporal envelope, as shown in Fig. 4.13b, because Gaussian envelopes are time-reverse symmetric and are relatively compact in both time and frequency. The coupling necessary to produce a Gaussian envelope centered at time $t = t_{\mathrm{o}}$ can be found using Eqn. 4.4:

$$\Gamma(t) = \frac{\gamma e^{-\gamma^2 (t-t_{\mathrm{o}})^2}}{1 - \mathrm{erf}\left(\gamma(t - t_{\mathrm{o}})\right) + \delta} \tag{4.8}$$

where $\mathrm{erf}(t)$ is the error function, $\gamma = 2\pi \times 24$ kHz, and $\delta \approx \gamma/\Gamma(0) e^{-\gamma^2 t_{\mathrm{o}}^2}$ [185].

4.6 Temporal and spectral mode conversion of microwave signals

To incorporate spectral mode conversion into our protocol for temporal mode conversion, we utilize the signal storage capability of the mode converter. As can be seen in Figs. 4.11 and 4.13, our temporal mode conversion protocol stores microwave signals for approximately 30 μs. We can use this time to alter the center frequency of the electromagnetic resonator by adjusting V_{dc}. This allows a microwave signal captured at one frequency to be released from the mode converter at another. A protocol for temporal and spectral mode conversion is diagrammed in Fig. 4.14.

4.6.1 Wigner-Ville distribution

Signals emitted from the mode converter have different temporal and spectral content depending on the details of the mode conversion protocol. To clearly represent the voltage waveform measured by our microwave receiver, we construct the Wigner-Ville distribution using the discretized version of $W(t, f) = \int_{-\infty}^{\infty} v(t + \tau/2) v^*(t - \tau/2) e^{2\pi \imath f \tau} d\tau$, where $W(t, f)$ is the Wigner-Ville distribution and $v(t)$ is the analytic voltage measured at time t. The analytic voltage is constructed using a Hilbert transform on the measured voltage [191]: $v(t) = V(t) + \imath \mathcal{H}(V(t))$, where $V(t)$ is the voltage measured at time t and $\mathcal{H}$ is the Hilbert transform. The resulting time-frequency

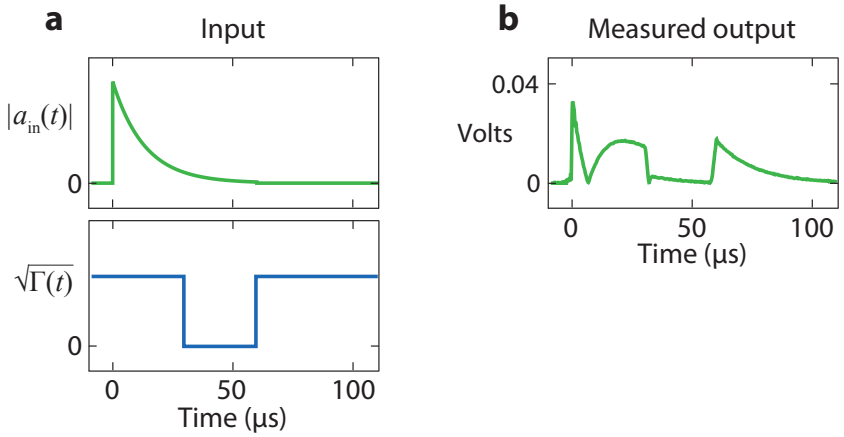

Figure 4.12: Sub-optimal temporal mode conversion of a microwave signal. **a**, A signal with a decaying exponential temporal envelope (green waveform) and a pulsed pump (blue waveform) are injected into the converter. **b**, Much of the incoming signal is reflected from the mode converter; only a fraction is captured as a vibration of the mechanical oscillator and later released.

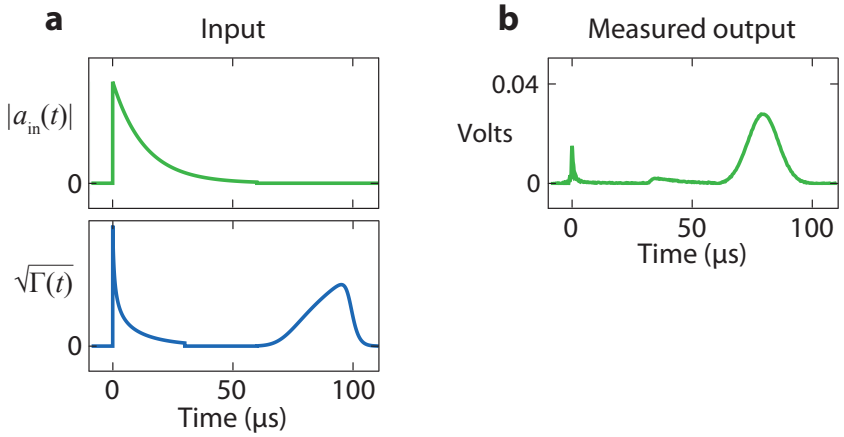

Figure 4.13: Temporal mode conversion of a microwave signal. **a**, A signal with a decaying exponential envelope (green waveform) and an optimally shaped microwave pump (blue waveform) are injected into the mode converter. **b**, The vast majority of the incoming microwave signal is captured as a vibration of the mechanical oscillator, and emitted as an outgoing microwave signal with a Gaussian temporal envelope.

distribution is similar to the position-momentum Wigner quasiprobability distribution.

Although there are many ways to represent the temporal and spectral content of signals [192], the Wigner-Ville distribution has several convenient properties. The marginal distributions of the Wigner-Ville distribution give the temporal envelope and energy spectral density of the signal: $|v(t)|^2 = \int_{-\infty}^{\infty} W(t,f)df$ and $|v(f)|^2 = \int_{-\infty}^{\infty} W(t,f)dt$. Additionally, the Wigner-Ville distribution

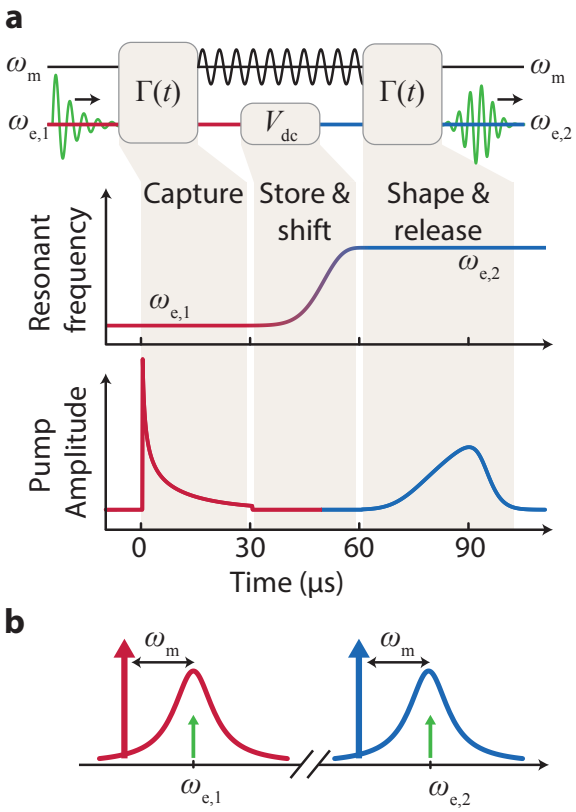

Figure 4.14: Protocol for temporal and spectral mode conversion. **a**, An incoming signal at frequency $\omega_{e,1}$ (green sinusoid) is first converted into a vibration of the aluminum drumhead (black sinusoid). $\Gamma(t)$ is adjusted by varying the power in a pump at frequency $\omega_{e,1} - \omega_m$ (red waveform). Then, we alter the frequency of the microwave circuit by changing V_{dc}. During this time, the signal is stored as a vibration of the mechanical oscillator; the change in V_{dc} adiabatically changes ω_m by approximately $2\pi \times 300$ kHz. Finally, the signal is released from the mechanical oscillator into an outgoing microwave signal at frequency $\omega_{e,2}$ by adjusting the power in a pump at frequency $\omega_{e,2} - \omega_m$ (blue waveform). **b**, Frequency domain picture of mode conversion. Microwave pumps (red and blue arrows) applied at a frequency ω_m below the microwave circuit (response shown as the red and blue curves) allow a signal at frequency $\omega_{e,1}$ to be converted to a signal at frequency $\omega_{e,2}$ (green arrows).

provides high temporal and spectral resolution [193]. However, the marginal properties and resolution of the Wigner-Ville distribution necessarily imply $W(t, f)$ can be negative [193]. Unlike the position-momentum Wigner quasiprobability distribution, nothing 'quantum' is associated with negative values of $W(t, f)$.

4.6.2 Temporal and spectral mode conversion

We generate a signal near 7.08 GHz that has a decaying exponential envelope (power decay rate of $2\pi \times 24$ kHz) and inject it into the mode converter. Initially, we set V_{dc} so that the microwave circuit has a resonant frequency substantially different from the injected signal, and the signal reflects off the mode converter and is measured by our microwave receiver. The measured Wigner-Ville distribution of the injected signal is shown in Fig. 4.15a, with the data normalized by $E_{\mathrm{sig}} = \int_{-\infty}^{\infty} |v_{\mathrm{sig}}(t)|^2 dt$.

To perform mode conversion, we set $V_{\mathrm{dc}} \approx 10$ V so the microwave circuit is centered near 7.08 GHz, and send in the decaying exponential envelope signal. We apply a microwave pump with a time-dependent amplitude so that $\Gamma(t)$ is given by Eqn. 4.7. Only a small amount (about 4%) of the signal energy is reflected off the converter, as demonstrated in Fig. 4.15b. We then set $V_{\mathrm{dc}} = 0$ so that the microwave circuit is centered near 7.34 GHz, and again apply a microwave pump with a time dependent so that $\Gamma(t)$ is given by Eqn. 4.8. The Wigner-Ville distribution of the signal emitted by the mode converter is plotted in Fig. 4.15b. From the relative energies in the reflected and converted signals, we find the photon number efficiency of the conversion process to be 0.81, in good agreement with an expected efficiency of $(\kappa_{\mathrm{ext}}/\kappa)^2 \times 0.96 = 0.81$ where 0.96 is the efficiency with which we capture the injected signal [185].

The mode converter can be used to change signals between arbitrary temporal and spectral modes. We demonstrated frequency conversion over approximately 250 MHz; conversion over a larger window is feasible but the mode converter becomes more sensitive to fluctuations in V_{dc} at higher bias. And although we altered the temporal envelope of a microwave signal from a decaying exponential to a Gaussian, other envelopes are possible, only limited by the bandwidth of the converter. The maximum bandwidth is set by the rate at which information can be exchanged between the transmission line and the drumhead, which for this device is limited by the microwave circuit's bandwidth of $\Gamma < \kappa/2 \approx 2\pi \times 1$ MHz. The minimum bandwidth is set by the mechanical decoherence rate. Even though energy in the drumhead is lost to the environment at the modest

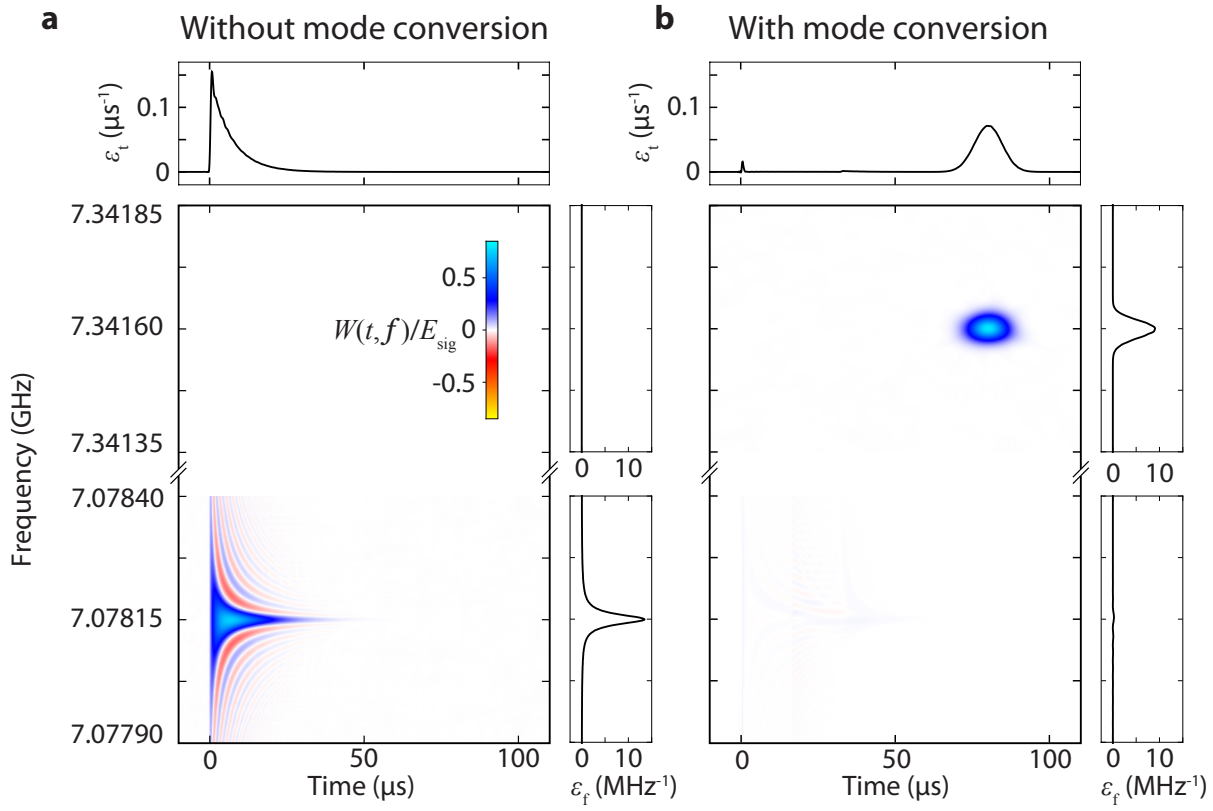

Figure 4.15: Temporal and spectral mode conversion of a microwave signal. **a**, Wigner-Ville distribution of a signal that reflects off the mode converter (so no mode conversion is performed) and is measured with a microwave receiver. The marginal distributions of the Wigner-Ville distribution show the signal is a decaying exponential in time, and a Lorentzian in frequency; $\epsilon_t = |v(t)|^2/E_{sig}$ and $\epsilon_f = |v(f)|^2/E_{sig}$. The signal is centered near 7.07815 GHz and has a power decay rate of $2\pi \times 24$ kHz. There is no signal content near 7.34160 GHz. **b**, Wigner-Ville distribution of a mode-converted signal. When the mode converter is used, the decaying exponential microwave signal is captured as a vibration of the mechanical oscillator, and the signal content at 7.07815 GHz is almost entirely absent. Later in time, we recover the signal that is now centered near 7.34160 GHz and has a Gaussian temporal envelope and Gaussian spectral content with width $2\pi \times 24$ kHz.

rate of $\kappa_{\mathrm{m}} = 2\pi \times 25$ Hz, fluctuations of the environment incoherently drive vibrations of the drumhead. To avoid these environment-driven vibrations, signals must be processed faster than the mechanical decoherence rate of $n_{\mathrm{m}}\kappa_{\mathrm{m}} = 2\pi \times 900$ Hz. Avoiding excess vibrations is essential when manipulating fragile quantum signals.

4.6.3 Operation at the quantum level

4.6.3.1 Quadrature amplitudes of microwave signals

In order to analyze signals at the quantum level, we would like to express a measured signal in units of photon flux per unit bandwidth, or quanta, referred to the input of the receiver. For a continuous wave signal, we can express the signal in quanta using a Fourier transform of the measured voltage waveform. In this case, we define quadrature amplitudes at a frequency ω:

$$\begin{aligned} X_1 &= \sqrt{\frac{2}{\zeta\mathcal{G}}} \cdot \sqrt{\frac{\delta t}{N}} \cdot \sum_{k=1}^{N} y(k) \cdot \cos(\omega \cdot k \cdot \delta t) \\ X_2 &= \sqrt{\frac{2}{\zeta\mathcal{G}}} \cdot \sqrt{\frac{\delta t}{N}} \cdot \sum_{k=1}^{N} y(k) \cdot \sin(\omega \cdot k \cdot \delta t) \end{aligned} \tag{4.9}$$

where $y(k)$ is the measured voltage waveform of length N, and $1/\delta t$ is the sample rate. The factor $\sqrt{2/(\zeta\mathcal{G})}$ converts the voltage waveform into units of $\sqrt{\text{quanta} \cdot \text{Hz}}$ at the input of the receiver (the factor of two is present because $\mathcal{G}$ was calculated using a single-sided spectral density). X_1 and X_2 are proportional to the real and imaginary parts of the complex Fourier amplitude, and can be considered to represent the magnitude and phase of the signal: $X_1^2 + X_2^2$ yields an estimate of the number of quanta contained in the signal, and $\arctan(X_2/X_1)$ the phase of the signal.

Eqns. 4.9 are appropriate when the signal is continuous and at a known frequency. When a signal has a particular temporal envelope, this definition no longer provides an accurate description of the signal. To compensate for the broader bandwidth of the signal, we define quadrature amplitudes using a Fourier transform with a window function where the window function matches the temporal envelope of the signal. This window function prevents the quadrature amplitudes from

being affected by noise that occurs either before or after the signal.

$$X_1 = \sqrt{\frac{2}{\zeta \mathcal{G}}} \cdot \sqrt{\frac{\delta t}{C}} \cdot \sum_{k=1}^{N} f(k) \cdot y(k) \cdot \cos(\omega \cdot k \cdot \delta t)$$
$$X_2 = \sqrt{\frac{2}{\zeta \mathcal{G}}} \cdot \sqrt{\frac{\delta t}{C}} \cdot \sum_{k=1}^{N} f(k) \cdot y(k) \cdot \sin(\omega \cdot k \cdot \delta t) \tag{4.10}$$

where $f(k)$ is the temporal envelope of the signal and $C = \sum_{k=1}^{N} |f(k)|^2$ is a factor that compensates for the noise equivalent bandwidth of $f(k)$.

Using the window function $f(k)$ with a Fourier transform is equivalent to using least squares parameter estimation, where the parameters to be estimated are the amplitudes of $f(k) \cdot \cos(w \cdot k \cdot \delta t)$ and $f(k) \cdot \sin(w \cdot k \cdot \delta t)$. This method of parameter estimation is appropriate when noise in the voltage waveform is Gaussian, as is the case for our measurements [194].

4.6.3.2 Noise added during mode conversion

To verify that our converter operates quickly and quietly enough to avoid corrupting signals, we collect statistics on single-shot measurements of mode conversion using low amplitude ($\sim$ 10 quanta of energy) signals. We inject a low-amplitude signal with a decaying exponential envelope into the converter, shift its frequency by 90 MHz, and recover a signal with a Gaussian envelope. The central frequency and temporal envelope of the converted signal are already known, and we use this information and Eqns. 4.10 to estimate the quadrature amplitudes X_1 and X_2. The result of each single shot measurement and quadrature amplitude estimation appears as a single point in Fig. 4.16a. The scatter of the quadrature amplitudes indicates the total amount of noise added to the signal during preparation, mode conversion, and measurement. By comparing the total variance, $\mathrm{Var}(X_1) + \mathrm{Var}(X_2)$, of the converted signal with that of measured vacuum noise, we infer the mode converter adds 0.92 ± 0.07 quanta of noise during conversion with a 90 MHz frequency shift, indicating compatibility with fragile quantum states [195].

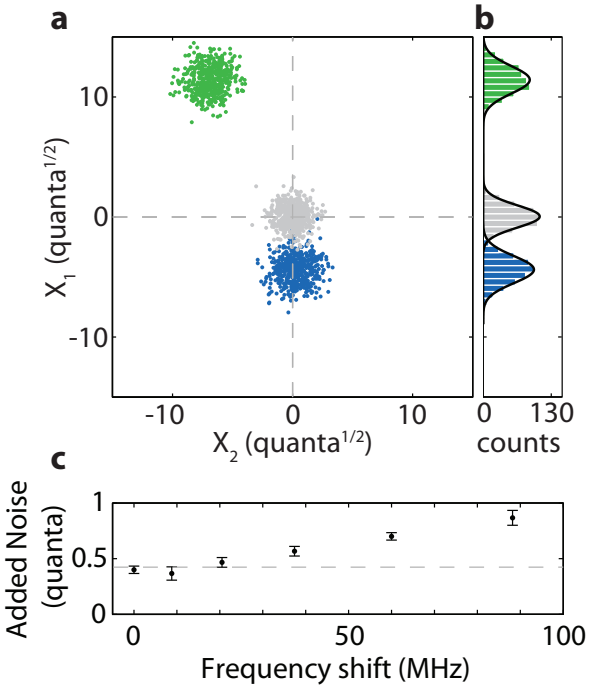

Figure 4.16: Noise added during mode conversion. **a**, Quadrature amplitudes for 500 independent repetitions of the mode conversion protocol. Results of conversion with a 90 MHz frequency shift with a signal containing ∼10 quanta (blue points) and ∼100 quanta (green points) of energy. Low and high amplitude signals are intentionally generated with different phases. For reference, a vacuum input into our microwave receiver yields the gray points. The total variance of the quadrature amplitudes, $\mathrm{Var}(X_1)+\mathrm{Var}(X_2)$, subtracted from the variance of measured vacuum indicates the amount of noise added during signal generation and mode conversion, which we find to be 0.92 ± 0.07 quanta. **b**, X_1 marginal of the quadrature amplitudes with Gaussian fits (black curves). **c**, For frequency shifts less than 90 MHz, we observe less added noise. Error bars, s.e.m. Dashed gray line indicates expected added noise from a mechanical decoherence rate of $n_{\mathrm{th}}\kappa_{\mathrm{m}} = 2\pi \times 900$ Hz.

4.7 Future work

We have demonstrated a temporal and spectral mode converter whose operating frequency, bandwidth, and low noise properties make it compatible with many circuit QED systems. As a next step, our mode converter could be integrated with a single circuit QED system consisting of a superconducting qubit embedded in a high-Q microwave resonator. This could enable the preparation of non-classical states of motion of a macroscopic mechanical oscillator. For example, circuit QED has been used to generate many-photon Schrodinger cat states of the electromagnetic

field [196]. By releasing these quantum signals into a transmission line and then capturing them as vibrations of the mechanical oscillator, we could in principle prepare the mechanical oscillator in a displacement superposition. This superposition could be used to probe the intersection of gravity and quantum mechanics [27], one of the original motivations of cavity optomechanics.

From an experimental point of view, even if non-classical states of motion can be prepared, they must also be detected. Measuring the position of a mechanical oscillator with sensitivity great enough to detect non-classical motion is an outstanding challenge for the field of cavity optomechanics [197, 198, 199, 167]. A related approach to measuring the motion of a mechanical oscillator amplifies motion via parametrically pumping the oscillator's resonant frequency [200, 201]. This latter approach can be implemented with our mode converter by utilizing the actuation electrode. This offers a potential route to nearly noiseless, phase-sensitive detection that is capable of detecting nonclassical motion.

Although the temporal and spectral mode converter functions well and adds less than one quanta of noise to the converted signal, the mechanical decoherence rate limits the added noise to $\gtrsim$0.4 quanta, as shown in Fig. 4.16b. A mode converter that utilizes membranes with higher quality factor vibrational modes could thus reduce added noise. In particular, vibrational modes of silicon nitride membranes have quality factors well in excess of those used here. Silicon nitride membranes have already been integrated with superconducting microwave circuits [148, 202]. These construction techniques, combined with advances in both understanding and fabricating silicon nitride membranes [65, 146, 145], could enable mode converters with greatly improved performance.

Chapter 5

Prosepects for quantum networking with mechanical oscillators

The microwave-to-optical frequency conversion demonstrated in Chapter 3 and the arbitrary temporal and spectral mode conversion presented in Chapter 4 together offer a route to overcome many of the signal processing challenges inherent in quantum information networks. However, the signal manipulation presented here utilizes low-amplitude classical signals. A next task is to combine macroscopic mechanical oscillators into networks that manipulate quantum signals. As suggested in section 4.7, a simple quantum network could be formed from a circuit QED system and our temporal and spectral mode converter. Such a network could be used to generate nonclassical states of macroscopic motion, but also confirm that mechanical oscillators can process quantum electromagnetic signals.

For a cavity optomechanical system to manipulate quantum signals with high fidelity, it must add much less than 1/2 quantum of noise to the signals [195]. Although the temporal and spectral mode converter can add approximately 0.4 quanta of noise, for high-fidelity manipulation both the mode converter and the microwave-to-optical frequency converter must operate deep in the quantum-enabled regime with $\Gamma \gg n_{\mathrm{m}}\kappa_{\mathrm{m}}$. Key to reaching deeper into this limit is the use of high-Q mechanical oscillators, as well as boosting Γ. However, for the type of signal processing presented here, there is a strict frequency hierarchy: $2\Gamma < \kappa \ll 4\omega_{\mathrm{m}}$, as set by the weak-coupling and resolved-sideband requirements introduced in section 2.4. High bandwidth manipulation of propagating electromagnetic signals thus requires a large ω_{m}. By utilizing recent advances in microfabrication and understanding of membrane mechanical oscillators, we hope to combine elec-

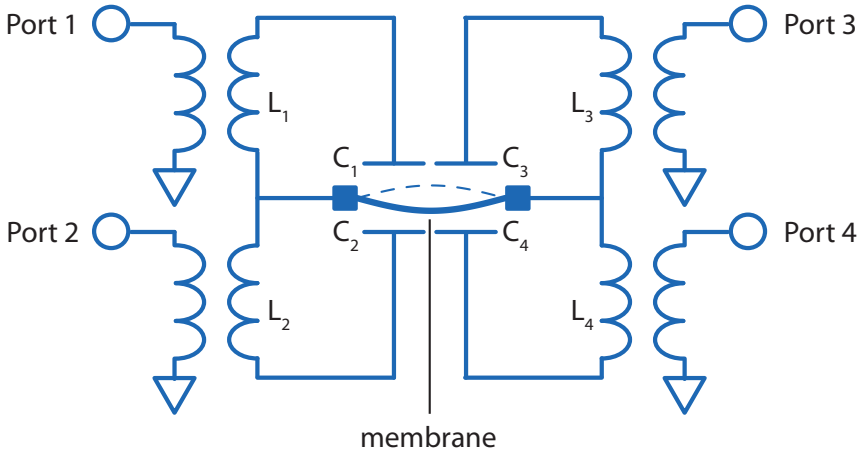

Figure 5.1: Electromagnetic signal router based on a mechanical oscillator. The radiation pressure interaction can be used to route quantum signals. For example, a signal entering through port 1 could be captured as a vibration of the mechanical oscillator and then released out any of the four ports.

tromagnetic resonators and mechanical oscillators that have $Q > 10^7$ and $\omega_{\rm m} > 2\pi \times 20$ MHz. These systems could bring truly quantum and useful capabilities to electromagnetic signal processing.

If mechanical oscillators can be used successfully in small quantum networks, their signal processing capabilities can be expanded to be relevant to larger and more complex networks. For example, large networks need devices that can route quantum signals between many different locations and components [203, 204]. An optomechanical router can potentially be created by combining a mechanical oscillator with multiple electromagnetic resonators. A sketch of such a routing circuit is shown in Fig. 5.1. The flexibility of microfabricated circuits and the radiation pressure interaction may allow optomechanical systems to play a key role in the development of quantum information networks.

5.1 Conclusion

The radiation pressure interaction between light and a mechanical oscillator provides a general method for manipulating quantum electromagnetic signals. The microwave-to-optical frequency

conversion of Chapter 3 demonstrates the broadband nature of the interaction, and the temporal and spectral mode conversion of Chapter 4 highlights the time-domain control available with the radiation pressure interaction. Next steps include integrating cavity optomechanical systems into small quantum networks, and extending their signal processing capabilities to include amplification and routing. Given recent progress in cavity optomechanics, I think mechanical oscillators will have a place in future quantum information networks.

Bibliography

[1] J. Kepler, Tychonis Brahei Dani Hyperaspistes. Frankfurt: Apud G. Tampachium, 1625. [Online]. Available: https://archive.org/details/tychonisbraheida00kepl

[2] C. Hellman, "Kepler and comets," Vistas in Astronomy, vol. 18, pp. 789–796, 1975. [Online]. Available: http://www.sciencedirect.com/science/article/pii/0083665675901695

[3] M. de Mairan, Traite physique et historique de l'aurore boreale. Paris: Imprimerie Royale, 1625. [Online]. Available: http://gallica.bnf.fr/ark:/12148/bpt6k3586v

[4] W. Crookes, "On attraction and repulsion resulting from radiation," Philosophical Transactions of the Royal Society of London, vol. 164, pp. 501–527, 1874. [Online]. Available: http://rstl.royalsocietypublishing.org/content/164/501.short

[5] J. C. Maxwell, A Treatise on Electricity and Magnetism. Clarendon Press, 1873, vol. 1.

[6] P. Lebedew, "Untersuchungen uber die druckkrafte des lichtes," Annalen der Physik, vol. 311, no. 11, pp. 433–458, 1901. [Online]. Available: http://dx.doi.org/10.1002/andp.19013111102

[7] E. F. Nichols and G. F. Hull, "A preliminary communication on the pressure of heat and light radiation," Phys. Rev. (Series I), vol. 13, pp. 307–320, Nov 1901. [Online]. Available: http://link.aps.org/doi/10.1103/PhysRevSeriesI.13.307

[8] ——, "The pressure due to radiation. (second paper.)," Phys. Rev. (Series I), vol. 17, pp. 26–50, Jul 1903. [Online]. Available: http://link.aps.org/doi/10.1103/PhysRevSeriesI.17.26

[9] ——, "The pressure due to radiation. (second paper.)," Phys. Rev. (Series I), vol. 17, pp. 91–104, Aug 1903. [Online]. Available: http://link.aps.org/doi/10.1103/PhysRevSeriesI.17.91

[10] A. Ashkin, "Acceleration and trapping of particles by radiation pressure," Phys. Rev. Lett., vol. 24, pp. 156–159, Jan 1970. [Online]. Available: http://link.aps.org/doi/10.1103/PhysRevLett.24.156

[11] T. Hansch and A. Schawlow, "Cooling of gases by laser radiation," Optics Communications, vol. 13, no. 1, pp. 68–69, 1975. [Online]. Available: http://www.sciencedirect.com/science/article/pii/0030401875901595

[12] A. Ashkin, "Trapping of atoms by resonance radiation pressure," Phys. Rev. Lett., vol. 40, pp. 729–732, Mar 1978. [Online]. Available: http://link.aps.org/doi/10.1103/PhysRevLett.40.729

[13] D. J. Wineland, R. E. Drullinger, and F. L. Walls, "Radiation-pressure cooling of bound resonant absorbers," Phys. Rev. Lett., vol. 40, pp. 1639–1642, Jun 1978. [Online]. Available: http://link.aps.org/doi/10.1103/PhysRevLett.40.1639

[14] S. Stenholm, "The semiclassical theory of laser cooling," Rev. Mod. Phys., vol. 58, pp. 699–739, Jul 1986. [Online]. Available: http://link.aps.org/doi/10.1103/RevModPhys.58.699

[15] V. Braginsky and V. Rudenko, "Gravitational waves and the detection of gravitational radiation," Physics Reports, vol. 46, no. 5, pp. 165–200, 1978. [Online]. Available: http://www.sciencedirect.com/science/article/pii/0370157378901928

[16] R. L. Forward, "Wideband laser-interferometer gravitational-radiation experiment," Phys. Rev. D, vol. 17, pp. 379–390, Jan 1978. [Online]. Available: http://link.aps.org/doi/10.1103/PhysRevD.17.379

[17] V. B. Braginsky and Y. I. Vorontsov, "Quantum-mechanical limitations in macroscopic experiments and modern experimental technique," Soviet Physics Uspekhi, vol. 17, no. 5, p. 644, 1975. [Online]. Available: http://stacks.iop.org/0038-5670/17/i=5/a=R02

[18] C. M. Caves, "Quantum-mechanical radiation-pressure fluctuations in an interferometer," Phys. Rev. Lett., vol. 45, pp. 75–79, Jul 1980. [Online]. Available: http://link.aps.org/doi/10.1103/PhysRevLett.45.75

[19] V. B. Braginsky and F. Y. Khalili, Quantum measurement. Cambridge: Cambridge University Press, 1992.

[20] V. Braginsky, A. B. Manukin, and M. Y. Tikhonov, "Investigation of dissipative ponderomotive effects of electromagnetic radiation," Journal of Experimental and Theoretical Physics, vol. 31, no. 5, p. 829, 1970.

[21] J. D. Teufel, T. Donner, M. A. Castellanos-Beltran, J. W. Harlow, and K. W. Lehnert, "Nanomechanical motion measured with an imprecision below that at the standard quantum limit," Nature Nanotechnology, vol. 4, pp. 820–823, Nov 2009. [Online]. Available: http://dx.doi.org/doi:10.1038/nnano.2009.343

[22] E. Gavartin, P. Verlot, and T. Kippenberg, "A hybrid on-chip optomechanical transducer for ultrasensitive force measurements," Nature nanotechnology, vol. 7, no. 8, pp. 509–514, 2012. [Online]. Available: http://dx.doi.org/doi:10.1038/nnano.2012.97

[23] M. Aspelmeyer, T. J. Kippenberg, and F. Marquardt, "Cavity optomechanics," Rev. Mod. Phys., vol. 86, pp. 1391–1452, Dec 2014. [Online]. Available: http://link.aps.org/doi/10.1103/RevModPhys.86.1391

[24] M. Metcalfe, "Applications of cavity optomechanics," Applied Physics Reviews, vol. 1, no. 3, pp. –, 2014. [Online]. Available: http://scitation.aip.org/content/aip/journal/apr2/1/3/10.1063/1.4896029

[25] S. Mancini, V. I. Man'ko, and P. Tombesi, "Ponderomotive control of quantum macroscopic coherence," Phys. Rev. A, vol. 55, pp. 3042–3050, Apr 1997. [Online]. Available: http://link.aps.org/doi/10.1103/PhysRevA.55.3042

[26] S. Bose, K. Jacobs, and P. L. Knight, "Preparation of nonclassical states in cavities with a moving mirror," Phys. Rev. A, vol. 56, pp. 4175–4186, Nov 1997. [Online]. Available: http://link.aps.org/doi/10.1103/PhysRevA.56.4175

[27] W. Marshall, C. Simon, R. Penrose, and D. Bouwmeester, "Towards quantum superpositions of a mirror," Phys. Rev. Lett., vol. 91, p. 130401, Sep 2003. [Online]. Available: http://link.aps.org/doi/10.1103/PhysRevLett.91.130401

[28] I. Pikovski, M. R. Vanner, M. Aspelmeyer, M. Kim, and Č. Brukner, "Probing Planck-scale physics with quantum optics," Nature Physics, vol. 8, no. 5, pp. 393–397, 2012. [Online]. Available: http://dx.doi.org/doi:10.1038/nphys2262

[29] A. Schliesser, P. Del'Haye, N. Nooshi, K. J. Vahala, and T. J. Kippenberg, "Radiation pressure cooling of a micromechanical oscillator using dynamical backaction," Phys. Rev. Lett., vol. 97, p. 243905, Dec 2006. [Online]. Available: http://link.aps.org/doi/10.1103/PhysRevLett.97.243905

[30] S. Gigan, H. R. Bohm, M. Paternostro, F. Blaser, G. Langer, J. B. Hertzberg, K. C. Schwab, D. Bauerle, M. Aspelmeyer, and A. Zeilinger, "Self-cooling of a micromirror by radiation pressure," Nature, vol. 444, no. 7115, pp. 67–70, 2006. [Online]. Available: http://dx.doi.org/10.1038/nature05273

[31] O. Arcizet, P.-F. Cohadon, T. Briant, M. Pinard, and A. Heidmann, "Radiation-pressure cooling and optomechanical instability of a micromirror," Nature, vol. 444, no. 7115, pp. 71–74, 2006. [Online]. Available: http://dx.doi.org/doi:10.1038/nature05244

[32] J. D. Teufel, J. W. Harlow, C. A. Regal, and K. W. Lehnert, "Dynamical backaction of microwave fields on a nanomechanical oscillator," Phys. Rev. Lett., vol. 101, p. 197203, Nov 2008. [Online]. Available: http://link.aps.org/doi/10.1103/PhysRevLett.101.197203

[33] F. Marquardt, J. P. Chen, A. A. Clerk, and S. M. Girvin, "Quantum theory of cavity-assisted sideband cooling of mechanical motion," Phys. Rev. Lett., vol. 99, no. 9, p. 093902, Aug 2007. [Online]. Available: http://dx.doi.org/doi:10.1103/PhysRevLett.99.093902

[34] I. Wilson-Rae, N. Nooshi, W. Zwerger, and T. J. Kippenberg, "Theory of ground state cooling of a mechanical oscillator using dynamical backaction," Phys. Rev. Lett., vol. 99, p. 093901, Aug 2007. [Online]. Available: http://link.aps.org/doi/10.1103/PhysRevLett.99.093901

[35] T. Rocheleau, T. Ndukum, C. Macklin, J. B. Hertzberg, A. A. Clerk, and K. C. Schwab, "Preparation and detection of a mechanical resonator near the ground state of motion," Nature, vol. 463, pp. 72–75, Jan 2010. [Online]. Available: http://dx.doi.org/doi:10.1038/nature08681

[36] J. D. Teufel, T. Donner, D. Li, J. W. Harlow, M. S. Allman, K. Cicak, A. J. Sirois, J. D. Whittaker, K. W. Lehnert, and R. W. Simmonds, "Sideband cooling of micromechanical motion to the quantum ground state," Nature, vol. 475, no. 7356, pp. 359–363, 2011. [Online]. Available: http://dx.doi.org/10.1038/nature10261

[37] J. Chan, T. P. M. Alegre, A. H. Safavi-Naeini, J. T. Hill, A. Krause, S. Groblacher, M. Aspelmeyer, and O. Painter, "Laser cooling of a nanomechanical oscillator into its quantum ground state," Nature, vol. 478, no. 7367, pp. 89–92, 2011. [Online]. Available: http://dx.doi.org/10.1038/nature10461

[38] P. Rabl, "Photon blockade effect in optomechanical systems," Phys. Rev. Lett., vol. 107, p. 063601, Aug 2011. [Online]. Available: http://link.aps.org/doi/10.1103/PhysRevLett.107.063601

[39] A. Nunnenkamp, K. Børkje, and S. M. Girvin, "Single-photon optomechanics," Phys. Rev. Lett., vol. 107, p. 063602, Aug 2011. [Online]. Available: http://link.aps.org/doi/10.1103/PhysRevLett.107.063602

[40] L. A. D. Lorenzo and K. C. Schwab, "Superfluid optomechanics: coupling of a superfluid to a superconducting condensate," New Journal of Physics, vol. 16, no. 11, p. 113020, 2014. [Online]. Available: http://stacks.iop.org/1367-2630/16/i=11/a=113020

[41] H. J. Kimble, "The quantum internet," Nature, vol. 453, no. 7198, pp. 1023–1030, 2008. [Online]. Available: http://dx.doi.org/10.1038/nature07127

[42] A. K. Ekert, "Quantum cryptography based on Bell's theorem," Phys. Rev. Lett., vol. 67, pp. 661–663, Aug 1991. [Online]. Available: http://link.aps.org/doi/10.1103/PhysRevLett.67.661

[43] H.-K. Lo and H. F. Chau, "Unconditional security of quantum key distribution over arbitrarily long distances," Science, vol. 283, no. 5410, pp. 2050–2056, 1999. [Online]. Available: http://www.sciencemag.org/content/283/5410/2050.abstract

[44] C. Bennett, P. Shor, J. Smolin, and A. Thapliyal, "Entanglement-assisted capacity of a quantum channel and the reverse Shannon theorem," IEEE Transactions on Information Theory, vol. 48, no. 10, pp. 2637–2655, Oct 2002. [Online]. Available: http://dx.doi.org/doi:10.1109/TIT.2002.802612

[45] I. Buluta, S. Ashhab, and F. Nori, "Natural and artificial atoms for quantum computation," Reports on Progress in Physics, vol. 74, no. 10, p. 104401, 2011. [Online]. Available: http://stacks.iop.org/0034-4885/74/i=10/a=104401

[46] J. L. O'Brien, A. Furusawa, and J. Vuckovic, "Photonic quantum technologies," Nature Photonics, vol. 3, pp. 687–695, 2009. [Online]. Available: http://dx.doi.org/doi:10.1038/nphoton.2009.229

[47] J. I. Cirac, P. Zoller, H. J. Kimble, and H. Mabuchi, "Quantum state transfer and entanglement distribution among distant nodes in a quantum network," Phys. Rev. Lett., vol. 78, pp. 3221–3224, Apr 1997. [Online]. Available: http://link.aps.org/doi/10.1103/PhysRevLett.78.3221

[48] M. W. McCutcheon, D. E. Chang, Y. Zhang, M. D. Lukin, and M. Loncar, "Broadband frequency conversion and shaping of single photons emitted from a nonlinear cavity," Opt. Express, vol. 17, no. 25, pp. 22 689–22 703, Dec 2009. [Online]. Available: http://www.opticsexpress.org/abstract.cfm?URI=oe-17-25-22689

[49] S. J. van Enk, J. I. Cirac, and P. Zoller, "Photonic channels for quantum communication," Science, vol. 279, no. 5348, pp. 205–208, 1998. [Online]. Available: http://www.sciencemag.org/content/279/5348/205.abstract

[50] K. Stannigel, P. Rabl, A. S. Sørensen, P. Zoller, and M. D. Lukin, "Optomechanical transducers for long-distance quantum communication," Phys. Rev. Lett., vol. 105, p. 220501, Nov 2010. [Online]. Available: http://link.aps.org/doi/10.1103/PhysRevLett.105.220501

[51] P. Rabl, S. J. Kolkowitz, F. H. L. Koppens, J. G. E. Harris, P. Zoller, and M. D. Lukin, "A quantum spin transducer based on nanoelectromechanical resonator arrays," Nature Physics, vol. 6, no. 8, pp. 602–608, 2010. [Online]. Available: http://dx.doi.org/doi:10.1038/nphys1679

[52] A. H. Safavi-Naeini and O. Painter, "Proposal for an optomechanical traveling wave phononphoton translator," New Journal of Physics, vol. 13, no. 1, p. 013017, 2011. [Online]. Available: http://stacks.iop.org/1367-2630/13/i=1/a=013017

[53] A. H. Safavi-Naeini, T. P. M. Alegre, J. Chan, M. Eichenfield, M. Winger, Q. Lin, J. T. Hill, D. E. Chang, and O. Painter, "Electromagnetically induced transparency and slow light with optomechanics," Nature, vol. 472, no. 7341, pp. 69–73, 2011. [Online]. Available: http://dx.doi.org/doi:10.1038/nature09933

[54] S. Weis, R. Rivière, S. Deléglise, E. Gavartin, O. Arcizet, A. Schliesser, and T. J. Kippenberg, "Optomechanically induced transpency," Science, vol. 330, pp. 1520–1523, November 2010. [Online]. Available: http://dx.doi.org/doi:10.1126/science.1195596

[55] J. D. Teufel, D. Li, M. S. Allman, K. Cicak, A. J. Sirois, J. D. Whittaker, and R. W. Simmonds, "Circuit cavity electromechanics in the strong-coupling regime," Nature, vol. 471, no. 7337, pp. 204–208, 2011. [Online]. Available: http://dx.doi.org/10.1038/nature09898

[56] X. Zhou, F. Hocke, A. Schliesser, A. Marx, H. Huebl, R. Gross, and T. Kippenberg, "Slowing, advancing and switching of microwave signals using circuit nanoelectromechanics," Nature Physics, vol. 9, no. 3, pp. 179–184, 2013. [Online]. Available: http://dx.doi.org/doi:10.1038/nphys2527

[57] V. Fiore, Y. Yang, M. C. Kuzyk, R. Barbour, L. Tian, and H. Wang, "Storing optical information as a mechanical excitation in a silica optomechanical resonator," Phys. Rev. Lett., vol. 107, p. 133601, Sep 2011. [Online]. Available: http://link.aps.org/doi/10.1103/PhysRevLett.107.133601

[58] T. A. Palomaki, J. W. Harlow, J. D. Teufel, R. W. Simmonds, and K. W. Lehnert, "Coherent state transfer between itinerant microwave fields and a mechanical oscillator," Nature, vol. 495, no. 7440, pp. 210–214, 2013. [Online]. Available: http://dx.doi.org/10.1038/nature11915

[59] E. Verhagen, S. Deleglise, S. Weis, A. Schliesser, and T. J. Kippenberg, "Quantum-coherent coupling of a mechanical oscillator to an optical cavity mode," Nature, vol. 482, no. 7383, pp. 63–67, 2012. [Online]. Available: http://dx.doi.org/10.1038/nature10787

[60] J. T. Hill, A. H. Safavi-Naeini, J. Chan, and O. Painter, "Coherent optical wavelength conversion via cavity optomechanics," Nature Communications, vol. 3, p. 1196, 2012. [Online]. Available: http://dx.doi.org/10.1038/ncomms2201

[61] C. Dong, V. Fiore, M. C. Kuzyk, and H. Wang, "Optomechanical dark mode," Science, vol. 338, no. 6114, pp. 1609–1613, 2012. [Online]. Available: http://www.sciencemag.org/content/338/6114/1609.abstract

[62] Y. Liu, M. Davanço, V. Aksyuk, and K. Srinivasan, "Electromagnetically induced transparency and wideband wavelength conversion in silicon nitride microdisk optomechanical resonators," Phys. Rev. Lett., vol. 110, p. 223603, May 2013. [Online]. Available: http://link.aps.org/doi/10.1103/PhysRevLett.110.223603

[63] S. Timoshenko, D. H. Young, and W. Weaver, Vibrational Problems in Engineering. New York: John Wiley and Sons, 1974.

[64] A. W. Leissa, "Vibration of plates," DTIC Document, Tech. Rep., 1969.

[65] P.-L. Yu, T. P. Purdy, and C. A. Regal, "Control of material damping in high-Q membrane microresonators," Phys. Rev. Lett., vol. 108, p. 083603, Feb 2012. [Online]. Available: http://link.aps.org/doi/10.1103/PhysRevLett.108.083603

[66] S. Schmid, K. D. Jensen, K. H. Nielsen, and A. Boisen, "Damping mechanisms in high-Q micro and nanomechanical string resonators," Phys. Rev. B, vol. 84, p. 165307, Oct 2011. [Online]. Available: http://link.aps.org/doi/10.1103/PhysRevB.84.165307

[67] M. Eichenfield, "Cavity optomechanics in photonic and phononic crystals: engineering the interaction of light and sound at the nanoscale," Ph.D. dissertation, Caltech, 2010.

[68] D. J. Wilson, "Cavity optomechanics with high-stress silicon nitride films," Ph.D. dissertation, Caltech, 2012.

[69] Q. P. Unterreithmeier, T. Faust, and J. P. Kotthaus, "Damping of nanomechanical resonators," Phys. Rev. Lett., vol. 105, p. 027205, Jul 2010. [Online]. Available: http://link.aps.org/doi/10.1103/PhysRevLett.105.027205

[70] D. M. Pozar, Microwave Engineering, 2nd ed. New York: John Wiley and Sons, 1998.

[71] A. N. Cleland, Foundations of Nanomechanics. Berlin: Springer, 2003.

[72] C. A. Regal, J. D. Teufel, and K. W. Lehnert, "Measuring nanomechanical motion with a microwave cavity interferometer," Nature Physics, vol. 4, pp. 555–560, May 2008. [Online]. Available: http://dx.doi.org/doi:10.1038/nphys974

[73] I. Wilson-Rae, R. A. Barton, S. S. Verbridge, D. R. Southworth, B. Ilic, H. G. Craighead, and J. M. Parpia, "High-Q nanomechanics via destructive interference of elastic waves," Phys. Rev. Lett., vol. 106, p. 047205, Jan 2011. [Online]. Available: http://link.aps.org/doi/10.1103/PhysRevLett.106.047205

[74] T. P. Purdy, R. W. Peterson, P.-L. Yu, and C. A. Regal, "Cavity optomechanics with Si_3N_4 membranes at cryogenic temperatures," New Journal of Physics, vol. 14, no. 11, p. 115021, 2012. [Online]. Available: http://stacks.iop.org/1367-2630/14/i=11/a=115021

[75] A. E. Siegman, Lasers. Sausalito: University Science Books, 1986.

[76] S. Kuhr, S. Gleyzes, C. Guerlin, J. Bernu, U. B. Hoff, S. Delglise, S. Osnaghi, M. Brune, J.-M. Raimond, S. Haroche, E. Jacques, P. Bosland, and B. Visentin, "Ultrahigh finesse Fabry-Perot superconducting resonator," Applied Physics Letters, vol. 90, no. 16, pp. –, 2007. [Online]. Available: http://scitation.aip.org/content/aip/journal/apl/90/16/10.1063/1.2724816

[77] R. G. Rogers, Low Phase Noise Microwave Oscillator Design. Boston: Artech House, 1991.

[78] P. K. Day, H. G. LeDuc, B. A. Mazin, A. Vayonakis, and J. Zmuidzinas, "A broadband superconducting detector suitable for use in large arrays," Nature, vol. 425, no. 6960, pp. 817–821, 2003. [Online]. Available: http://dx.doi.org/doi:10.1038/nature02037

[79] S. Doyle, "Lumped element kinetic inductance detectors," Ph.D. dissertation, Cardiff University, 2008.

[80] H. A. Haus, Waves and Fields in Optoelectronics. New Jersey: Prentice-Hall, 1984.

[81] J. Gao, M. Daal, A. Vayonakis, S. Kumar, J. Zmuidzinas, B. Sadoulet, B. A. Mazin, P. K. Day, and H. G. Leduc, "Experimental evidence for a surface distribution of two-level systems in superconducting lithographed microwave resonators," Applied Physics Letters, vol. 92, no. 15, pp. –, 2008. [Online]. Available: http://scitation.aip.org/content/aip/journal/apl/92/15/10.1063/1.2906373

[82] H. Wang, M. Hofheinz, J. Wenner, M. Ansmann, R. C. Bialczak, M. Lenander, E. Lucero, M. Neeley, A. D. O'Connell, D. Sank, M. Weides, A. N. Cleland, and J. M. Martinis, "Improving the coherence time of superconducting coplanar resonators," Applied Physics Letters, vol. 95, no. 23, pp. –, 2009. [Online]. Available: http://scitation.aip.org/content/aip/journal/apl/95/23/10.1063/1.3273372

[83] D. F. Walls and G. J. Milburn, Quantum Optics, 2nd ed. Berlin: Springer-Verlag, 2008.

[84] A. Schliesser, R. Riviére, G. Anetsberger, O. Arcizet, and T. J. Kippenberg, "Resolved-sideband cooling of a micromechanical oscillator," Nature Physics, vol. 4, pp. 415–419, Apr 2008. [Online]. Available: http://dx.doi.org/doi:10.1038/nphys939

[85] T. J. Kippenberg and K. J. Vahala, "Cavity optomechanics: Back-action at the mesoscale," Science, vol. 321, no. 5893, pp. 1172–1176, 2008. [Online]. Available: http://www.sciencemag.org/content/321/5893/1172.abstract

[86] T. P. Purdy, R. W. Peterson, and C. A. Regal, "Observation of radiation pressure shot noise on a macroscopic object," Science, vol. 339, no. 6121, pp. 801–804, 2013. [Online]. Available: http://www.sciencemag.org/content/339/6121/801.abstract

[87] C. Fabre, M. Pinard, S. Bourzeix, A. Heidmann, E. Giacobino, and S. Reynaud, "Quantum-noise reduction using a cavity with a movable mirror," Phys. Rev. A, vol. 49, pp. 1337–1343, Feb 1994. [Online]. Available: http://link.aps.org/doi/10.1103/PhysRevA.49.1337

[88] A. Dorsel, J. D. McCullen, P. Meystre, E. Vignes, and H. Walther, "Optical bistability and mirror confinement induced by radiation pressure," Phys. Rev. Lett., vol. 51, pp. 1550–1553, Oct 1983. [Online]. Available: http://link.aps.org/doi/10.1103/PhysRevLett.51.1550

[89] C. K. Law, "Interaction between a moving mirror and radiation pressure: A Hamiltonian formulation," Phys. Rev. A, vol. 51, no. 3, pp. 2537–2541, Mar 1995. [Online]. Available: http://dx.doi.org/doi:10.1103/PhysRevA.51.2537

[90] S. A. McGee, D. Meiser, C. A. Regal, K. W. Lehnert, and M. J. Holland, "Mechanical resonators for storage and transfer of electrical and optical quantum states," Phys. Rev. A, vol. 87, p. 053818, May 2013. [Online]. Available: http://link.aps.org/doi/10.1103/PhysRevA.87.053818

[91] C.-T. Chen, Linear System Theory and Design, 3rd ed. New York: Oxford University Press, 1999.

[92] W. L. Brogan, Modern Control Theory, 3rd ed. New Jersey: Prentice-Hall, 1991.

[93] A. A. Clerk, M. H. Devoret, S. M. Girvin, F. Marquardt, and R. J. Schoelkopf, "Introduction to quantum noise, measurement, and amplification," Rev. Mod. Phys., vol. 82, no. 2, pp. 1155–1208, Apr 2010. [Online]. Available: http://dx.doi.org/doi:10.1103/RevModPhys.82.1155

[94] R. Loudon, The Quantum Theory of Light, 3rd ed. New York: Oxford University Press, 2000.

[95] C. Kittel and H. Kroemer, Thermal Physics, 2nd ed. W. H. Freeman and Company, 1980.

[96] F. Pobell, Matter and Methods at Low Temperatures, 2nd ed. Berlin: Springer-Verlag, 1996.

[97] A. D. O'Connell, M. Hofheinz, M. Ansmann, R. C. Bialczak, M. Lenander, E. Lucero, M. Neeley, D. Sank, H. Wang, M. Weides, J. Wenner, J. M. Martinis, and A. N. Cleland, "Quantum ground state and single-phonon control of a mechanical resonator," Nature, vol. 464, no. 7289, pp. 697–703, 2010. [Online]. Available: http://dx.doi.org/10.1038/nature08967

[98] M. Eichenfield, J. Chan, R. M. Camacho, K. J. Vahala, and O. Painter, "Optomechanical crystals," Nature, vol. 462, no. 7269, pp. 78–82, 2009. [Online]. Available: http://dx.doi.org/doi:10.1038/nature08524

[99] J. Bochmann, A. Vainsencher, D. D. Awschalom, and A. N. Cleland, "Nanomechanical coupling between microwave and optical photons," Nature Physics, vol. 9, pp. 712–716, 2013. [Online]. Available: http://dx.doi.org/10.1038/nphys2748

[100] T. Miya, Y. Terunuma, T. Hosaka, and T. Miyashita, "Ultimate low-loss single-mode fibre at 1.55 μm," Electronics Letters, vol. 15, no. 4, pp. 106–108, February 1979. [Online]. Available: http://dx.doi.org/10.1049/el:19790077

[101] J. Kilby, "Invention of the integrated circuit," IEEE Transactions on Electron Devices, vol. 23, no. 7, pp. 648–654, Jul 1976. [Online]. Available: http://dx.doi.org/doi:10.1109/T-ED.1976.18467

[102] J. Clarke and F. K. Wilhelm, "Superconducting quantum bits," Nature, vol. 453, no. 7198, pp. 1031–1042, 2008. [Online]. Available: http://dx.doi.org/10.1038/nature07128

[103] R. J. Schoelkopf and S. M. Girvin, "Wiring up quantum systems," Nature, vol. 451, no. 7179, pp. 664–669, 2008. [Online]. Available: http://dx.doi.org/10.1038/451664a

[104] M. H. Devoret and R. J. Schoelkopf, "Superconducting circuits for quantum information: An outlook," Science, vol. 339, no. 6124, pp. 1169–1174, 2013. [Online]. Available: http://www.sciencemag.org/content/339/6124/1169.abstract

[105] C. Langer, R. Ozeri, J. D. Jost, J. Chiaverini, B. DeMarco, A. Ben-Kish, R. B. Blakestad, J. Britton, D. B. Hume, W. M. Itano, D. Leibfried, R. Reichle, T. Rosenband, T. Schaetz, P. O. Schmidt, and D. J. Wineland, "Long-lived qubit memory using atomic ions," Phys. Rev. Lett., vol. 95, p. 060502, Aug 2005. [Online]. Available: http://link.aps.org/doi/10.1103/PhysRevLett.95.060502

[106] M. Zhong, M. P. Hedges, R. L. Ahlefeldt, J. G. Bartholomew, S. E. Beavan, S. M. Wittig, J. J. Longdell, and M. J. Sellars, "Optically addressable nuclear spins in a solid with a six-hour coherence time," Nature, vol. 517, no. 7533, pp. 177–180, 2015. [Online]. Available: http://dx.doi.org/doi:10.1038/nature14025

[107] S. Ritter, C. Nolleke, C. Hahn, A. Reiserer, A. Neuzner, M. Uphoff, M. Mucke, E. Figueroa, J. Bochmann, and G. Rempe, "An elementary quantum network of single atoms in optical cavities," Nature, vol. 484, no. 7393, pp. 195–200, 2012. [Online]. Available: http://dx.doi.org/10.1038/nature11023

[108] M. D. Reed, L. DiCarlo, S. E. Nigg, L. Sun, L. Frunzio, S. M. Girvin, and R. J. Schoelkopf, "Realization of three-qubit quantum error correction with superconducting circuits," Nature, vol. 482, no. 7385, pp. 382–385, 2012. [Online]. Available: http://dx.doi.org/10.1038/nature10786

[109] E. Lucero, R. Barends, Y. Chen, J. Kelly, M. Mariantoni, A. Megrant, P. O'Malley, D. Sank, A. Vainsencher, J. Wenner, T. White, Y. Yin, A. N. Cleland, and J. M. Martinis, "Computing prime factors with a Josephson phase qubit quantum processor," Nature Physics, vol. 8, no. 10, pp. 719–723, 2012. [Online]. Available: http://dx.doi.org/10.1038/nphys2385

[110] T. D. Ladd, F. Jelezko, R. Laflamme, Y. Nakamura, C. Monroe, and J. L. O'Brien, "Quantum computers," Nature, vol. 464, no. 7285, pp. 45–53, 2010. [Online]. Available: http://dx.doi.org/10.1038/nature08812

[111] M. Tsang, "Cavity quantum electro-optics," Phys. Rev. A, vol. 81, p. 063837, Jun 2010. [Online]. Available: http://link.aps.org/doi/10.1103/PhysRevA.81.063837

[112] ——, "Cavity quantum electro-optics. II. input-output relations between traveling optical and microwave fields," Phys. Rev. A, vol. 84, p. 043845, Oct 2011. [Online]. Available: http://link.aps.org/doi/10.1103/PhysRevA.84.043845

[113] D. Cohen, M. Hossein-Zadeh, and A. F. J. Levi, "Microphotonic modulator for microwave receiver," Electronics Letters, vol. 37, no. 5, pp. 300–301, 2001. [Online]. Available: http://dx.doi.org/doi:10.1049/el:20010220

[114] V. S. Ilchenko, A. A. Savchenkov, A. B. Matsko, and L. Maleki, "Whispering-gallery-mode electro-optic modulator and photonic microwave receiver," J. Opt. Soc. Am. B, vol. 20, no. 2, pp. 333–342, Feb 2003. [Online]. Available: http://josab.osa.org/abstract.cfm?URI=josab-20-2-333

[115] A. A. Savchenkov, W. Liang, A. B. Matsko, V. S. Ilchenko, D. Seidel, and L. Maleki, "Tunable optical single-sideband modulator with complete sideband suppression," Opt. Lett., vol. 34, no. 9, pp. 1300–1302, May 2009. [Online]. Available: http://ol.osa.org/abstract.cfm?URI=ol-34-9-1300

[116] M. Hafezi, Z. Kim, S. L. Rolston, L. A. Orozco, B. L. Lev, and J. M. Taylor, "Atomic interface between microwave and optical photons," Phys. Rev. A, vol. 85, p. 020302, Feb 2012. [Online]. Available: http://link.aps.org/doi/10.1103/PhysRevA.85.020302

[117] J. Verdú, H. Zoubi, C. Koller, J. Majer, H. Ritsch, and J. Schmiedmayer, "Strong magnetic coupling of an ultracold gas to a superconducting waveguide cavity," Phys. Rev. Lett., vol. 103, p. 043603, Jul 2009. [Online]. Available: http://link.aps.org/doi/10.1103/PhysRevLett.103.043603

[118] A. Imamoğlu, "Cavity QED based on collective magnetic dipole coupling: Spin ensembles as hybrid two-level systems," Phys. Rev. Lett., vol. 102, p. 083602, Feb 2009. [Online]. Available: http://link.aps.org/doi/10.1103/PhysRevLett.102.083602

[119] D. Marcos, M. Wubs, J. M. Taylor, R. Aguado, M. D. Lukin, and A. S. Sørensen, "Coupling nitrogen-vacancy centers in diamond to superconducting flux qubits," Phys. Rev. Lett., vol. 105, p. 210501, Nov 2010. [Online]. Available: http://link.aps.org/doi/10.1103/PhysRevLett.105.210501

[120] C. O'Brien, N. Lauk, S. Blum, G. Morigi, and M. Fleischhauer, "Interfacing superconducting qubits and telecom photons via a rare-earth-doped crystal," Phys. Rev. Lett., vol. 113, p. 063603, Aug 2014. [Online]. Available: http://link.aps.org/doi/10.1103/PhysRevLett.113.063603

[121] L. A. Williamson, Y.-H. Chen, and J. J. Longdell, "Magneto-optic modulator with unit quantum efficiency," Phys. Rev. Lett., vol. 113, p. 203601, Nov 2014. [Online]. Available: http://link.aps.org/doi/10.1103/PhysRevLett.113.203601

[122] C. A. Regal and K. W. Lehnert, "From cavity electromechanics to cavity optomechanics," Journal of Physics: Conference Series, vol. 264, no. 1, p. 012025, 2011. [Online]. Available: http://stacks.iop.org/1742-6596/264/i=1/a=012025

[123] M. Winger, T. D. Blasius, T. P. M. Alegre, A. H. Safavi-Naeini, S. Meenehan, J. Cohen, S. Stobbe, and O. Painter, "A chip-scale integrated cavity-electro-optomechanics platform," Opt. Express, vol. 19, no. 25, pp. 24 905–24 921, Dec 2011. [Online]. Available: http://www.opticsexpress.org/abstract.cfm?URI=oe-19-25-24905

[124] T. Bagci, A. Simonsen, S. Schmid, L. G. Villanueva, E. Zeuthen, J. Appel, J. M. Taylor, A. Sørensen, K. Usami, A. Schliesser et al., "Optical detection of radio waves through a nanomechanical transducer," Nature, vol. 507, no. 7490, pp. 81–85, 2014. [Online]. Available: htt[://dx.doi.org/doi:10.1038/nature13029

[125] A. Pitanti, J. M. Fink, A. H. Safavi-Naeini, J. T. Hill, C. U. Lei, A. Tredicucci, and O. Painter, "Strong opto-electro-mechanical coupling in a silicon photonic crystal cavity," Opt. Express, vol. 23, no. 3, pp. 3196–3208, Feb 2015. [Online]. Available: http://www.opticsexpress.org/abstract.cfm?URI=oe-23-3-3196

[126] A. Metelmann and A. A. Clerk, "Quantum-limited amplification via reservoir engineering," Phys. Rev. Lett., vol. 112, p. 133904, Apr 2014. [Online]. Available: http://link.aps.org/doi/10.1103/PhysRevLett.112.133904

[127] C. M. Caves, "Quantum limits on noise in linear amplifiers," Phys. Rev. D, vol. 26, pp. 1817–1839, Oct 1982. [Online]. Available: http://link.aps.org/doi/10.1103/PhysRevD.26.1817

[128] A. Gozzini, F. Maccarrone, F. Mango, I. Longo, and S. Barbarino, "Light-pressure bistability at microwave frequencies," J. Opt. Soc. Am. B, vol. 2, no. 11, pp. 1841–1845, Nov 1985. [Online]. Available: http://josab.osa.org/abstract.cfm?URI=josab-2-11-1841

[129] L. Tian and H. Wang, "Optical wavelength conversion of quantum states with optomechanics," Phys. Rev. A, vol. 82, p. 053806, Nov 2010. [Online]. Available: http://link.aps.org/doi/10.1103/PhysRevA.82.053806

[130] Y.-D. Wang and A. A. Clerk, "Using interference for high fidelity quantum state transfer in optomechanics," Phys. Rev. Lett., vol. 108, p. 153603, Apr 2012. [Online]. Available: http://link.aps.org/doi/10.1103/PhysRevLett.108.153603

[131] L. Tian, "Adiabatic state conversion and pulse transmission in optomechanical systems," Phys. Rev. Lett., vol. 108, p. 153604, Apr 2012. [Online]. Available: http://link.aps.org/doi/10.1103/PhysRevLett.108.153604

[132] S. Barzanjeh, M. Abdi, G. J. Milburn, P. Tombesi, and D. Vitali, "Reversible optical-to-microwave quantum interface," Phys. Rev. Lett., vol. 109, p. 130503, Sep 2012. [Online]. Available: http://link.aps.org/doi/10.1103/PhysRevLett.109.130503

[133] B. M. Zwickl, W. E. Shanks, A. M. Jayich, C. Yang, A. C. B. Jayich, J. D. Thompson, and J. G. E. Harris, "High quality mechanical and optical properties of commercial silicon nitride membranes," Applied Physics Letters, vol. 92, no. 10, p. 103125, 2008. [Online]. Available: http://link.aip.org/link/?APL/92/103125/1

[134] J. D. Thompson, B. M. Zwickl, A. M. Jayich, F. Marquardt, S. M. Girvin, and J. G. E. Harris, "Strong dispersive coupling of a high-finesse cavity to a micromechanical membrane," Nature, vol. 452, no. 7183, pp. 72–75, 2008. [Online]. Available: http://dx.doi.org/10.1038/nature06715

[135] D. J. Wilson, C. A. Regal, S. B. Papp, and H. J. Kimble, "Cavity optomechanics with stoichiometric SiN films," Phys. Rev. Lett., vol. 103, p. 207204, Nov 2009. [Online]. Available: http://link.aps.org/doi/10.1103/PhysRevLett.103.207204

[136] K. Cicak, D. Li, J. Stong, M. Allman, F. Altomare, A. Sirois, J. Whittaker, J. D. Teufel, and R. W. Simmonds, "Low-loss superconducting resonant circuits using vacuum-gap-based microwave components," Applied Physics Letters, vol. 96, p. 093502, Mar 2010. [Online]. Available: http://dx.doi.org/doi:10.1063/1.3304168

[137] R. Barends, J. Wenner, M. Lenander, Y. Chen, R. C. Bialczak, J. Kelly, E. Lucero, P. O'Malley, M. Mariantoni, D. Sank, H. Wang, T. C. White, Y. Yin, J. Zhao, A. N. Cleland, J. M. Martinis, and J. J. A. Baselmans, "Minimizing quasiparticle generation from stray infrared light in superconducting quantum circuits," Applied Physics Letters, vol. 99, no. 11, pp. –, 2011. [Online]. Available: http://scitation.aip.org/content/aip/journal/apl/99/11/10.1063/1.3638063

[138] J. Gao, J. Zmuidzinas, A. Vayonakis, P. Day, B. Mazin, and H. Leduc, "Equivalence of the effects on the complex conductivity of superconductor due to temperature change and external pair breaking," Journal of Low Temperature Physics, vol. 151, no. 1-2, pp. 557–563, 2008. [Online]. Available: http://dx.doi.org/10.1007/s10909-007-9688-z

[139] H. Lefevre, R. Schofield, and D. Ciarlo, "Thin Si_3N_4 windows for energy loss STIM in air," Nuclear Instruments and Methods in Physics Research Section B: Beam Interactions with Materials and Atoms, vol. 54, no. 13, pp. 47–51, 1991. [Online]. Available: http://www.sciencedirect.com/science/article/pii/0168583X9195489Z

[140] D. Ciarlo, "Silicon nitride thin windows for biomedical microdevices," Biomedical Microdevices, vol. 4, no. 1, pp. 63–68, 2002. [Online]. Available: http://dx.doi.org/10.1023/A%3A1014275913962

[141] "Dupont Pyralux AP flexible circuit materials," Tech. Rep. H73241-9, June 2012. [Online]. Available: http://www.dupont.com/content/dam/assets/products-and-services/electronic-electrical-materials/assets/PyraluxAPclad_DataSheet.pdf

[142] E. Guillaume, "Recherches surs les aciers au nickel. Dilatations aux temperatures elevees; resistance electrique." Comptes Rendus de l'Academie des Sciences, vol. 125, pp. 235–238, 1897. [Online]. Available: http://www.archive.org/details/ComptesRendusAcademieDesSciences0125

[143] P. Meystre, J. D. McCullen, E. Vignes, and E. M. Wright, "Theory of radiation-pressure-driven interferometers," J. Opt. Soc. Am. B, vol. 2, no. 11, pp. 1830–1840, Nov 1985. [Online]. Available: http://josab.osa.org/abstract.cfm?URI=josab-2-11-1830

[144] M. Maldovan, "Sound and heat revolutions in phononics," Nature, vol. 503, no. 7475, pp. 209–217, 2013. [Online]. Available: http://dx.doi.org/doi:10.1038/nature12608

[145] Y. Tsaturyan, A. Barg, A. Simonsen, L. G. Villanueva, S. Schmid, A. Schliesser, and E. S. Polzik, "Demonstration of suppressed phonon tunneling losses in phononic bandgap shielded membrane resonators for high-Q optomechanics," Opt. Express, vol. 22, no. 6, pp. 6810–6821, Mar 2014. [Online]. Available: http://www.opticsexpress.org/abstract.cfm?URI=oe-22-6-6810

[146] P.-L. Yu, K. Cicak, N. S. Kampel, Y. Tsaturyan, T. P. Purdy, R. W. Simmonds, and C. A. Regal, "A phononic bandgap shield for high-Q membrane microresonators," Applied Physics Letters, vol. 104, no. 2, pp. –, 2014. [Online]. Available: http://scitation.aip.org/content/aip/journal/apl/104/2/10.1063/1.4862031

[147] J. Zhang, K. Peng, and S. L. Braunstein, "Quantum-state transfer from light to macroscopic oscillators," Phys. Rev. A, vol. 68, p. 013808, Jul 2003. [Online]. Available: http://link.aps.org/doi/10.1103/PhysRevA.68.013808

[148] R. Andrews, R. Peterson, T. Purdy, K. Cicak, R. Simmonds, C. Regal, and K. Lehnert, "Bidirectional and efficient conversion between microwave and optical light," Nature Physics, vol. 10, pp. 321–324, 2014. [Online]. Available: http://dx.doi.org/doi:10.1038/nphys2911

[149] Y.-D. Wang and A. A. Clerk, "Reservoir-engineered entanglement in optomechanical systems," Phys. Rev. Lett., vol. 110, p. 253601, Jun 2013. [Online]. Available: http://link.aps.org/doi/10.1103/PhysRevLett.110.253601

[150] L. Tian, "Robust photon entanglement via quantum interference in optomechanical interfaces," Phys. Rev. Lett., vol. 110, p. 233602, Jun 2013. [Online]. Available: http://link.aps.org/doi/10.1103/PhysRevLett.110.233602

[151] M. C. Kuzyk, S. J. van Enk, and H. Wang, "Generating robust optical entanglement in weak-coupling optomechanical systems," Phys. Rev. A, vol. 88, p. 062341, Dec 2013. [Online]. Available: http://link.aps.org/doi/10.1103/PhysRevA.88.062341

[152] R. Miller, T. E. Northup, K. M. Birnbaum, A. Boca, A. D. Boozer, and H. J. Kimble, "Trapped atoms in cavity QED: coupling quantized light and matter," Journal of Physics B: Atomic, Molecular and Optical Physics, vol. 38, no. 9, p. S551, 2005. [Online]. Available: http://stacks.iop.org/0953-4075/38/i=9/a=007

[153] M. G. Raymer and K. Srinivasan, "Manipulating the color and shape of single photons," Physics Today, vol. 65, pp. 32–37, 2012. [Online]. Available: http://dx.doi.org/10.1063/PT.3.1786

[154] M. T. Rakher, L. Ma, M. Davanço, O. Slattery, X. Tang, and K. Srinivasan, "Simultaneous wavelength translation and amplitude modulation of single photons from a quantum dot," Phys. Rev. Lett., vol. 107, p. 083602, Aug 2011. [Online]. Available: http://link.aps.org/doi/10.1103/PhysRevLett.107.083602

[155] A. Kuhn, M. Hennrich, and G. Rempe, "Deterministic single-photon source for distributed quantum networking," Phys. Rev. Lett., vol. 89, p. 067901, Jul 2002. [Online]. Available: http://link.aps.org/doi/10.1103/PhysRevLett.89.067901

[156] J. McKeever, A. Boca, A. D. Boozer, R. Miller, J. R. Buck, A. Kuzmich, and H. J. Kimble, "Deterministic generation of single photons from one atom trapped in a cavity," Science, vol. 303, no. 5666, pp. 1992–1994, 2004. [Online]. Available: http://www.sciencemag.org/content/303/5666/1992.abstract

[157] Y. Yin, Y. Chen, D. Sank, P. J. J. O'Malley, T. C. White, R. Barends, J. Kelly, E. Lucero, M. Mariantoni, A. Megrant, C. Neill, A. Vainsencher, J. Wenner, A. N. Korotkov, A. N. Cleland, and J. M. Martinis, "Catch and release of microwave photon states," Phys. Rev. Lett., vol. 110, p. 107001, Mar 2013. [Online]. Available: http://link.aps.org/doi/10.1103/PhysRevLett.110.107001

[158] M. Pierre, I.-M. Svensson, S. Raman Sathyamoorthy, G. Johansson, and P. Delsing, "Storage and on-demand release of microwaves using superconducting resonators with tunable coupling," Applied Physics Letters, vol. 104, no. 23, pp. –, 2014. [Online]. Available: http://scitation.aip.org/content/aip/journal/apl/104/23/10.1063/1.4882646

[159] J. Wenner, Y. Yin, Y. Chen, R. Barends, B. Chiaro, E. Jeffrey, J. Kelly, A. Megrant, J. Y. Mutus, C. Neill, P. J. J. O'Malley, P. Roushan, D. Sank, A. Vainsencher, T. C. White, A. N. Korotkov, A. N. Cleland, and J. M. Martinis, "Catching time-reversed microwave coherent state photons with 99.4% absorption efficiency," Phys. Rev. Lett., vol. 112, p. 210501, May 2014. [Online]. Available: http://link.aps.org/doi/10.1103/PhysRevLett.112.210501

[160] M. Pechal, L. Huthmacher, C. Eichler, S. Zeytinoğlu, A. A. Abdumalikov, S. Berger, A. Wallraff, and S. Filipp, "Microwave-controlled generation of shaped single photons in circuit quantum electrodynamics," Phys. Rev. X, vol. 4, p. 041010, Oct 2014. [Online]. Available: http://link.aps.org/doi/10.1103/PhysRevX.4.041010

[161] S. J. Srinivasan, N. M. Sundaresan, D. Sadri, Y. Liu, J. M. Gambetta, T. Yu, S. M. Girvin, and A. A. Houck, "Time-reversal symmetrization of spontaneous emission for quantum state transfer," Phys. Rev. A, vol. 89, p. 033857, Mar 2014. [Online]. Available: http://link.aps.org/doi/10.1103/PhysRevA.89.033857

[162] E. Zakka-Bajjani, F. Nguyen, M. Lee, L. R. Vale, R. W. Simmonds, and J. Aumentado, "Quantum superposition of a single microwave photon in two different 'colour' states," Nature Physics, vol. 7, no. 8, pp. 599–603, 2011. [Online]. Available: http://dx.doi.org/doi:10.1038/nphys2035

[163] B. Abdo, K. Sliwa, F. Schackert, N. Bergeal, M. Hatridge, L. Frunzio, A. D. Stone, and M. Devoret, "Full coherent frequency conversion between two propagating microwave modes," Phys. Rev. Lett., vol. 110, p. 173902, Apr 2013. [Online]. Available: http://link.aps.org/doi/10.1103/PhysRevLett.110.173902

[164] K. Inomata, K. Koshino, Z. R. Lin, W. D. Oliver, J. S. Tsai, Y. Nakamura, and T. Yamamoto, "Microwave down-conversion with an impedance-matched Λ system in driven circuit QED," Phys. Rev. Lett., vol. 113, p. 063604, Aug 2014. [Online]. Available: http://link.aps.org/doi/10.1103/PhysRevLett.113.063604

[165] A. Houck, D. Schuster, J. Gambetta, J. Schreier, B. Johnson, J. Chow, L. Frunzio, J. Majer, M. Devoret, S. Girvin et al., "Generating single microwave photons in a circuit," Nature, vol. 449, no. 7160, pp. 328–331, 2007. [Online]. Available: http://dx.doi.org/doi:10.1038/nature06126

[166] H. Paik, D. I. Schuster, L. S. Bishop, G. Kirchmair, G. Catelani, A. P. Sears, B. R. Johnson, M. J. Reagor, L. Frunzio, L. I. Glazman, S. M. Girvin, M. H. Devoret, and R. J. Schoelkopf, "Observation of high coherence in Josephson junction qubits measured in a three-dimensional circuit QED architecture," Phys. Rev. Lett., vol. 107, p. 240501, Dec 2011. [Online]. Available: http://link.aps.org/doi/10.1103/PhysRevLett.107.240501

[167] J. Suh, A. J. Weinstein, C. U. Lei, E. E. Wollman, S. K. Steinke, P. Meystre, A. A. Clerk, and K. C. Schwab, "Mechanically detecting and avoiding the quantum fluctuations of a microwave field," Science, vol. 344, no. 6189, pp. 1262–1265, 2014. [Online]. Available: http://www.sciencemag.org/content/344/6189/1262.abstract

[168] R. Puers and D. Lapadatu, "Electrostatic forces and their effects on capacitive mechanical sensors," Sensors and Actuators A: Physical, vol. 56, no. 3, pp. 203–210, 1996. [Online]. Available: http://www.sciencedirect.com/science/article/pii/S0924424796013106

[169] N. Lobontiu and E. Garcia, Mechanics of microelectromechanical systems, 1st ed. New York: Kluwer Academic, 2005.

[170] J. Kolodzey, E. Chowdhury, T. Adam, G. Qui, I. Rau, J. Olowolafe, J. Suehle, and Y. Chen, "Electrical conduction and dielectric breakdown in aluminum oxide insulators on silicon," IEEE Transactions on Electron Devices, vol. 47, no. 1, pp. 121–128, Jan 2000. [Online]. Available: http://dx.doi.org/doi:10.1109/16.817577

[171] E. Hourdakis, B. J. Simonds, and N. M. Zimmerman, "Submicron gap capacitor for measurement of breakdown voltage in air," Review of Scientific Instruments, vol. 77, no. 3, pp. –, 2006. [Online]. Available: http://scitation.aip.org/content/aip/journal/rsi/77/3/10.1063/1.2185149

[172] D. J. Griffiths, Introduction to Electrodynamics, 3rd ed. New Jersey: Prentice Hall, 1999.

[173] S. Chowdhury, M. Ahmadi, and W. C. Miller, "A closed-form model for the pull-in voltage of electrostatically actuated cantilever beams," Journal of Micromechanics and Microengineering, vol. 15, no. 4, p. 756, 2005. [Online]. Available: http://stacks.iop.org/0960-1317/15/i=4/a=012

[174] F. Lecocq, J. D. Teufel, J. Aumentado, and R. W. Simmonds, "Resolving vacuum fluctuations of micromechanical motion using a phonon counter," ArXiv e-prints, Sep 2014. [Online]. Available: http://arxiv.org/abs/1409.0872

[175] H. B. G. Casimir, "On the attraction between two perfectly conducting plates," Proc. Kon. Ned. Akad. Wetenschap., vol. 51, pp. 793–795, 1948. [Online]. Available: http://www.dwc.knaw.nl/toegangen/digital-library-knaw/?pagetype=publDetail&pId=PU00018547

[176] F. Serry, D. Walliser, and G. Maclay, "The anharmonic Casimir oscillator (ACO)—the Casimir effect in a model microelectromechanical system," Journal of Microelectromechanical Systems, vol. 4, no. 4, pp. 193–205, Dec 1995. [Online]. Available: http://dx.doi.org/10.1109/84.475546

[177] S. K. Lamoreaux, "Demonstration of the casimir force in the 0.6 to 6μm range," Phys. Rev. Lett., vol. 78, pp. 5–8, Jan 1997. [Online]. Available: http://link.aps.org/doi/10.1103/PhysRevLett.78.5

[178] C. C. Speake and C. Trenkel, "Forces between conducting surfaces due to spatial variations of surface potential," Phys. Rev. Lett., vol. 90, p. 160403, Apr 2003. [Online]. Available: http://link.aps.org/doi/10.1103/PhysRevLett.90.160403

[179] W. J. Kim, A. O. Sushkov, D. A. R. Dalvit, and S. K. Lamoreaux, "Surface contact potential patches and Casimir force measurements," Phys. Rev. A, vol. 81, p. 022505, Feb 2010. [Online]. Available: http://link.aps.org/doi/10.1103/PhysRevA.81.022505

[180] F. Intravaia and A. Lambrecht, "Surface plasmon modes and the Casimir energy," Phys. Rev. Lett., vol. 94, p. 110404, Mar 2005. [Online]. Available: http://link.aps.org/doi/10.1103/PhysRevLett.94.110404

[181] J. N. Munday, F. Capasso, and V. A. Parsegian, "Measured long-range repulsive Casimir–Lifshitz forces," Nature, vol. 457, no. 7226, pp. 170–173, 2009. [Online]. Available: http://dx/doi/org/doi:10.1038/nature07610

[182] J. H. Wilson, A. A. Allocca, and V. M. Galitski, "Repulsive Casimir force between Weyl semimetals," ArXiv e-prints, Jan 2015. [Online]. Available: http://arxiv.org/abs/1501.07659

[183] K. Jahne, B. Yurke, and U. Gavish, "High-fidelity transfer of an arbitrary quantum state between harmonic oscillators," Phys. Rev. A, vol. 75, p. 010301, Jan 2007. [Online]. Available: http://dx.doi.org/doi:10.1103/PhysRevA.75.010301

[184] A. N. Korotkov, "Flying microwave qubits with nearly perfect transfer efficiency," Phys. Rev. B, vol. 84, p. 014510, Jul 2011. [Online]. Available: http://link.aps.org/doi/10.1103/PhysRevB.84.014510

[185] J. W. Harlow, "Microwave electromechanics: Measuring and manipulating the quantum state of a macroscopic mechanical oscillator," Ph.D. dissertation, Univ. of Colo. at Boulder, 2013.

[186] J. L. Horner, Ed., Optical Signal Processing. San Diego: Academic Press, 1987.

[187] M. Castellanos-Beltran, K. Irwin, G. Hilton, L. Vale, and K. Lehnert, "Amplification and squeezing of quantum noise with a tunable Josephson metamaterial," Nature Physics, vol. 4, no. 12, pp. 929–931, 2008. [Online]. Available: http://dx.doi.org/doi:10.1038/nphys1090

[188] B. Yurke, L. R. Corruccini, P. G. Kaminsky, L. W. Rupp, A. D. Smith, A. H. Silver, R. W. Simon, and E. A. Whittaker, "Observation of parametric amplification and deamplification in a Josephson parametric amplifier," Phys. Rev. A, vol. 39, pp. 2519–2533, Mar 1989. [Online]. Available: http://link.aps.org/doi/10.1103/PhysRevA.39.2519

[189] M. Castellanos-Beltran, "Development of a Josephson parametric amplifier for the preparation and detection of nonclassical states of microwave fields," Ph.D. dissertation, Univ. of Colo. at Boulder, 2010.

[190] T. A. Palomaki, J. D. Teufel, R. W. Simmonds, and K. W. Lehnert, "Entangling mechanical motion with microwave fields," Science, vol. 342, no. 6159, pp. 710–713, 2013. [Online]. Available: http://www.sciencemag.org/content/342/6159/710.abstract

[191] B. Boashash, "Note on the use of the Wigner distribution for time-frequency signal analysis," IEEE Transactions on Acoustics, Speech and Signal Processing, vol. 36, no. 9, pp. 1518–1521, Sep 1988. [Online]. Available: http://dx.doi.org/doi:10.1109/29.90380

[192] L. Cohen, Time-Frequency Analysis. New Jersey: Prentice Hall, 1995.

[193] W. Mecklenbrauker and F. Hlawatsch, Eds., The Wigner Distribution: Theory and Applications in Signal Processing. Amsterdam: Elsevier, 1997.

[194] B. P. Gibbs, Advanced Kalman Filtering, Least-Squares and Modeling: A Practical Handbook. New York: John Wiley and Sons, 2011.

[195] U. Leonhardt, Measuring the Quantum State of Light. Cambridge: Cambridge University Press, 1997.

[196] B. Vlastakis, G. Kirchmair, Z. Leghtas, S. E. Nigg, L. Frunzio, S. M. Girvin, M. Mirrahimi, M. H. Devoret, and R. J. Schoelkopf, "Deterministically encoding quantum information using 100-photon Schrodinger cat states," Science, vol. 342, no. 6158, pp. 607–610, 2013. [Online]. Available: http://www.sciencemag.org/content/342/6158/607.abstract

[197] M. R. Vanner, I. Pikovski, and M. S. Kim, "Towards optomechanical quantum state reconstruction of mechanical motion," Annalen der Physik, vol. 527, no. 1-2, pp. 15–26, 2015. [Online]. Available: http://dx.doi.org/10.1002/andp.201400124

[198] M. R. Vanner, J. Hofer, G. D. Cole, and M. Aspelmeyer, "Cooling-by-measurement and mechanical state tomography via pulsed optomechanics," Nature Communications, vol. 4, 2013. [Online]. Available: http://dx.doi.org/doi:10.1038/ncomms3295

[199] J. B. Hertzberg, T. Rocheleau, T. Ndukum, M. Savva, A. A. Clerk, and K. C. Schwab, "Back-action-evading measurements of nanomechanical motion," Nature Physics, vol. 6, no. 3, pp. 213–217, 2010. [Online]. Available: http://dx.doi.org/doi:10.1038/nphys1479

[200] D. Rugar and P. Grütter, "Mechanical parametric amplification and thermomechanical noise squeezing," Phys. Rev. Lett., vol. 67, pp. 699–702, Aug 1991. [Online]. Available: http://link.aps.org/doi/10.1103/PhysRevLett.67.699

[201] A. Szorkovszky, G. A. Brawley, A. C. Doherty, and W. P. Bowen, "Strong thermomechanical squeezing via weak measurement," Phys. Rev. Lett., vol. 110, p. 184301, May 2013. [Online]. Available: http://link.aps.org/doi/10.1103/PhysRevLett.110.184301

[202] J. Suh, A. J. Weinstein, and K. C. Schwab, "Optomechanical effects of two-level systems in a back-action evading measurement of micro-mechanical motion," Applied Physics Letters, vol. 103, no. 5, pp. –, 2013. [Online]. Available: http://scitation.aip.org/content/aip/journal/apl/103/5/10.1063/1.4816428

[203] I.-C. Hoi, C. M. Wilson, G. Johansson, T. Palomaki, B. Peropadre, and P. Delsing, "Demonstration of a single-photon router in the microwave regime," Phys. Rev. Lett., vol. 107, p. 073601, Aug 2011. [Online]. Available: http://link.aps.org/doi/10.1103/PhysRevLett.107.073601

[204] I. Shomroni, S. Rosenblum, Y. Lovsky, O. Bechler, G. Guendelman, and B. Dayan, "All-optical routing of single photons by a one-atom switch controlled by a single photon," Science, vol. 345, no. 6199, pp. 903–906, 2014. [Online]. Available: http://www.sciencemag.org/content/345/6199/903.abstract

[205] J. E. Mahan, Physical Vapor Deposition of Thin Films. New York: John Wiley and Sons, 2000.

[206] J. William S. Rees, Ed., CVD of Nonmetals. Weinheim: VCH, 1998.

[207] G. T. A. Kovacs, Micromachined Transducers Sourcebook. New York: McGraw Hill, 1998.

Appendix A

Construction details of circuits and membranes

Figs. A.1 and A.2 overview the microfabrication steps used to create the microwave circuit used in the microwave-to-optical frequency converter and the temporal and spectral mode converter, respectively. The figures show profile views starting from the initial wafer, which is made from either silicon or sapphire. Layers of material are added and removed using standard deposition [205, 206] and etching [207] processes. Tables A.1 amd A.2 give the deposition processes and etch/removal processes for different materials used during construction of the frequency converter and temporal and spectral mode converter, respectively. All fabrication was performed at the NIST Boulder Microfabrication Facility (BMF). Additional information about construction of the microwave circuit is provided in section 3.3.1 (for microwave-to-optical frequency conversion) and section 4.2.2 (for temporal and spectral mode conversion).

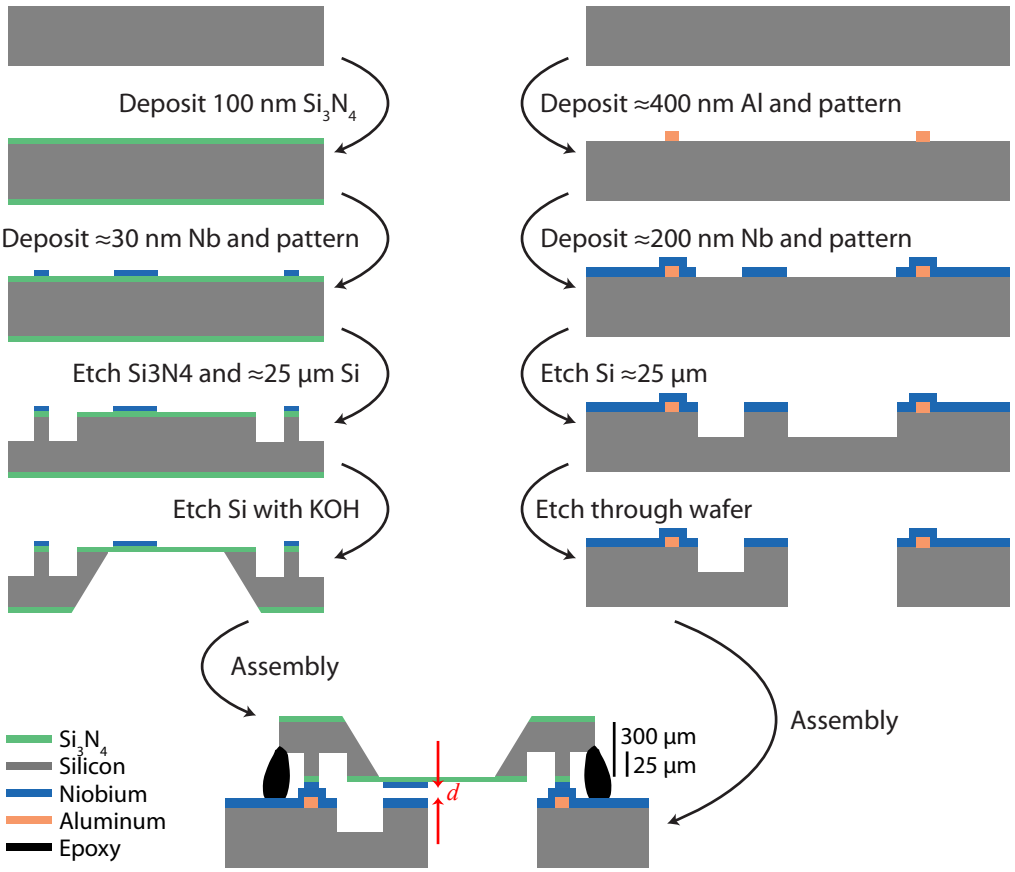

Figure A.1: Construction details of microwave circuit for frequency conversion. Both structures begin with high-resistivity silicon wafers. With an aluminum layer of $\approx$ 400 nm, the separation distance $d \approx 400$ nm.

Table A.1: Deposition and etch processes used during construction of the microwave circuit used for frequency conversion.

Material	Deposition process	Removal process
Silicon nitride (Si_3N_4)	LPCVD	RIE with CF_4
Niobium	DC magnetron sputtering	RIE with 30% O_2 and 60% CF_4 or ICP+RIE with SF_6
Aluminum	Electron beam deposition	Wet etch with Transene type A
Silicon		DRIE with SF_6 and C_4F_8 or Wet etch with KOH

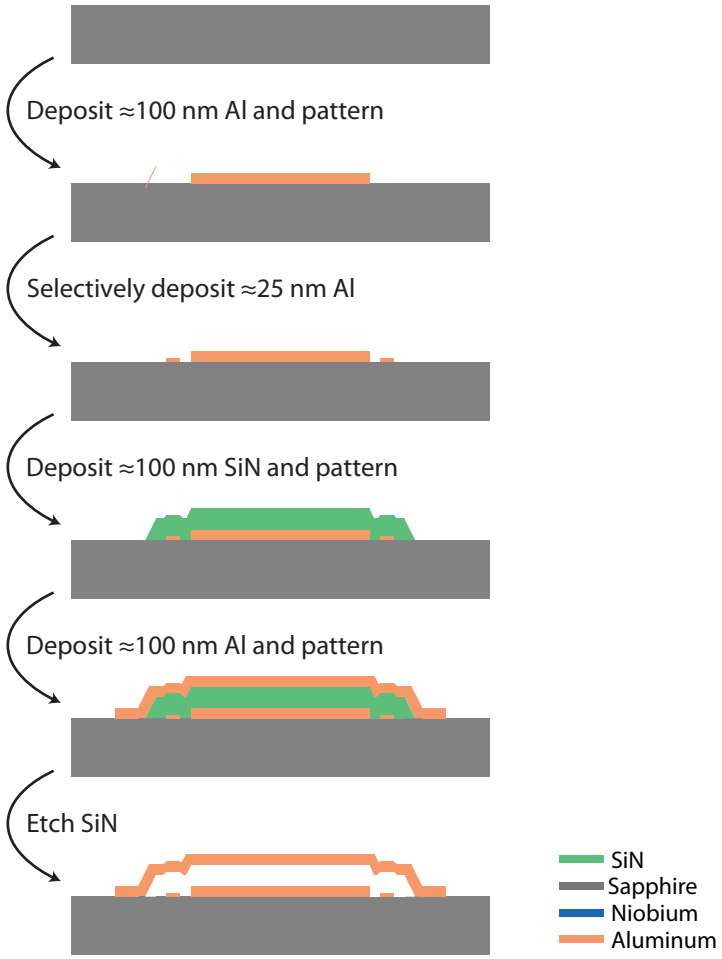

Figure A.2: Construction details of temporal and spectral mode converter. Construction begins with a sapphire wafer. The two initial layers of aluminum form the microwave electrode and the actuation electrode, visible in Fig. 4.3. The final layer of aluminum forms the membrane once the silicon nitride is removed.

Table A.2: Deposition and etch processes used during construction of the temporal and spectral mode converter.

Material	Deposition process	Removal Process
Aluminum, 100 nm layers	DC magnetron sputtering	RIE with 25% Cl_2 and 75% BCl_3
Aluminum, 25 nm layer	electron beam deposition	
Silicon nitride (SiN_x)	PECVD	RIE with 60% O_2 and 40% CF_4 or RIE with SF_6

Appendix B

Predicted frequency tuning of the temporal and spectral mode converter

The approximate geometry of the temporal and spectral mode converter is outlined in Fig. 4.4a. With this geometry, we use a finite element simulation to predict the effect of thermal contraction between the aluminum and the sapphire substrate. In simulation, the total thermal contraction is adjusted so that the central portion of the drumhead deflects by ≈160 nm, leaving a ≈40 nm separation between the plates of the microwave capacitor, a value set by the measured $Gx_{\mathrm{zp}} = 2\pi \times 270$ Hz. The total thermal contraction needed to create this amount of deflection is seven parts per thousand, a value approximately consistent with that of bulk aluminum. The predicted effect of thermal contraction on device geometry is shown in Fig. 4.4b.

Using relevant parameters from the thermally-altered geometry of Fig. 4.4, we create a simplified model to predict the frequency tuning of the mode converter. This model, detailed in Fig. B.1, is used in a finite element simulation to estimate the membrane's vibrational frequency and deflection. As the membrane deflects with increasing voltage, it alters the capacitance in the microwave circuit and thus its resonant frequency. This effect is modeled by assuming a parallel plate capacitance (C_{m}) that is modulated by changes in the position of the aluminum membrane, and an additional parasitic capacitance (C_{p}) provided by, for example, the coils of the inductor. With no applied voltage, $C_{\mathrm{m}}/\left(C_{\mathrm{p}} + C_{\mathrm{m}}\right) = 0.65$, estimated from electromagnetic simulations of the microwave circuit. Using this information, we predict the frequency tuning shown as dashed lines in Fig. 4.5.

In order to correctly predict the frequency tuning of the device, we must include the effects of

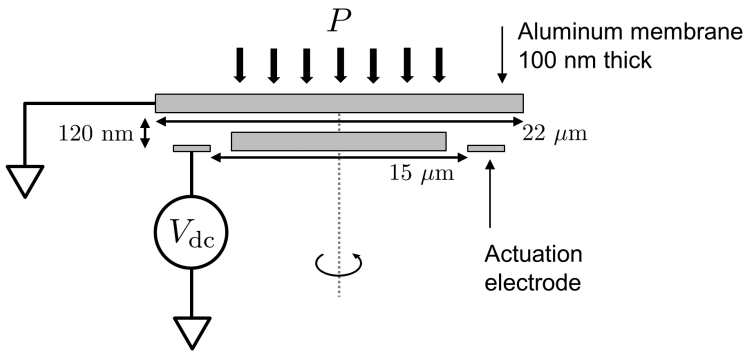

Figure B.1: Simplified model of the aluminum membrane and actuation electrode used in the mode converter. The membrane is under tension with fixed edges so that with $V_{\rm dc} = 0$, $\omega_{\rm m} = 2\pi \times 9.56$ MHz. The membrane is periodically perforated so that it resembles Fig. 4.3. A voltage $V_{\rm dc}$ can be applied between the membrane and the actuation electrode. Additional attractive forces are incorporated by distributing the force over the central area of the membrane that overlaps with the capacitor plate (the capacitor plate is shown for clarity, but is not used during simulation). For example, to model a Casimir force, $P \to -0.7 \times \hbar c\pi^2/240(d-x)^4$, where $d = 40$ nm is the initial separation distance with $V_{\rm dc} = 0$ and x is the local deflection of the membrane away from its equilibrium position.

the Casimir force. We include an attractive pressure of approximately $0.7 \times P_{\rm cas}$ in a finite element simulation of the membrane in the presence of a DC voltage, where $P_{\rm cas} = -\hbar c\pi^2/240a^4$ is the Casimir pressure for two parallel, perfectly conducting plates separated by a distance a of vacuum. (For imperfectly conducting plates, a reduction in the Casimir force for small separations $d \lesssim \lambda_{\rm p}$ is expected, where $\lambda_{\rm p}$ is the plasma wavelength of the conducting plates [180].) With this additional pressure, we predict the frequency tuning shown as solid lines in Fig. 4.5.

Appendix C

Measurement network for microwave-to-optical frequency converter

Fig. C.1 shows a detailed diagram of the network used to measure the microwave-to-optical frequency converter presented in Chapter 3. The network contains components that function at microwave frequencies (≈7 GHz), optical frequencies (≈282 THz), and mechanical frequencies (≈1 MHz). The necessary optical components are discussed in section C.1, and the necessary microwave components in section C.2. Mechanical frequency signals are written onto microwave or optical signals and then injected into the converter before being measured, as discussed in section C.3.

C.1 Optical network

The optical network utilizes two laser beams: A pump (Fig. C.1, red line) and a locking signal (Fig. C.1, green line), both of which are derived from a single 1064 nm Nd:YAG laser (Coherent, Inc. Mephisto). The laser beam is double-passed through a 200 MHz AOM that locks the laser frequency to the cavity, and then split into the pump and locking signal using two AOMs. The AOMs are modulated at approximatey 80 MHz with a relative detuning of 1 MHz, so the pump has a frequency 1 MHz below the locking signal. Polarizing beamsplitters (PBSs), and a half-wave plate are used to inject the pump and locking signal into orthogonal polarization modes of the optical cavity. Light reflected or emitted from the cavity is separated from incoming light using a Faraday rotator and detected with photodetectors. Transmitted light is also detected and used to measure optomechanical parameters. The measured locking signal provides feedback to the 200 MHz AOM and locks the frequency of the locking signal to the cavity's resonance using the Pound-

Drever-Hall technique. The cavity has a birefringent splitting of 270 kHz, and so the optical pump has a detuning of $\Delta_o = -2\pi \times 730$ kHz. The locking signal is low power and near the optical cavity's resonant frequency so the dynamical backaction from this signal can be neglected.

C.2 Microwave network

The microwave network utilizes an Agilent PSG signal generator to create a microwave pump at ≈ 7 GHz. This pump drives the microwave port of the converter, and additionally provides a local oscillator for two quadrature-IF mixers (Marki IQ-4509LXP) that are used to both upconvert and downconvert the signals that interact with the converter. Microwave signals reflected or emitted from the cavity are amplified using a room-temperature low noise amplifier (Miteq, Inc.). The microwave cavity is intrinsically stable (environmental fluctuations change the microwave resonant frequency by much less than its linewidth), and no stabilization technique is needed.

C.3 Signal generation and detection

A network analyzer generates a swept signal near the mechanical oscillator's resonant frequency. This signal is upconverted to either microwave or optical frequencies via single-sideband (SSB) modulation of the optical or microwave pump, a process where a signal (at frequency ω_1) modulates a pump (at frequency ω_2) to create an 'upper sideband' on the pump (at frequency $\omega_1 + \omega_2$). The signal directly modulates the microwave pump using a microwave-frequency mixer. However, to modulate the optical pump, the signal first modulates an $\approx$80 MHz pump that drives an AOM. Any stray lower sideband modulation (at frequency $\omega_2 - \omega_1$) is suppressed at least 20 dB (10 dB) below the upper sideband for SSB modulation at microwave (optical) frequencies. After interacting with the converter, reflected and transmitted signals are demodulated and detected using homodyne (direct) detection for microwave (optical) signals. The spectral density of outgoing optical signals can also be measured with a spectrum analyzer. Three switches allow the measurement network to change between measuring microwave or optical frequency signals.

For a measurement of $S_{21}(\omega) = a_{\text{out}}(\omega)/b_{\text{in}}(\omega)$, we generate an upper sideband on the mi-

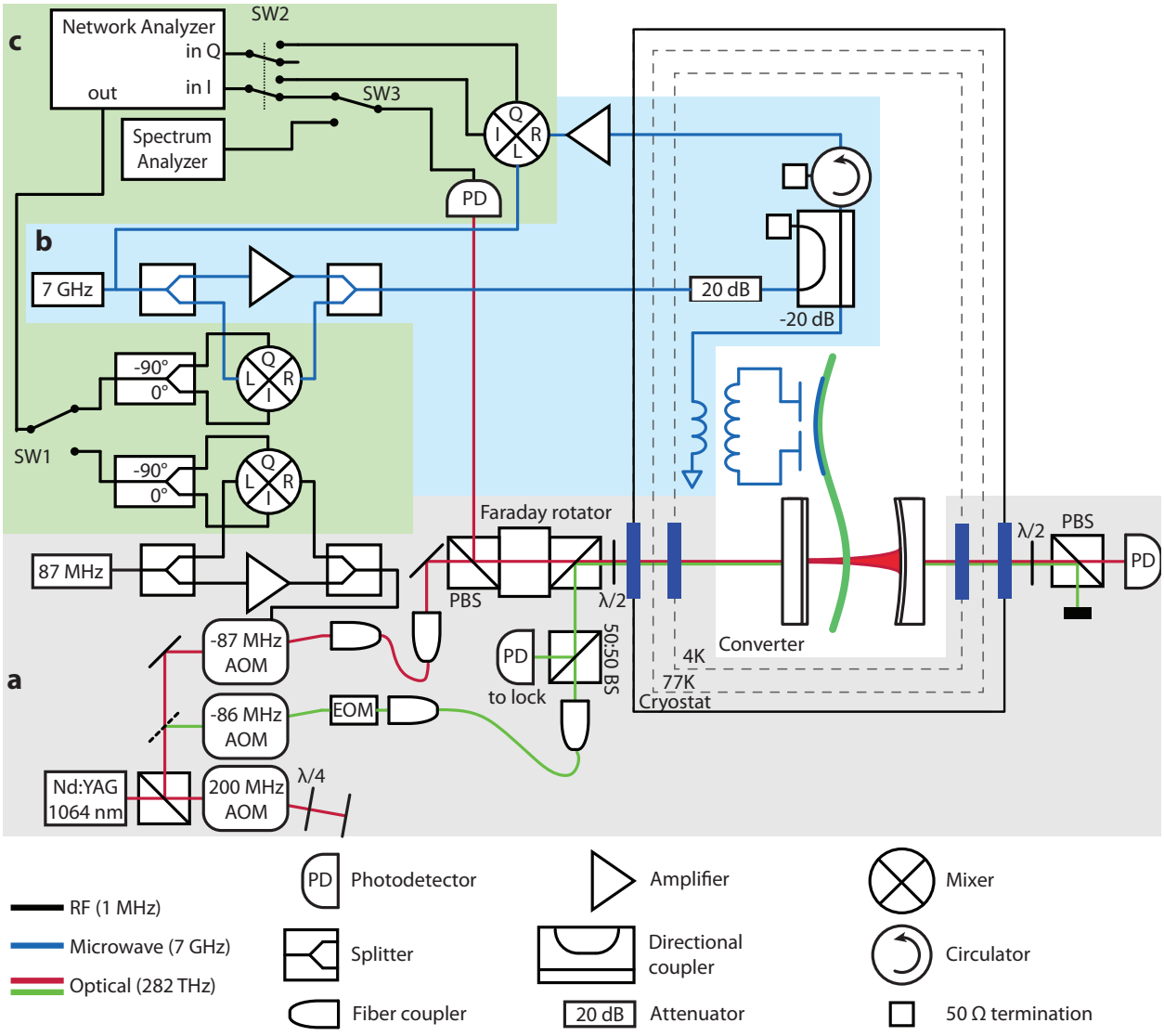

Figure C.1: Measurement network for the microwave-to-optical frequency converter. The network is divided into three general sections: **a**, Optical network. **b**, Microwave network. **c**, Signal generation and detection.

crowave pump (with amplitude and phase given by $b_{\text{in}}(\omega)$) and measure the upper sideband on the outgoing optical pump (which yields the amplitude and phase of $a_{\text{out}}(\omega)$). In general, the conversion process also produces a non-zero lower sideband; that is, the transfer function element that connects $b_{\text{in}}(\omega)$ to $a_{\text{out}}(-\omega)$ is nonzero (see Fig. 3.12). During downconversion (S_{12}) and microwave reflection (S_{11}), we collect both in-phase and quadrature data using homodyne detec-

tion. No information is lost during measurement, and we can reconstruct the amount of power present in the upper- and lower- sidebands ($b_{\rm out}(\omega)$ and $b_{\rm out}(-\omega)$, respectively) of the reflected microwave pump. During upconversion (S_{21}), the reflected optical pump and sidebands are focused onto a photodetector, and we only detect amplitude modulation of the pump. In order to assign a measured amplitude modulation an equivalent upper-sideband amplitude, we need to know the relationship between the upper- and lower- sidebands.

The photocurrent we measure is proportional to the incident photon flux (in units of number/sec). The photon flux is

$$f(t) \equiv \left\langle d^{\dagger}_{\rm out}(t) d_{\rm out}(t) \right\rangle \tag{C.1}$$

where $d_{\rm out}(t)$ is the annihilation operator for the light field incident on the detector and has units of $\sqrt{\text{number/sec}}$, as introduced in Chapter 2. During an upconversion measurement, an optical pump $a_{\rm in}(t) = \bar{a}_{\rm in} e^{-\imath\omega_{\rm in} t}$ is injected into the optical cavity. If the mechanical oscillator is vibrating with displacement $x_0 \sin(\omega'_{\rm m} t + \Phi)$, the outgoing field can be described by

$$\begin{aligned} d_{\rm out}(t) =& \frac{\imath\Delta_{\rm o} + \kappa_{\rm o,ext} - \kappa_{\rm o}/2}{-i\Delta_{\rm o} + \kappa_{\rm o}/2} \sqrt{\epsilon}\bar{a}_{\rm in} e^{-i\omega_{\rm in} t} \\ &+ \frac{G_{\rm o} x_0}{2} \frac{\kappa_{\rm o,ext}}{-\imath\Delta_{\rm o} + \kappa_{\rm o}/2} \sqrt{\epsilon}\bar{a}_{\rm in} \left(\frac{e^{-\imath(\omega_{\rm in} + \omega'_{\rm m})t - \imath\Phi}}{-\imath(\Delta_{\rm o} + \omega'_{\rm m}) + \kappa_{\rm o}/2} - \frac{e^{-\imath(\omega_{\rm in} - \omega'_{\rm m})t + \imath\Phi)}}{-\imath(\Delta_{\rm o} - \omega'_{\rm m}) + \kappa_{\rm o}/2} \right), \end{aligned} \tag{C.2}$$

in close analogy to Eqn. 2.15 where I've additionally included the effect of modematching as given by $\sqrt{\epsilon}$. The non-modematched light in the optical pump does not beat with the sidebands on the photodetector, and appears as a zero-frequency photocurrent. Defining $\theta = \text{Arg}[(\imath\Delta_{\rm o} + \kappa_{\rm o,ext} - \kappa_{\rm o}/2)/(-\imath\Delta_{\rm o} + \kappa_{\rm o}/2)]$, $\psi = \text{Arg}[\kappa_{\rm o,ext}/(-\imath\Delta_{\rm o} + \kappa_{\rm o}/2)]$, and neglecting the zero-frequency portion of the photocurrent,

$$f(t) = \mathcal{B} e^{-i(\omega'_{\rm m} t + \Phi)} \left(1 - e^{2i(\theta - \psi)} \left(\frac{-i(\Delta_{\rm o} + \omega'_{\rm m}) + \kappa_{\rm o}/2}{i(\Delta_{\rm o} - \omega'_{\rm m}) + \kappa_{\rm o}/2} \right) \right) + \text{c.c.} \tag{C.3}$$

$$\mathcal{B} = \epsilon \left| \bar{a}_{\rm in} \right|^2 \left| \frac{\imath\Delta_{\rm o} + \kappa_{\rm o,ext} - \kappa_{\rm o}/2}{-i\Delta_{\rm o} + \kappa_{\rm o}/2} \right| \left| \frac{\kappa_{\rm o,ext}}{-i\Delta_{\rm o} + \kappa_{\rm o}/2} \right| \frac{G_{\rm o} x_0}{2} \left(\frac{e^{-i(\theta - \psi)}}{-i(\Delta_{\rm o} + \omega'_{\rm m}) + \kappa_{\rm o}/2} \right)$$

In a measurement where we do not detect the lower sideband at frequency $\omega_{\rm p} - \omega'_{\rm m}$, we would detect a photocurrent proportional to $f_{ssb}(t)$. The ratio of these two photon fluxes is (using complex

notation to express a phase difference)

$$\frac{f_{\mathrm{ssb}}(t)}{f(t)} = \frac{1}{1 - e^{2i(\theta-\psi)}\left(\frac{-i(\Delta_{\mathrm{o}}+\omega'_{\mathrm{m}})+\kappa_{\mathrm{o}}/2}{i(\Delta_{\mathrm{o}}-\omega'_{\mathrm{m}})+\kappa_{\mathrm{o}}/2}\right)}. \tag{C.4}$$

This ratio allows us to convert between the measured photon flux $f(t)$ and an equivalent upper-sideband photon flux $f_{\mathrm{ssb}}(t)$.

Appendix D

Measurement network for temporal and spectral mode conversion

Fig. D.1 shows a detailed diagram of the network used to measure the temporal and spectral mode converter presented in Chapter 4. The network consists of four main components: Signals reflected or emitted from the mode converter are measured with a sensitive microwave receiver (subsection D.1). Microwave signals that interact with the mode converter are created using a combination of arbitrary waveform generation and upconversion (subsection D.2). The mode converter and a resistive load are mounted to the base stage of a dilution refrigerator (subsection D.3). A voltage bias on the actuation electrode controls the center frequency of the mode converter (subsection D.4).

D.1 Microwave receiver

Microwave signals reflected or emitted from the mode converter are measured via a sensitive microwave receiver. The first component of the receiver is a Josephson parametric amplifier (JPA), followed by additional amplifiers, a downconverting mixer, and a digitizer. A microwave pump detuned 1 MHz below the converter's resonant frequency of $\omega_{e,2} = 2\pi \times 7.34$ GHz drives the JPA. This pump also serves as the phase reference for the downconverting mixer. We adjust the phase of the pump entering the local oscillator (LO) port of the downconverting mixer so that the signal amplified by the JPA exits via the in-phase channel of the mixer. This channel is sampled by a high speed digitizer (AlazarTech ATS 9462).

The JPA has a limited dynamic range [189], and the pumps used with the mode converter

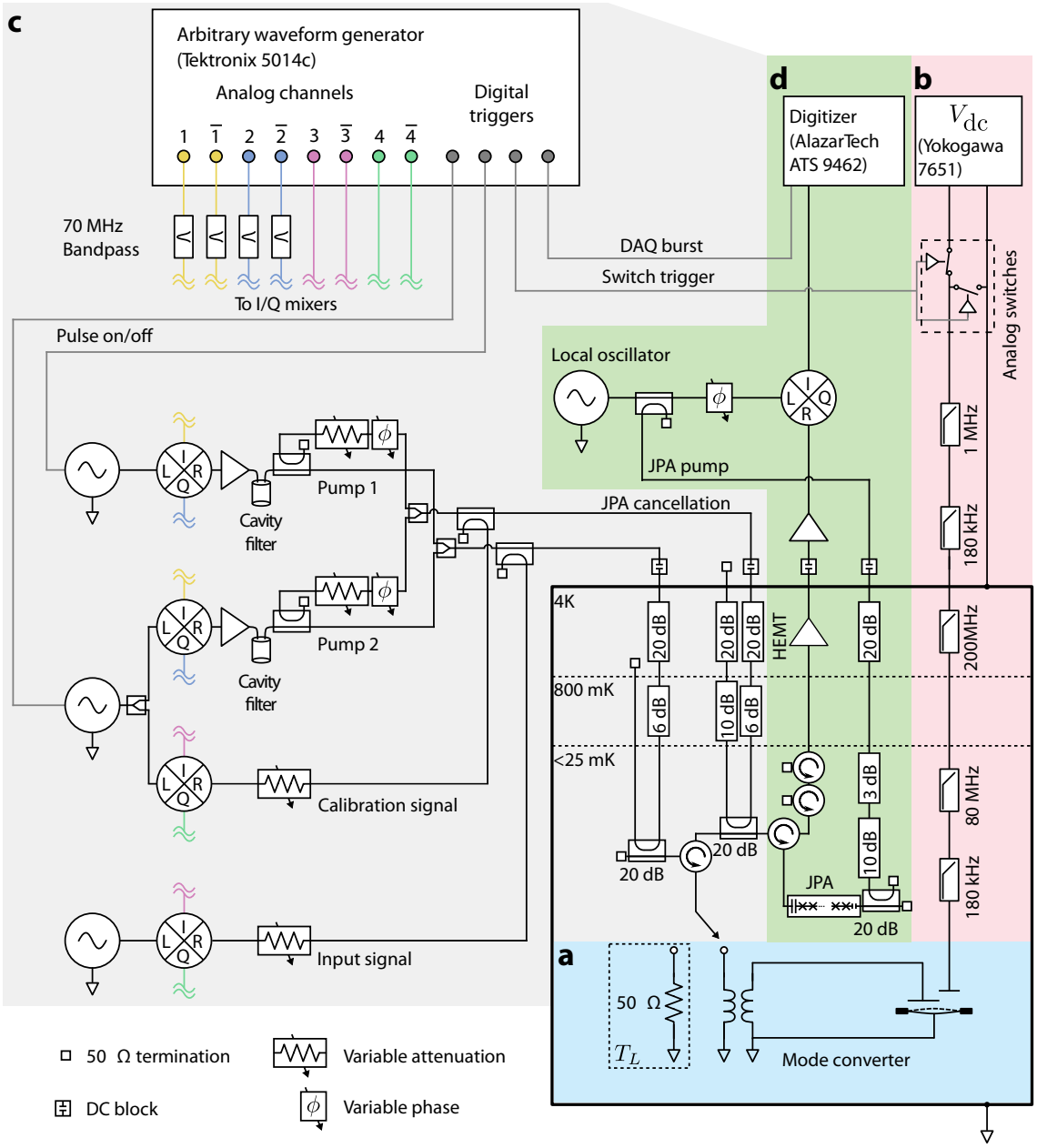

Figure D.1: Measurement network for temporal and spectral mode conversion. **a**, Microwave receiver. **b**, Microwave generation. **c**, Mode converter at <25 mK and resistive load at temperature T_{L}. **d**, Actuation line.

carry enough power to saturate the JPA's gain. We use variable attenuators and phase shifters to create cancellation tones that reduce the pump power incident on the JPA by 50 to 60 dB, which is sufficient for proper JPA operation. We monitor the gain of the JPA (for both gain drift and saturation) with a weak calibration signal.

D.2 Microwave generation

Waveforms with programmable amplitude, phase, and frequency are generated by a Tektronix 5014c arbitrary waveform generator (AWG). However, the AWG can only produce waveforms with center frequencies up to approximately 300 MHz. We must upconvert these waveforms so they interact with the mode converter, which has a center frequency of approximately 7 GHz (see Fig. 4.5). Upconversion is accomplished via single-sideband modulation, a process where the original waveform (centered at frequency ω_1) modulates a constant microwave tone (at frequency ω_2) to produce a final waveform (centered at frequency $\omega_1 + \omega_2$). Agilent PSG signal generators provide the constant microwave tones, and microwave mixers (Marki Microwave IQ4509-MXP) combine the microwave tones and the waveforms from the AWG. The relative phase, amplitude, and DC offsets of the AWG waveforms are adjusted to compensate for non-idealities in the mixer.

Channels 1 and 2 of the AWG produce four waveforms centered at 70 MHz that create the microwave pumps used during our mode conversion protocol (see section 4.6). Bandpass filters (KR Electronics 2657) at the outputs of the AWG attenuate phase and amplitude noise by >40 dB for frequencies outside their passband (≈20 MHz centered at 70 MHz). Although the filters limit the bandwidth of waveforms produced by the AWG, this bandwidth is sufficient for our mode conversion protocol. Once the waveforms are upconverted using single-sideband modulation, they are amplified (Mini-Circuits ZVA-183V) and additionally filtered [77]. Ideally, this procedure results in a microwave-frequency pump at frequency $\omega_{e,1} - \omega_m$ or frequency $\omega_{e,2} - \omega_m$ that is >170 dB more powerful than at frequency $\omega_{e,1}$ or $\omega_{e,2}$. This large dynamic range is necessary to produce a powerful microwave pump whose phase and amplitude noise do not incoherently drive vibrations of the mechanical oscillator. When no pump is necessary, the Agilent PSGs are pulsed off so that

they emit no microwave tone.

Channels 3 and 4 of the AWG produce waveforms centered at 30 MHz that create the signals used during our mode conversion protocol. Once upconverted, the waveforms produced by the AWG are at frequency $\omega_{e,1}$ or $\omega_{e,2}$. These signals are neither amplified nor filtered because the signals can be attenuated to reduce phase and amplitude noise. The signal at frequency $\omega_{e,1}$ is manipulated with the mode converter. The signal at frequency $\omega_{e,2}$ is used to monitor the gain of the JPA and additionally used to correct small (< 10 ps) timing errors that occur between the AWG and the Agilent PSGs during each repetition of our mode conversion protocol.

D.3 Mode converter and resistive load

The mode converter and a resistive load are mounted to the base stage of a dilution refrigerator and cooled to <25 millikelvin. A low insertion loss (<0.30 dB) 2-way switch (Radiall R577433000) connects the microwave receiver to either the mode converter or the resistive load. The temperature of the resistive load, T_L, can be varied without significantly affecting the temperature of the mode converter or fridge, as it has a weak thermal link to base stage of the dilution refrigerator and has an attached heating element. The resistive load injects a known amount of noise into the microwave receiver, and this noise allows us to calibrate the efficiency and gain of the microwave receiver (see section 4.4.1).

D.4 Actuation line

The voltage on the actuation line controls the microwave circuit's resonant frequency. We use a stable voltage source (Yokogawa 7651) to provide a constant V_{dc}. Solid state switches (Maxim Integrated 313) change the voltage on the actuation line between V_{dc} and 0 V. The state of the switch network is controlled by a digital output of the AWG.

The actuation line is filtered to ensure voltage fluctuations in V_{dc} do not incoherently drive the mechanical oscillator. In particular, the mechanical oscillator is sensitive to voltage fluctuations near its resonant frequency of $\omega_m \approx 2\pi \times 9$ MHz. Room temperature filters attenuate fluctuation in

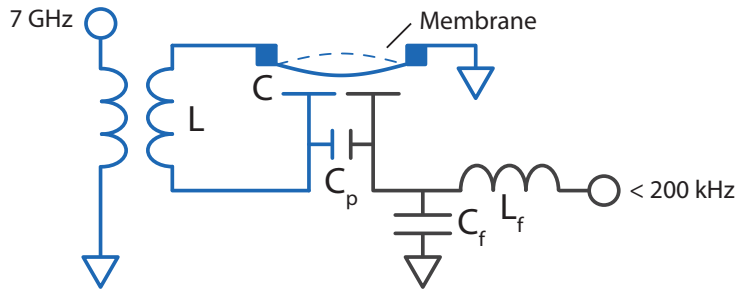

Figure D.2: Circuit diagram of mode converter, including a low-pass filter on the actuation line. Parasitic capacitance, C_p, between the actuation electrode and the microwave electrode causes microwave energy in the inductor-capacitor electromagnetic resonator (shown in blue) to exit via the actuation line (shown in black). For the design shown in Figs. 4.3 and 4.4, $C_p \approx 3$ fF. The low-pass filter has $L_f \approx 20$ nH and $C_f \approx 1$ pF. When the filter is terminated with 50 Ohm load, as done in our experiments with a bias tee, the energy loss rate is relatively small (estimated to be ≈10 kHz)

V_{dc} by more than 100 dB at frequencies near ω_m, and cryogenic low-pass filters provide additional attenuation near ω_m. These filters are designed so the voltage noise seen by the mode converter (at frequencies near ω_m) is ideally given by Johnson noise from a few Ohms at <25 mK. Additionally, the filters provide enough bandwidth to quickly (<30 μs) change the voltage on the actuation line.

The external filters sufficiently suppress voltage noise; however, the actuation line must also not dissipate microwave energy stored in the electromagnetic resonator. To limit the loss of microwave energy, we include a superconducting inductor-capacitor low-pass filter on the actuation line during construction of the mode converter. A circuit diagram of the mode converter and filter is shown in Fig. D.2. With this filter, we estimate a microwave energy loss rate through the DC line of ∼10 kHz, much less than the total energy loss rate of $\kappa = 2\pi \times 2.5$ MHz (see table 4.1).